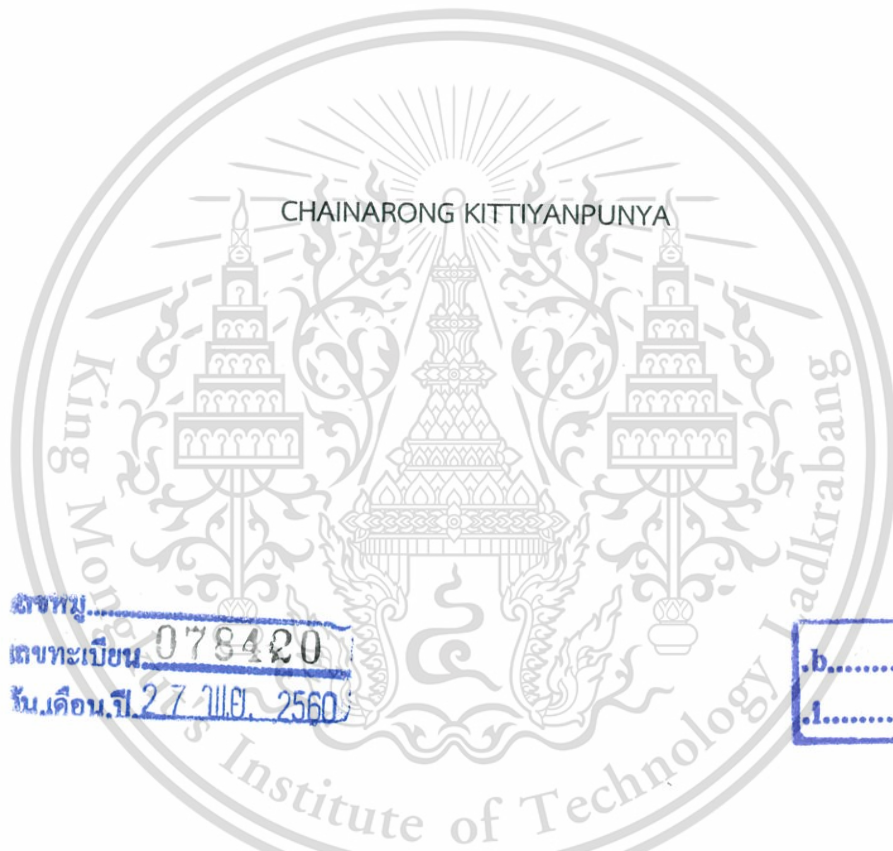




E078420



A THESIS SUBMITTED IN PARTIAL FULFILLMENT
OF THE REQUIREMENT FOR THE DEGREE OF
DOCTOR OF ENGINEERING IN ELECTRICAL ENGINEERING
FACULTY OF ENGINEERING
KING MONGKUT'S INSTITUTE OF TECHNOLOGY LADKRABANG

2017

KMITL-2017-EN-D-018-058



COPYRIGHT 2017

FACULTY OF ENGINEERING

KING MONGKUT'S INSTITUTE OF TECHNOLOGY LADKRABANG

This material is reserved for educational use only, not allowed for commercial use.

Forbidden to modify the content, and cite the document when use.

หัวข้อวิทยานิพนธ์	สายอากาศยาคี-อูตะที่สามารถเปลี่ยนทิศทางการแผ่พลังงานและการประยุกต์ใช้งาน
นักศึกษา	นาย ไชยณรงค์ กิตติญาณปัญญา
รหัสนักศึกษา	56601008
ปริญญา	วิศวกรรมศาสตรดุษฎีบัณฑิต
สาขาวิชา	วิศวกรรมไฟฟ้า
พ.ศ.	2560
อาจารย์ที่ปรึกษาวิทยานิพนธ์	ศาสตราจารย์ ดร.โมไนย ไกรฤกษ์

บทคัดย่อ

ปัญหาของผลผลิตทางการเกษตรที่ไม่ได้มาตรฐานทำให้เกิดการขาดทุนของพ่อค้า เพราะฉะนั้นเซ็นเซอร์แบบไม่ทำลายที่สามารถระบุคุณภาพของผลผลิตเป็นที่ต้องการอย่างมาก นี่เป็นเหตุผลที่วิทยานิพนธ์นี้นำเสนอการประยุกต์ใช้งานของสายอากาศยาคี-อูตะที่สามารถเปลี่ยนทิศทางการแผ่พลังงานเพื่อปรับปรุงระบบเซ็นเซอร์ โดยวิทยานิพนธ์นี้ออกแบบระบบเซ็นเซอร์บนพื้นฐานของรีเฟล็กต์โอมิเตอร์แบบกวาดลำคลื่นซึ่งทำงานที่ความถี่ 2.45 GHz การกวาดลำคลื่นทำด้วยสองการศึกษา โดยการศึกษาแรกเป็นสายอากาศยาคี-อูตะที่สามารถเปลี่ยนทิศทางการแผ่พลังงานได้ และชุดที่สองเป็นสายอากาศแถวลำดับแบบจัดเฟสที่ใช้ส่วนประกอบสายอากาศยาคี-อูตะที่สามารถเปลี่ยนทิศทางการแผ่พลังงาน สำหรับสายอากาศยาคี-อูตะที่สามารถเปลี่ยนทิศทางการแผ่พลังงานถูกออกแบบบนแผ่นพิมพ์ FR-4 และไดโอดพิน (PIN diode) ติดตั้งบนองค์ประกอบรับการป้อน (Driven element) ของสายอากาศและองค์ประกอบปรสิต (Parasitic element) การเปลี่ยนทิศทางของลำคลื่นหลักทำได้โดยการสลับสถานะไดโอดพินระหว่างเปิดและปิด ทำให้เกิดลำคลื่นหลักชี้ไปสู่ทิศทาง 45° 135° 225° และ 315° ตามลำดับ สายอากาศที่สามารถเปลี่ยนทิศทางการแผ่พลังงานนี้ถูกนำไปใช้ในงานเซ็นเซอร์สองชนิด พบว่าสามารถช่วยตรวจสอบได้หลายเป้าหมายทำให้ลดค่าใช้จ่ายและเพื่อช่วยปรับเทียบระบบ (Calibration) สำหรับการตรวจสอบวัตถุขนาดใหญ่ สำหรับสายอากาศแถวลำดับแบบจัดเฟสที่ใช้ส่วนประกอบสายอากาศยาคี-อูตะที่สามารถเปลี่ยนทิศทางการแผ่พลังงานใช้หลักการของแถวลำดับแบบเส้นสององค์ประกอบที่ใช้ตัวเปลี่ยนเฟสแบบ 1 บิตเพื่อให้มีการสูญเสียที่น้อยที่สุดในระบบการป้อน ในงานวิจัยนี้ได้แสดงให้เห็นศักยภาพที่จะใช้สายอากาศยาคี-อูตะที่สามารถเปลี่ยนทิศทางการแผ่พลังงานเพื่อเพิ่มมุมการกวาดการรับสัญญาณของสายอากาศแถวลำดับการทำงานของสายอากาศแถวลำดับใช้รูปแบบลำคลื่นของสายอากาศยาคี-อูตะที่สามารถเปลี่ยนทิศ

ทางการแผ่พลังงานที่นำเสนอและสถานะไดโอดพินของตัวเปลี่ยนเฟสแบบ 1 บิต ผลการทดสอบแสดงให้เห็นได้ว่าสายอากาศแถวลำดับทำงานที่ความถี่ 2.45 GHz สามารถกวาดลำคลื่นหลักไปยังแปดทิศทางด้วยความแปรปรวนอัตราขยายที่ต่ำ สายอากาศแถวลำดับแบบจัดเฟสนี้ถูกใช้ในรีเฟล็กต์อิมิตเตอร์แบบกวาดลำคลื่นซึ่งสามารถรับคลื่นที่กระจายจากหลายทิศทางรอบผลสัมผัสที่สะท้อนโดยตัวสะท้อนทรงกรวย เพื่อเก็บข้อมูลที่ใช้ในการคำนวณค่าดัชนีไรเซียน (Rician k -factor) ระบบถูกทดสอบด้วยดินน้ำมันทรงกลมและสัมจริง พบที่ว่าระบบที่ใช้สายอากาศแถวลำดับแบบแปรลำคลื่นให้ผลดีกว่าระบบที่ใช้สายอากาศแถวลำดับแบบสี่ลำคลื่น สำหรับการทดสอบสัมจริงความแม่นยำของการคัดแยกอยู่ในระดับ 85% ระบบนี้มีประโยชน์สำหรับการควบคุมคุณภาพของการผลิตส้มเขียวหวานและผลิตภัณฑ์ทางการเกษตรอื่นได้

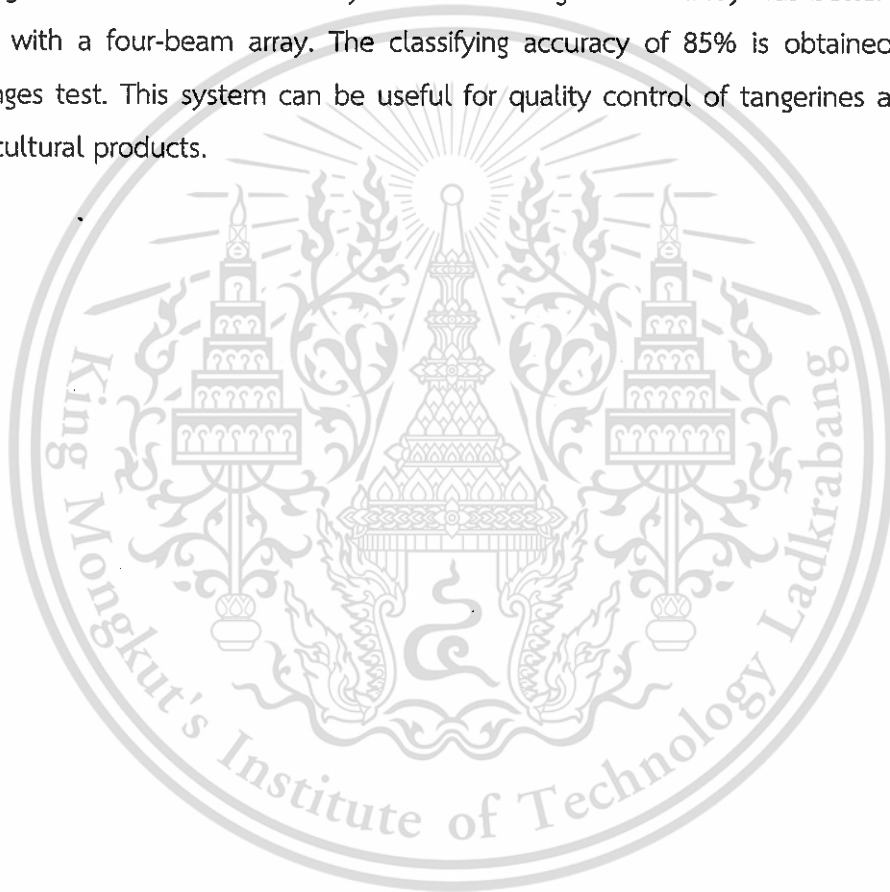


Thesis title	Pattern reconfigurable Yagi-Uda antennas and applications
Student	Mr. Chainarong Kittiyapunya
Student ID.	56601008
Degree	Doctor of Engineering
Program	Electrical Engineering
Year	2017
Thesis advisor	Professor Dr. Monai Krairiksh

ABSTRACT

The problem of defected agricultural product causes loss of vendor's revenue, hence a non-destructive sensor that can identify the quality non-destructively is highly desirable. To cope with this problem, this dissertation presents the application of the pattern reconfigurable Yagi-Uda antenna to accomplish the desirable sensor system. In this dissertation, the sensor system is designed based on beam-scanning reflectometer operating at 2.45 GHz. The beam-scanning is carried out with two series of studies. The first one is a pattern reconfigurable Yagi-Uda antenna whereas the other one is a phased array using pattern reconfigurable Yagi-Uda antenna as elements. The pattern reconfigurable Yagi-Uda antenna is designed on an FR-4 printed circuit board (PCB) and PIN diodes are attached onto the antenna's driven elements and parasitic elements. The direction of the main beam is shifted by alternating the PIN diodes' status between ON and OFF and results in main beam directing toward the directions of 45° , 135° , 225° , and 315° , respectively. Furthermore, this pattern reconfigurable antenna was applied for two sensor applications. It was found that the antenna can assist in detecting multiple targets for cost reduction and calibrating the system for measuring a large-size material. The phased array using pattern reconfigurable Yagi-Uda antenna elements is based on two-element linear array equipped with 1-bit phase shifters for lowest loss in feeding network. It is experimentally studied to illustrate the potential of using pattern reconfigurable Yagi-Uda antenna for increasing scan angle of the phased array

antenna. The operation of the array antenna utilizes beam patterns of the proposed pattern reconfigurable Yagi-Uda antenna and PIN diodes' status of 1-bit phase shifters. Measured results show that the array antenna can scan main beam toward eight directions with low gain fluctuation at the operating frequency of 2.45 GHz. This phased array antenna is utilized in a beam-scanning reflectometer that scattered waves from several directions around an orange reflected by a conical reflector are measured by the proposed phased array antenna. The collected data are used to calculate the Rician k -factor. The system was tested with plasticine spheres and real oranges. It was found that the system with an eight-beam array was better than the one with a four-beam array. The classifying accuracy of 85% is obtained for real oranges test. This system can be useful for quality control of tangerines and other agricultural products.



ACKNOWLEDGMENTS

First and foremost, I would like to give my deep gratitude to my advisor, Prof. Monai Krairiksh, for his consistent guidance, extraordinary patience, and unreserved support. I could not have gone this far without the endless help I got from him. I feel extremely fortunate to have him as my advisor and my mentor who made me open up my vision for research area and well beyond just the antenna design. I would also like to express my sincere gratitude to Assoc. Prof. Chuwong Phongcharoenpanich for his invaluable support and guidance. This dissertation would not have been possible without their advice and encouragement.

I would like to show gratitude to all my teacher at Joseph Upatham School, Kanjanapisek Witthayalai Nakornphathom School, King Mongkut's University of Technology Thonburi, and King Mongkut's Institute of Technology Ladkrabang who gave knowledge in academic matters and helpful guidance in living.

I would like to thank all my colleagues in Wireless Communication Laboratory, Dr. Thunyawat Limpiti, Dr. Tanawut Tantisopharak, Dr. Paiboon Yoiod, Dr. Prapan Leekul, and Mr. Chattapon Rienthong for their kind supports and providing a friendly atmosphere during the work. Also, I am grateful to all members in Innovative Antenna and Electromagnetic Applications Research Laboratory for their helpful assistance and a good friendship.

Many thanks also go to Dr. Noraset Wichaipanich, Dr. Parinya Soontornwong, Dr. Siraporn Sakphrom, and Ms. Atcharawan Sukkua for their helpful suggestions and kind support.

I would like to thank Mr. Vichit Lohprapan and Mr. Pratana Kangsadal for their kind suggestions, discussion, and support in English proofreading.

Finally, I would like to give my deepest gratitude to my parents, my relatives, my friends and Ms. Nisachon Choknakawaro for their loves, suggestions, support and prayer.

Chainarong Kittiyapunya

TABLE OF CONTENTS

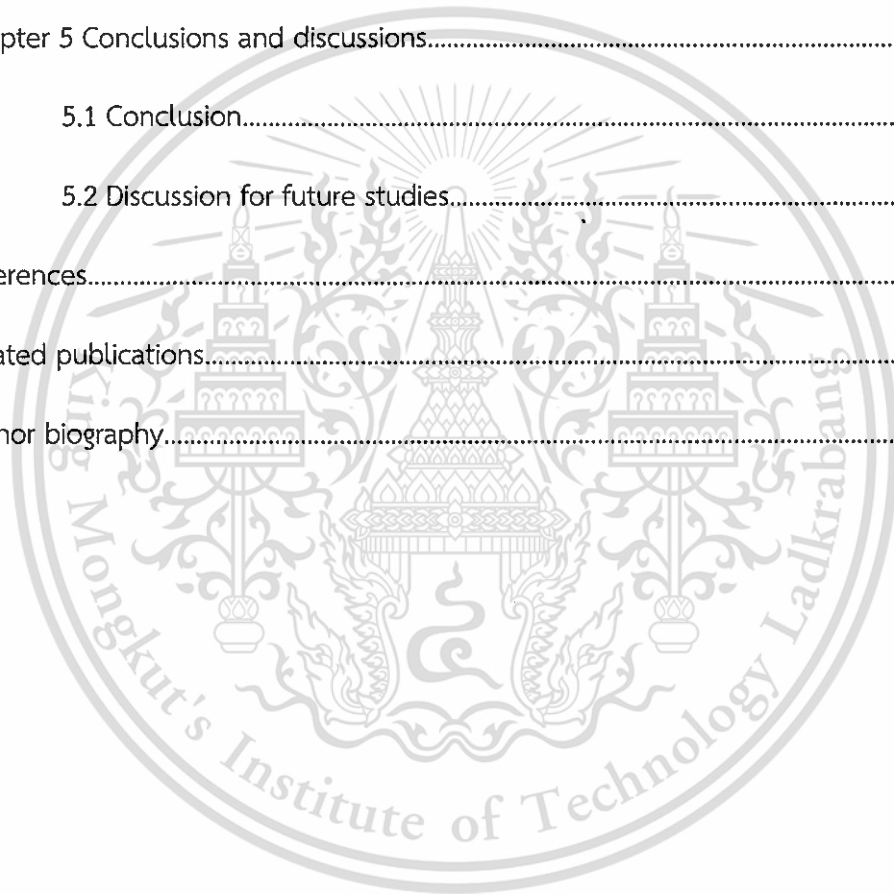
	Page
Thai abstract.....	I
English abstract.....	III
Acknowledgments.....	V
List of tables.....	IX
List of figures.....	XI
Chapter 1 Introduction.....	1
1.1 Problem statement and motivation.....	1
1.2 Dissertation organization.....	6
Chapter 2 Theoretical background.....	8
2.1 Introduction.....	8
2.2 Characteristic of orange.....	8
2.2.1 Orange anatomy.....	8
2.2.2 Dielectric properties.....	10
2.2.3 Judgement of orange property.....	13
2.3 Propagation channel.....	16
2.4 Reflection measurement.....	21
2.5 Scattered wave from a non-uniform dielectric.....	25
2.6 Conclusion.....	28
Chapter 3 Phased array using pattern reconfigurable Yagi-Uda antennas.....	30
3.1 Introduction.....	30

TABLE OF CONTENTS (continued)

	Page
3.2 Pattern reconfigurable Yagi-Uda antenna.....	30
3.2.1 Yagi-Uda antenna.....	32
3.2.2 Configuration of the pattern reconfigurable Yagi-Uda antenna.....	41
3.2.3 Pattern reconfigurable antenna design.....	46
3.2.3.1 Main beam in region 1 (the 135°-direction main beam).....	46
3.2.3.2 Main beam in region 2 (the 45°-direction main beam).....	49
3.2.3.3 Main beam in region 3 and 4 (the 310° and 225°-direction main beams).....	50
3.2.4 Simulation and measured results.....	54
3.2.5 Applications.....	59
3.3 Phased array antenna using pattern reconfigurable Yagi-Uda antennas...63	
3.3.1 Linear array antenna.....	65
3.3.2 Design of phased array with pattern reconfigurable antennas.....	67
3.3.3 Feed system of the proposed array antenna.....	73
3.3.4 Implementation of the proposed array antenna.....	76
3.4 Conclusion.....	79
Chapter 4 Implementation of beam-scanning reflectometer.....	81
4.1 Introduction.....	81
4.2 Sensor system design.....	81
4.3 Experimental results.....	87

TABLE OF CONTENTS (continued)

	Page
4.3.1 Results from a plasticine model with one missing section.....	87
4.3.2 Results from real tangerine fruits.....	93
4.4 Conclusion.....	96
Chapter 5 Conclusions and discussions.....	98
5.1 Conclusion.....	98
5.2 Discussion for future studies.....	99
References.....	100
Related publications.....	106
Author biography.....	107



LISTS OF TABLES

Table	Page
1.1 Harvesting quantities of each season in Thailand.....	1
2.1 Juice properties of normal tangerines.....	15
2.2 k-factors for different numbers of receiving antennas.....	27
3.1 Mode of PIN diodes (ON/OFF) on the parasitic elements for the 135°-direction main beam (region 1).....	47
3.2 Mode of PIN diodes (ON/OFF) on the parasitic elements for the 225°-direction main beam (region 4).....	51
3.3 Optimal specifications/dimensions of the prototype antenna.....	54
3.4 Status of PIN diodes by region of the main beam.....	54
3.5 Magnitude of reflection coefficient for aluminum plate in each main beam.....	62
3.6 Operation of the array antenna.....	72
3.7 Simulated radiation characteristics of eight-beam antenna.....	72
3.8 Characteristic of one-bit phase shifter at 2.45 GHz.....	75
3.9 Measured radiation characteristics of eight-beam antenna.....	79
4.1 Calculated results of received power and signal-to-noise ratio.....	86
4.2 Propagation channel of 6-cm plasticine model with a missing section measured by the 8-beam antenna system.....	89
4.3 Propagation channel of 6-cm plasticine model with a missing section measured by the 4-beam antenna system.....	90
4.4 Propagation channel of 8-cm plasticine model with a missing section measured by the 8-beam antenna system.....	91

LISTS OF TABLES (continued)

Table	Page
4.5 Propagation channel of 8-cm plasticine model with a missing section measured by the 4-beam antenna system.....	92



LISTS OF FIGURES

Figure	Page
1.1 Flesh of granulated tangerine.....	2
2.1 Anatomy of orange.....	9
2.2 Representation of charge densities by field vector.....	10
2.3 Torque acting of electric dipole.....	11
2.4 Electric dipole moment.....	12
2.5 Experiment of normal and granulated tangerine with a dielectric probe.....	14
2.6 Dielectric properties of normal and granulated tangerine at 2.45 GHz.....	15
2.7 Propagation environment between a transmitter and a receiver: (a) Line-of-sight (b) Non-line-of-sight.....	17
2.8 Three scales of mobile signal variation.....	18
2.9 Structure of reflectometer: (a) Monostatic reflection (b) Bistatic reflection	22
2.10 Incident wave and reflected wave for material interface: (a) Spherical dielectric (b) Plane dielectric.....	22
2.11 Reflection coefficient versus dielectric constant by varying angle of incident wave.....	24
2.12 Model of granulated tangerine	26
2.13 Simulation to determine the optimum number of receiving antennas.....	27
3.1 Structure of Yagi-Uda antenna.....	33
3.2 Phasor diagram of impedance.....	34
3.3 Thin dipole for near field analysis.....	34
3.4 Mutual coupling of antenna.....	35

LISTS OF FIGURES (continued)

Figure	Page
3.5 Phasor diagram of induction between driven and parasitic elements.....	37
3.6 Thin dipole for far field analysis.....	38
3.7 E-plane amplitude patterns for Yagi-Uda antenna for varied F_{21} and F_{31}	40
3.8 Proposed antenna: (a) schematic of pattern-reconfigurable Yagi-Uda antenna, (b) the driven elements and PIN diode circuit, (c) microstrip-to-CPS transition (balun).....	42
3.9 Characteristics of the Philips BAP50-02.....	42
3.10 PIN diode equivalent circuit (a) the ON state, (b) the OFF state.....	43
3.11 Simulated result of isolation between DC circuit and RF signal.....	43
3.12 Current distribution on CPS and driven element.....	44
3.13 Simulation results of the two-port back-to-back configuration of the microstrip-to-CPS transition.....	45
3.14 Simulation results of radiation patterns (E-plane) in each cases of Table 3.1.....	47
3.15 Simulation results in case of distance variation (S_1 and S_2) for the main beam in region 1: (a) gain and sidelobe level relative to distance, (b) $ S_{11} $ and frequency relative to distance.....	48
3.16 Simulation results in case of director length variation (L_{dir1} , L_{dir2} , L_{dir3} , L_{dir4}) for the main beam in region 1: (a) gain and sidelobe level relative to length, (b) $ S_{11} $ and frequency relative to length.....	49

LISTS OF FIGURES (continued)

Figure	Page
3.17 Simulated $ S_{11} $ for the main beam in region 2: Incident 1 is when the biasing voltages at V_1, V_3, V_7, V_8 and at V_2, V_4, V_5, V_6 are 5 and 0 volts respectively; Incident 2 is when the parasitic elements functions are manipulated with the biasing voltage at V_1, V_3, V_5, V_7, V_8 and at V_2, V_4, V_6 are 5 and 0 volts, respectively.....	50
3.18 Simulated $ S_{11} $ for the main beam in region 3 and 4.....	51
3.19 Simulation results in case of distance variation (S_1) for the main beam in region 4: (a) gain and sidelobe level relative to distance, (b) $ S_{11} $ and frequency relative to distance.....	52
3.20 Simulation results in case of director length variation (L_{dir3} and L_{dir4}) for the main beam in region 4: (a) gain and sidelobe level relative to length, (b) $ S_{11} $ and frequency relative to length.....	53
3.21 Simulated effects of varying director lengths (L_{dri3} and L_{dri4}) on the main beam in region 2.....	53
3.22 Photographs of the prototype antenna (a) Top view (b) Side view.....	55
3.23 Simulated $ S_{11} $ for the main beams in different regions.....	56
3.24 Measured $ S_{11} $ for the main beams in different regions.....	56
3.25 Simulated results of radiation patterns at 2.45 GHz: (a) E-plane, (b) H-plane.....	57
3.26 Measured results of radiation patterns at 2.45 GHz: (a) Eplane, (b) H-plane.....	58
3.27 Diagram of the beam switching reflectometer for detecting multiple objects.....	60
3.28 Measurement of two targets which locate in different direction: (a) Azimuth patterns at 2.45 GHz, (b) Magnitude of reflection coefficient for different moisture content.....	61

LISTS OF FIGURES (continued)

Figure	Page
3.29 Diagram of the beam switching reflectometer for calibration system.....	62
3.30 Magnitude of reflection coefficient for different moisture content of paper stack.....	63
3.31 Configuration of linear phased array.....	66
3.32 Geometry of the phased array of pattern reconfigurable antennas.....	68
3.33 Simulation results in case of distance variation (d) for the main beam in 'Beam 1' and 'Beam 2': (a) gain relative to distance, (b) sidelobe level relative to distance.....	69
3.34 Simulation results in case of phase variation for the main beam in 'Beam 2' and 'Beam 4': (a) gain relative to phase difference, (b) sidelobe level relative to phase difference.....	70
3.35 Simulated radiation characteristics of the eight-beam array.....	72
3.36 Circuit of the designed 1-bit phase shifter.....	74
3.37 Prototype of the 1-bit phase shifter.....	75
3.38 Equivalent transmission line circuit of the Wilkinson power combiner.....	76
3.39 Prototype of the two way power combiner.....	76
3.40 Photographs of the phased array antenna: (a) Top view, (b) Side view, and (c) feeding system.....	77
3.41 Measured results of the phased array antenna. (a) $ S_{11} $ for different main beams. (b) Gain patterns.....	78
4.1 Configuration of the beam-scanning reflectometer.....	82
4.2 Radiation patterns at different distances.....	83

LISTS OF FIGURES (continued)

Figure	Page
4.3 Radiation pattern of 'Beam1' with a conical reflector.....	83
4.4 Measured result of MAX4003 characteristic.....	85
4.5 Photograph of the proposed system.....	86
4.6 Photographs of objects under test: (a) real tangerine and (b) plasticine with a missing section.....	88
4.7 Photograph of calibration with a metallic ball.....	89
4.8 Flesh of tangerine fruits. (a) Normal; (b) Granulated.....	94
4.9 Measured results from normal and granulated tangerine fruits: (a) mean; (b) variance; and (c) k-factor.....	95

CHAPTER 1

INTRODUCTION

1.1 Problem statement and motivation

The citrus fruits have many nutrients and medicinal value which have been recognized since ancient times. From report of Food and Agriculture Organization of the United Nations (FAO), it has a progressive tendency for planting citrus fruits. The citrus fruits are the most produced fruit and are grown in more than 80 countries. Thailand is a country which produces citrus fruits, such as orange, pomelo, lemon, and lime. Especially, orange is produced more than other types. The sweet and sour flavor of orange made it so popular and widely consumed throughout the world. In addition, orange is an export product of Thailand that got US\$ 30.11 million worth in the year 2015 [1]. Meanwhile, importing orange had a cost of US\$ 130.54 million in the year 2015. Regarding this, orange is one of the major fruits which has a high value of trading.

Table 1.1 Harvesting quantities of each season in Thailand [2]

First half of the year	Jan.	Feb.	Mar.	Apr.	May	Jun.
Orange (%)	41.02	5.64	0.89	1.32	0.49	0.90
Second half of the year	July	Aug.	Sep.	Oct.	Nov.	Dec.
Orange (%)	1.93	1.08	0.51	0.74	11.44	34.04

An orange is a native fruit and cultivated in all regions of Thailand. The harvesting quantity of orange in Thailand shown in Table 1.1 was 100,145 tons in the year 2015. It is observed that orange can be produced throughout the year. It is mostly produced in January (41.02%) and December (34.04%). For species in Thailand, tangerine is popular for planting in this zone.

As previously informed, orange is the exporting and importing product which makes revenue to vendors. This revenue will be assessed with quality of fruits which will have chances to get good and defective fruit. A common problem with harvested orange is granulation. Granulation will occur when lacks of water and delayed harvesting [3]. This disorder results in the juice vesicles in some parts of the fruits dry out and become tough [4]. Furthermore, their lower acid and sugar content cause defective fruits to taste bad and be unsaleable. A granulated orange is shown in Fig. 1.1. This defective fruit causes loss of revenue and may be blacklisted from trading partner. Therefore, the quality control of orange must be made before trading.



Fig. 1.1 | Flesh of granulated tangerine

The current technique of quality control can be done by counting the number of days after anthesis as an indication of orange harvest. This takes about 26-30 weeks. In addition, weighing by the hands and observation of peel are also an indicator. The granulated orange is lighter than the normal one. However, accuracy of these techniques depend on the human expertise and the reliability of these techniques greatly relies on person whose decision can be wrong.

Many years ago, many researchers have attempted to develop sensors to overcome limitation for quality control of orange. The biochemical properties can be used to determine quality of orange such as total soluble solid (TSS) and acidity (A) [5]. The total soluble solid indicates the sweetness of fruit whereas acidity indicates sourness. This method is accurate but their weakness is that it must destroy sample of fruit that is not suitable in practice. In addition, the physical properties of orange

This material is reserved for educational use only, not allowed for commercial use.

Forbidden to modify the content, and cite the document when use.

are another indicator of quality. There have been some studies in the change of physical appearance such as color of peel, size, aroma, firmness, dry weight, and specific gravity [6]-[10]. Insoluble solids have already been demonstrated to determine quality of orange [6]. They were determined by measuring dry weight residues of pellets obtained from centrifugations of orange juice. The ratio of dry weight to original juice weight represented the insoluble solids content. However, this method requires the destruction of fruit under test. The non-destructive measurement such as the specific gravity of an orange can be calculated from the ratio of the weight of an orange to that of water for an equivalent volume [7]. It was found that the specific gravity of the whole orange had low correlation coefficient with the soluble solids (Brix), including complexity for preparing equipment. Meanwhile, the electronic nose technology had a possibility to utilize information on behavior aroma to assess orange ripening stage. It has been demonstrated by using an array of 10 different metal oxide sensors positioned into chamber [8]. Each orange was placed into an airtight jar and then the sampled gas evaporated into the sensor chamber. The obtained results prove that the electronic nose can be possible to distinguish an orange's ripeness. In addition, the acoustic impulse response method has been investigated for monitoring an orange firmness change during storage [9]. It was generated by tapping fruit from pendulum plastic ball. Then, a piezoelectric film transducer was utilized to detect the resonance signal and to analyze the frequency domain for an orange fruit. The result suggests that the dominant resonant frequency, stiffness coefficient, and elasticity coefficient decrease with storage time. However, the detected aroma and acoustic impulse response may be disturbed by environment and position of measurement. It must be a closed system. Thus, these methods are not suitable for the industry which requires to detect continuously. Moreover, the color of peel is one of the attributes of the fruit product. It has been developed by using the color index of citrus fruits (CCI) [10]. This system was compared with the measurement obtained using a spectrophotometer. The color of an orange was measured by the imaging system using two different algorithms: from the average of the CCI values and from the average RGB value. The well correlations were achieved in the both algorithms. However, the results may be wrong since color is influenced by sunlight. Another attempt utilizes the size and number of oil gland which locates in peel surface [11]. It is an indicator to determine the stage of

maturity of orange. This method expects to eliminate error for color on surface that occurs from sunlight. Nevertheless, this method requires a good setup and still be only the study on piece of peel.

Several techniques are quite accurate such as, X-ray [12], nuclear magnetic resonance (NMR) [13], and magnetic resonance imaging (MRI) [14]. These techniques can scan internal factors of orange and they can accurately justify for classifying defective fruit. However, these techniques have not been extensively used for the industry due to the high cost of measuring instrument. In the meantime, visible (VIS) and near-infrared (NIR) band are used to estimate quality of orange [15]-[17]. It has been widely applied for the quality control of vegetable and fruit. The spectrums of VIS/NIR band incident on fruit will be absorbed depends on fruit characterization. This results in difference of output energy and it associates with either biochemical or physical properties. However, this technique has to direct contact between a transceiver and a fruit under test. It is not suitable for fruit mounted on a conveyor belt in a continuous process.

In the case of microwave frequency band, microwave sensor has already been developed for orange flavor-testing [18]. An orange is located between a transmitter and a receiver. The signal is transmitted to the fruit and then penetrates to the receiver. Moreover, microwave sensor operating at 2.45 GHz has been presented for checking granulated fruit. It measures reflected and scattered waves from a fruit that is rotated around its axis [19]. Due to the different dielectric properties between normal and granulated fruits, the mean (M) and standard deviation (S.D.) of the reflected and scattered waves are different, and the M/S.D. ratio can be a good indicator of granulation. It is noted that microwave frequency band can scan into flesh of orange and operate in non-contact manner.

Recently, Rician k-factor that plays an important role in wireless communications has been applied for identifying the maturity stage of fruits [20]. This method utilizes statistical data of received waves from around the fruit and k-factor is calculated from these data. It can obviously classify maturity stage of fruit. Therefore, k-factor can be applied to detect granulation.

Furthermore, the inspection is required with continuous process. A reflectometer technique is a good option due to contactless gauge and appropriate for conveyor belt system. This technique transmits electromagnetic wave to an object and measures the reflected wave that can reveal the object's property [21]. For example, a millimeter reflectometer has already been developed for sensing sweetness of apples [22]. A vector reflectometer using antenna mixers has also been proposed for mango classification [23]. The radiation pattern of a reflectometer is generally fixed but microwave sensor using Rician k-factor requires scanning system around the fruit. Mechanical scanning and electronic scanning are alternative that can be used to measure around the fruit. Nevertheless, mechanical scanning unavoidably causes wear and tear whereas electronic scanning seldom confronts with this problem.

According to aforementioned, electronic scanning can be carried out by using a beam scanning antenna. Beams can be scanned by several means, one of which is array antenna. Since a practical sensor system should have low loss as well as not too complex and expensive, a phased array of pattern reconfigurable antennas equipped with one-bit phase shifters has been proposed for this purpose [24]. However, as there are only two radiation patterns of pattern reconfigurable antennas, the number of the beams that can be scanned is limited. Increasing number of beam will assist scanning that covers around the fruit. Thus, antenna element of array should be developed for reducing this limit.

To enhance antenna pattern of phased array, wire antenna can be developed to address the issue and we have presented a four beam-pattern reconfigurable Yagi-Uda antenna [25]. This antenna is comprised of two pairs of dipole and four parasitic elements arranged in uniform end-fire array. To achieve four beams for UHF TV signal reception, the parasitic elements are required to function in correspondence with the operating dipoles. This know-how will be used to develop for increasing beam of the phased array antenna. In addition, pattern reconfigurable Yagi-Uda antenna is possible to utilize for other application such as, measuring material for different position, and assisting in calibration of a sensor system.

Consequently, the objective of this dissertation is to develop a microwave sensor system using a beam-scanning reflectometer. Rician k-factor is utilized to

detect granulated orange. To obtain statistical data for calculating k-factor, a reflectometer technique has to be developed from fixed beam into scanning beam. This novel concept will be managed by using a phased array of pattern reconfigurable Yagi-Uda antennas equipped with one-bit phase shifters. Also, number of beam must be suitable for measuring various positions around the fruit. The pattern reconfigurable Yagi-Uda antenna element of the phased array is a major factor to improve number of beams. It is designed and fabricated for using in phased array. Then, validation of beam-scanning reflectometer is investigated with a model and real oranges. Furthermore, pattern reconfigurable Yagi-Uda antenna can be useful for other applications. It will be used, to measure material in different positions, and to assist calibration of a sensor system.

1.2 Dissertation Organization

From the problem statement, the goal of this work is to enhance shortcoming of the previous works for classifying granulated fruit. In order to overcome, the design of novel beam-scanning reflectometer that differs from the traditional reflectometer is presented. The further detail of design will be organized as follows:

Chapter 2 exhibits characteristic of orange and dielectric properties of granulated and normal oranges. Also, this chapter describes methodology of beam-scanning reflectometer which is based on Rician k-factor. Moreover, the concept of technique and information of orange is simulated for comparing the effects of varying the number of receiving signals on calculated k-factor.

Chapter 3 presents design of a phased array using pattern reconfigurable Yagi-Uda antenna in order to utilize in beam-scanning reflectometer. Rationale of the proposed antenna design is elaborated in section 3.1. The reconfigurable Yagi-Uda antenna is studied and fabricated, including performance of antenna for interested applications, as shown in section 3.2. Then, section 3.3 presented phased array using pattern reconfigurable Yagi-Uda antenna. It is also studied to achieve the highest performance. In addition, this section will show the process to steer the beam toward eight directions with low gain fluctuation.

Chapter 4 introduces system design and results of the beam-scanning reflectometer which is based on Rician k-factor. Each device of the system is estimated and presented in section 4.2. Then, the sensor system is tested with model and real oranges in section 4.3. The performance of the sensor system has been shown to confirm that the beam-scanning reflectometer can detect granulated orange accurately.

Finally, summary of all presentations in this dissertation and discussion on the remark for future work are presented in chapter 5.



CHAPTER 2

THEORETICAL BACKGROUND

2.1 Introduction

This chapter elaborates characteristic of oranges together with an understanding of dielectric properties related to electromagnetic wave. Also, dielectric properties and total soluble solids of normal and granulated oranges have been measured which leads to application in quality determination. Dielectric properties of fruit can be analogous to environment within propagation channel. How to obtain Rician k-factor for quality inspection of propagation channel will be discussed along with a reflectometer. Furthermore, this chapter elaborates the concept of a novel sensor system, including simulated effect of varying number of receiving antennas on calculated k-factor.

2.2 Characteristic of orange

The structure of orange has been studied to comprehend its nature. Each part has different compositions, both of physical and chemical properties. Also, the disorder of orange will arise a change of properties. Therefore, anatomy and properties of orange should be acquainted before subsequent explanation.

2.2.1 Orange anatomy

An orange is the fruit of citrus genus in the family of rutaceae. Its feature is a spherical or ellipsoid which diameter is related to species. For example, diameter of tangerine species has been measured and the diameter is between 5 and 7.5 cm. Fig. 2.1 shows anatomy of orange. Oranges are composed of an outermost flavedo layer that contains the exterior fruit color and many oil glands that protect the fruit from bugs and microorganism. A subsequent layer is a white spongy albedo layer. These

layers are also known as rind. The surface of rind is smooth curve. The rind thickness depends on each species, such as 0.8-1.2 mm thickness for tangerine species, and 4-6 mm thickness for navel species, etc. Under rind layer are the flesh segments, divided by segment wall (membrane). The flesh of orange behaves as semi-solid dielectric. The average number of flesh segment is mostly ten segments. Seeds contain inside the flesh of orange. Each segment is consisted of many juice vesicles that are elongated and attached to the central core of orange. The juice vesicles provide juicy water that has many nutrients, including sweetness and sourness of fruit [26].

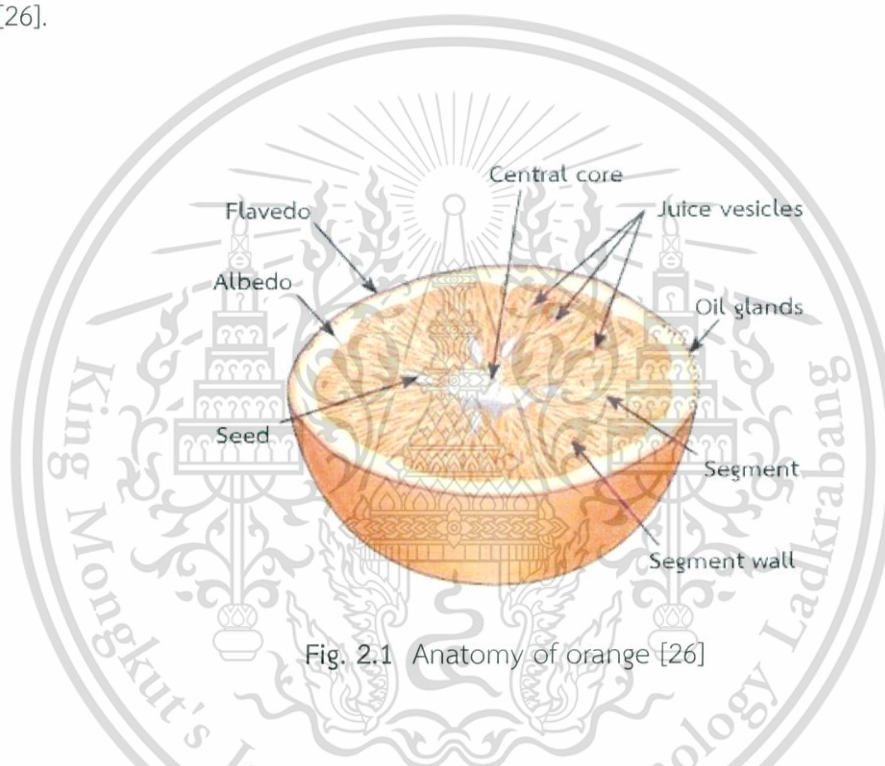


Fig. 2.1 Anatomy of orange [26]

Those segments will have a chance to be granulation because of lack of water and delayed harvest. Granulation is a physical disorder in orange that results in decreasingly extracted juice and sometimes withered vesicle. This disorder will form gel within vesicles which causes dry and tough. While sunburn and freezing are another reason for loss of juice. These events obtain from cellular collapse and tissue death which is not concern for gel formation. In addition, flavor of granulated fruit is bad since their acid and sugar are very low. These effects show different biochemical between normal and unusual fruit [3]-[4].

2.2.2 Dielectric properties

Since the components of orange are dielectric material, basic knowledge is explained to relate between dielectric and electric field, including association within particle of dielectric material. From these knowledges, it can lead to utilize for identifying dielectric properties [27].

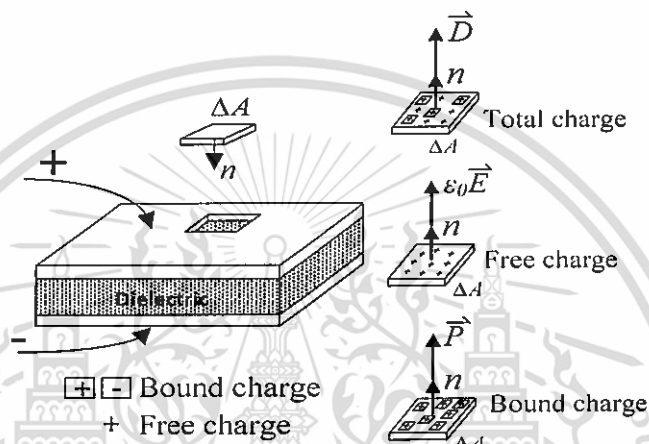


Fig. 2.2 Representation of charge densities by field vector [27]

Ideal dielectrics do not contain "free" or mobile charges like behavior of conductor. However, dielectrics contain bound charges which it will react to external electric field (E). To analyze dielectric, a condenser is utilized for representation of this condition. A dielectric is set between two plates that feed with opposite pole, as shown in Fig. 2.2. The vector of total charge densities (ρ_t) comprises vector of bound charge density (ρ_p) and vector of free charge density (ρ_f). The total charge densities represent vector by the electric flux density (D), known as dielectric flux density. Thus, surface charge density will be the normal component of D on the surface area (ΔA) of unit volume.

$$\rho_t \Delta A = |D| \cos\theta \Delta A = D \cdot \hat{n} \Delta A = \vec{D}_n \Delta A \quad (2.1)$$

Similarly, free charge density is $\frac{\rho_t}{\epsilon_r}$ and represented by vector of applied electric field intensity (\vec{E}) as follows:

$$\frac{\rho_t}{\epsilon_r} \Delta A = \frac{\rho_t}{\epsilon} \epsilon_0 \Delta A = \epsilon_0 E \cdot \hat{n} \Delta A = \epsilon_0 \vec{E}_n \Delta A \quad (2.2)$$

where ϵ is complex permittivity of the medium, ϵ_0 is permittivity of free space (8.854×10^{-12} farad/m), ϵ_r is complex relative permittivity of the medium ($\epsilon_r = \frac{\epsilon}{\epsilon_0}$), and the symbol \hat{n} is unit vector of normal component.

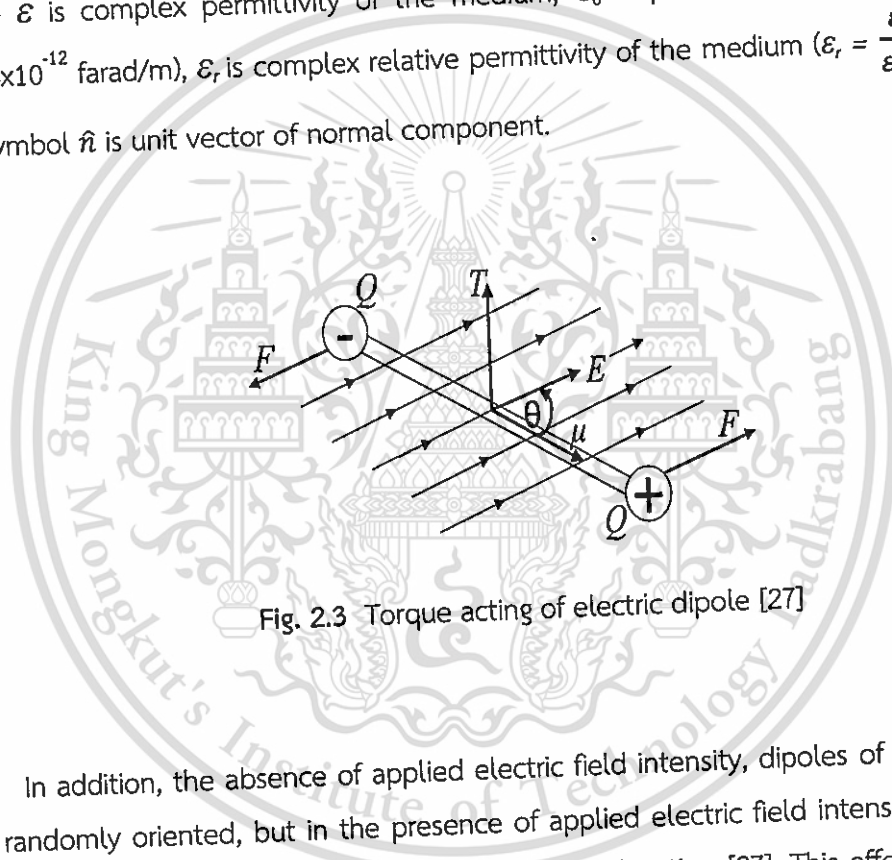


Fig. 2.3 Torque acting of electric dipole [27]

In addition, the absence of applied electric field intensity, dipoles of dielectric are randomly oriented, but in the presence of applied electric field intensity, these electric dipoles tend to align with the applied field direction [27]. This effect occurs from torque (T) that exercised by the electric field on an electric dipole moment (μ), as shown in Fig. 2.3. This event implies that electric field intensity causes electric dipole moment.

$$T = |\mu||E| \sin\theta = \mu \times E \quad (2.3)$$

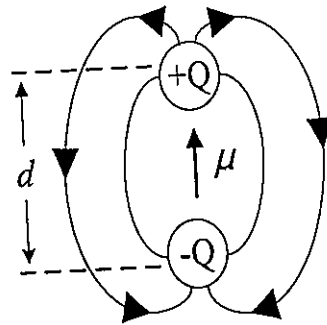


Fig. 2.4 Electric dipole moment

The electric dipole moment is vector of pointing from the negative to the positive pole, as shown in Fig. 2.4. It is defined by distance (d) between two electric charges ($\pm Q$) as equation 2.4. In addition, the whole vectors of electric dipole moment per unit volume ($\Delta V = d\Delta A$) within the dielectric material are identical with the vectors of surface charge density of bound charge (ρ_p), as called the polarization (\vec{P}).

$$\mu = Qd \quad (2.4)$$

$$\rho_p = \vec{P} = \frac{\sum \vec{\mu}}{\Delta V} = \frac{\sum Q_p \cdot \hat{n}}{\Delta A} \quad (2.5)$$

where $\sum Q_p$ is the total number of bound charge.

Equation 2.1 and 2.2 show the relationship between dielectric flux density and the electric field intensity, as $\vec{D} = \epsilon \vec{E}$. Moreover, dielectric flux density is the vector sum of bound charge density and free charge density which is shown in equation 2.6.

$$\vec{D} = \epsilon_0 \vec{E} + \vec{P} \quad (2.6)$$

Then, this equation will have a relation between complex relative permittivity and field vector as follows:

$$\vec{P} = \vec{D} - \epsilon_0 \vec{E} = (\epsilon - \epsilon_0) \vec{E} = (\epsilon_r - 1) \epsilon_0 \vec{E} = \chi \epsilon_0 \vec{E} \quad (2.7)$$

The factor χ is known as the electric susceptibility of dielectric material.

$$\chi = \frac{\vec{P}}{\epsilon_0 \vec{E}} = (\epsilon_r - 1) = \frac{\text{bound charge density}}{\text{free charge density}} \quad (2.8)$$

As abovementioned equations, complex relative permittivity ($\epsilon_r = \epsilon'_r - j \epsilon''_r$) is variable of dielectric material that can change value of three field vectors. The real of relative permittivity exhibits stored energy in a dielectric material that occurs from an external electric field, known as dielectric constant (ϵ'_r). On the other hand, the imaginary part of ϵ_r is dielectric loss factor (ϵ''_r) which accounts to relate loss of energy within dielectric material. Also, it is noted that the polarization vector can explain a relation between electric field and atom of material. Therefore, these dielectric properties are important factor for applying together with electric field, and it can be utilized for identifying properties of materials.

2.2.3 Judgement of orange property

Since dielectric properties influence to decay amplitude of fields, and may not penetrate to flesh of fruit. The frequency selection must be executed for suitable usability that wave can go through the rind. The evaluation of penetration depth (P_d) can exhibit the depth into the dielectric that the power flux has fallen to $1/e$ (36.8%) of the power entering the surface, and is given by [28]:

$$d_p = \frac{c}{2\pi f \sqrt{2\varepsilon_r'}} \frac{1}{\sqrt{\left(\sqrt{1 + \left(\frac{\varepsilon_r''}{\varepsilon_r'}\right)^2} - 1\right)}} \quad (2.9)$$

where c is the speed of light in free space ($3 \times 10^8 \text{ ms}^{-1}$), and f is frequency of the traveling wave.

Previous research study in [18], dielectric properties of tangerines with rind have been measured at 2.45 GHz. The dielectric constant and loss factor are 24 and 7, respectively. Then, these values can be useful to calculate penetration depth (P_d). It was found that penetration depth was 13.8 mm, and microwave operating at 2.45 GHz can penetrate to flesh of tangerines. Since thickness range of rind is from 0.8 to 1.2 mm. Therefore, 2.45 GHz frequency is utilized for data collection of dielectric properties and sensor system design.

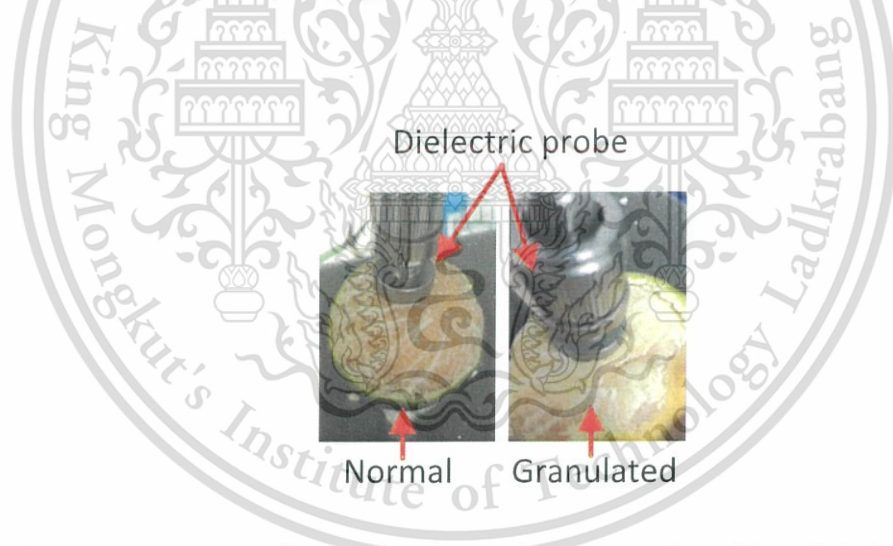


Fig. 2.5 Experiment of normal and granulated tangerine with a dielectric probe

Tangerine species was used as sample for measuring dielectric properties. The samples of tangerine fruit were peeled to see appearance of flesh, then those of tangerine were classified between normal and granulated tangerine. These fleshes of tangerines were measured with an Agilent 85070E dielectric probe [29] that was connected to an N9916A FieldFox microwave vector network analyzer [30]. The Agilent dielectric measurement software computed the dielectric properties from the

This material is reserved for educational use only, not allowed for commercial use.

Forbidden to modify the content, and cite the document when use.

reflection coefficient measured by the dielectric probe that was designed to measure flat-surface solid, liquid and semi-solid. Before measurement of tangerine samples, the dielectric probe was calibrated with air, a standard short circuit (85070-60003 shorting block), and distilled water. Measurements of samples for normal and granulated tangerines were made by placing the dielectric probe on the surface of the flesh samples, as can be seen in Fig. 2.5.

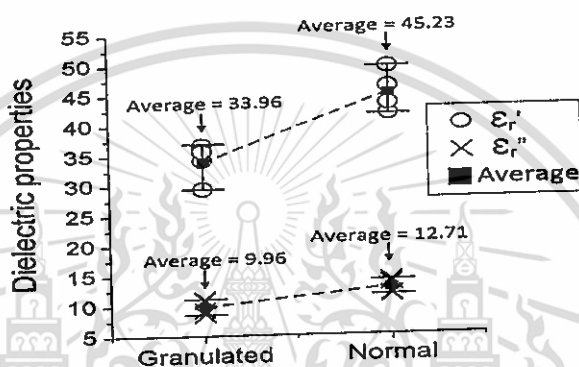


Fig. 2.6 Dielectric properties of normal and granulated tangerine at 2.45 GHz

Fig. 2.6 shows measured dielectric properties of normal and granulated tangerine. The dielectric constant and loss factor of the normal tangerines (45.23 and 12.71, respectively) were higher than those of the granulated ones (33.96 and 9.96, respectively) due to their higher water content. The acquired results obviously indicate difference between normal and granulated tangerine.

Table 2.1 Juice properties of normal tangerines

Tangerine	Properties		
	ϵ'_r	ϵ''_r	$^{\circ}\text{Bx}$
Normal juice	73.30-75.42	14.64-17.47	10.5-12
Average	74.44	16.11	11

Also, the normal fleshes were squeezed to measure dielectric properties and total soluble solids. However, juice of granulated fleshes cannot be measured since those fleshes have a few juice and dry. Table 2.1 shows dielectric properties and total soluble solids of normal juice. The dielectric constant and loss factor of normal juice were 74.44 and 16.11, respectively. It is noted that dielectric properties of juice are different from those of flesh because flesh comprises of water content and other components whereas juice is only water content. However, those for normal tangerines have higher water content than granulated tangerine. In addition, juices were used for measuring total soluble solids. It can be known as °Brix (°Bx) which indicates solids that are dissolved within a substance. A soluble solid is sucrose, glucose or other sugar solutions in fruits. The technique for measuring the concentration of total soluble solids is measurement of an index of refraction, as called refractometer. The total soluble solids was measured with an OPTIK handheld refractometer [31], and the results are revealed in °Brix. The °Brix values for normal tangerine were in range between 10.5 and 12 while those for the granulated tangerines were near zero. From the measured results, it was demonstrated that the normal tangerines were sweeter than granulated tangerines.

2.3 Propagation channel

The wireless communication is widely applied in cellular network, wireless sensor network, terrestrial TV, etc. To enhance performance of communication system, one of important factor is propagation channel which it can indicate quality of communication system. Propagation channel comprises a transmitter and a receiver, which transmits electromagnetic wave through any medium, as shown in Fig. 2.7. It is noted that travelling wave in direct path between the transmitter and the receiver is required for communication system, known as line-of-sight (LOS). On the other hand, the direct wave from the transmitter to the receiver is obstructed. This situation is called non line-of-sight (NLOS) propagation which is unpleasant in communication system. However, wave reception of the receiver is not necessary to obtain only direct path and obstructed path component. Since each area may have various environments which results in effect to propagation channel. These effects

must be accounted in order to understand and analyze the performance of wireless communication system.

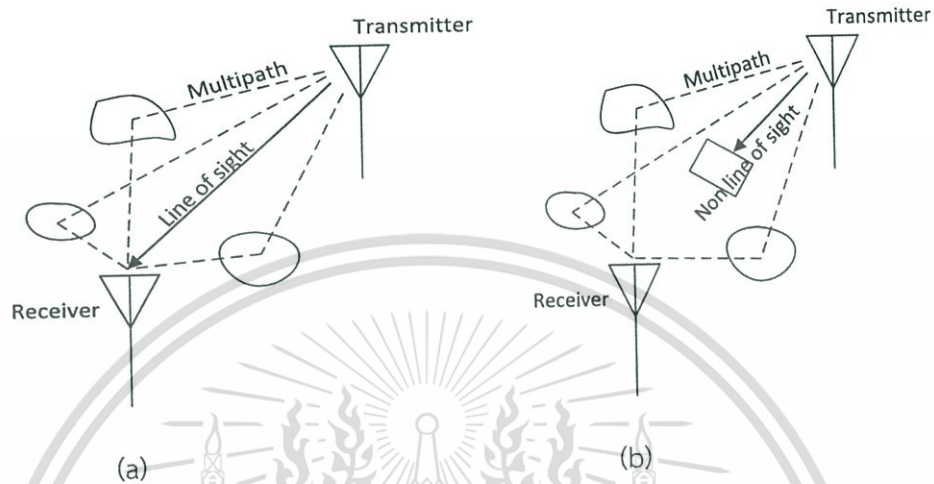


Fig. 2.7 Propagation environment between a transmitter and a receiver: (a) Line-of-sight (b) Non-line-of-sight

All effects are represented by noise source (undesirable) which arises from the various processes encountered by transmitted waves on their way from the transmitter to the receiver. Some of them are shown as follow [32]:

- Reflection (from the smooth surface of barrier and hills);
- Absorption (due to walls, canopy trees, and the atmosphere);
- Scattering (from rough surfaces such as ground and the leaves and branches of trees);
- Diffraction (by edges, hill top, rooftops, and buildings).

As above mentioned, the propagation channel is unavoidably faced with these effects. The noise can be subdivided in the channel into three types of fading, i.e. path loss, shadowing (or slow fading), and fast fading (or multipath fading) which each fading characterizes difference of extracted signal.

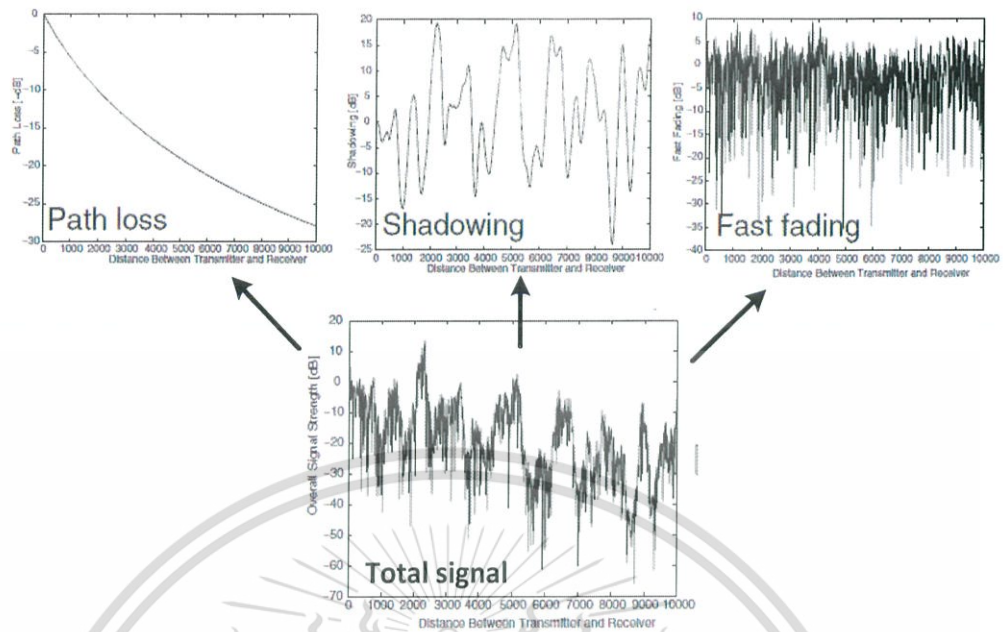


Fig. 2.8 Three scales of mobile signal variation [32]

An example of the three fading processes is illustrated in Figure 2.8 which shows received signal by a mobile receiver moving away from a transmitting base station. In general, path loss is defined as the attenuation of radiated signal from a transmitter dependent on the distance travelled path and various factors of the propagation channel. It is a well-known fact that the power of a signal decreases inversely proportional with the square of the distance from the transmitter. In addition, some positions will suffer increased loss, whereas others will be less obstructed and have an increased signal strength. This phenomenon is called shadowing or slow fading. It is noted that shadowing process is affected from obstruction within the channel. Another effect of propagation channel is fast fading which variation of the received signal is so rapid and small compared with the shadowing process. This fading occurs from objects which signal reflects and scatters toward receiver. This occurrence causes several waves to arrive at the receiver via different paths, called as multipath propagation [32].

Since objects within the channel of environment are similar to dielectric properties within the channel of fruit. When signal is transmitted through the channel

of fruit, then signal will be reflected and scattered toward receiver. This characteristic is similar to fast fading process which it can be utilized to detect property of fruit. To characterize fast fading process, statistical description is used, which will be analyzed for line-of-sight and non-line-of-sight cases.

In non-line-of-sight case, signal of direct path toward receiver is blocked which receiver obtains only multipath components. This case is called the Rayleigh distribution. To analyze multipath components, the variable “ α ” is the real and imaginary of multipath components which assumes as a complex Gaussian random variable. The variable “ r ” is magnitude of multipath components.

$$\alpha(t) = x(t) + jy(t) \quad (2.10)$$

$$r = |\alpha| = \sqrt{x^2 + y^2} \quad (2.11)$$

The mean power of multipath distribution or power in random part is given by

$$\begin{aligned} \text{Total power} &= \frac{E[\alpha(t)\alpha^*(t)]}{2} = \frac{E[(x(t)+jy(t))(x(t)+jy(t))^*]}{2} \\ &= \frac{E[x^2(t)]+E[y^2(t)]}{2} = \frac{\sigma^2+\sigma^2}{2} = \sigma^2. \end{aligned} \quad (2.12)$$

This mean power is same as the mean-square value of real signal. By the standard Gaussian distribution is normal distribution with zero mean ($\bar{x} = 0$, $\bar{y} = 0$), it results in power equaled variance (σ^2), as shown in equation 2.12. In addition, probability density function (p.d.f) of NLOS channel can be characterized by

$$P_R(r) = \left(\frac{r}{\sigma^2}\right)e^{-r^2/2\sigma^2}. \quad (2.13)$$

It is noted that statistical data can assist to estimate fading amplitude for channel in NLOS situations.

In line-of-sight situation, the received signal consists of a random multipath components and line-of-sight component. The multipath components have already been described by the Rayleigh distribution. While LOS component is essentially constant power within the boundary set by path loss. The prediction of this condition will resemble method of Rayleigh distribution. The complex Gaussian variable (α) still applies for representing the multipath components. The real constant is added within system to represent the voltage of the line-of-sight. Then, characterization of this case can show in the p.d.f of the channel, which known as Rician distribution, given theoretically by

$$P_R(r) = \left(\frac{r}{\sigma^2}\right) e^{-(r^2+s^2)/2\sigma^2} I_0\left(\frac{rs}{\sigma^2}\right) \quad (2.14)$$

where s is the magnitude of the LOS component and σ^2 is variance of multipath component (power of multipath). The function I_0 is the modified Bessel function of the first kind and zeroth order. Note that Rician distribution is identical to Rayleigh formulation (2.13) when “ s ” is set to zero.

Furthermore, the p.d.f of Rician distribution can often be expressed in terms of another factor, that is to say Rician k-factor and defined by

$$k\text{-factor} = \frac{\text{Power in constant part}}{\text{Power in random part}} = \frac{s^2/2}{\sigma^2} \quad (2.15)$$

The Rician k-factor is a ratio of the power of LOS component to the power of remaining multipath. It is a measure of the severity of fading. In case of k-factor = 0 is character that corresponds to the most severe fading and same as Rayleigh distribution. On the other hand, the k-factor approaches infinity which indicates

excellent communication without multipath component. This is the reason that Rician k-factor is the key indicator to characterize wireless communication.

To utilize with fruit, the Rician k-factor can also indicate propagation channel within fruit under test. The different dielectric properties causes change of signal components. Then, signal fading is analyzed by calculating Rician k-factor and shows characteristic of the fruit.

2.4 Reflection measurement

In a reflection measurement, an electromagnetic wave propagates from one material to another which impedance of both sides are different. This results in the wave velocity change and a partial reflection of the electromagnetic wave from the interface between the two materials. To understand easily, the oblique incidence can be used for representing in reflection methods. This discussion will use the parallel polarization of electric field which incident at a dielectric interface for illustrating the theory.

To apply for a sensor system, a reflection method is used with a reflectometer. A reflectometer is a device that transmits electromagnetic wave to an object and measures the reflected wave that can reveal the material's property [21]. This method can operate in either a contact or non-contact mode. However, a sensor for continuous process requires non-contact mode which free-space technique is the main solution. In most of reflectometer, the structure composes only one probe for detection. This probe transmits signal and simultaneous receives electromagnetic wave which is shown in Fig. 2.9 (a). However, it is difficult to change the incident angle of the transmitted wave, including received angle. Fig. 2.9 (b) shows a bistatic structure for free-space reflection measurement. This structure has two antennas which use for transmitting and receiving waves, respectively. This method can measure reflection at different angles and it is benefit when requires to measure many positions.

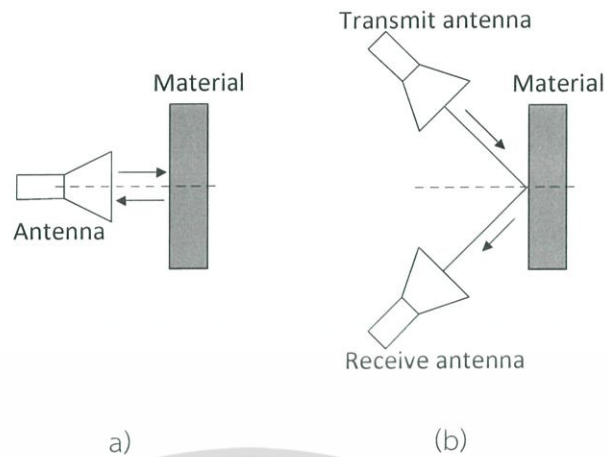


Fig. 2.9 Structure of reflectometer: (a) Monostatic reflection (b) Bistatic reflection

The appearance of orange is the spherical dielectric which the incident wave has the opportunity to reflect and to transmit into the spherical dielectric, as shown in Fig 2.10 (a). To understand easily, the reflection on a plane interface between free-space and the dielectric region can be utilized for discussion. The incident wave (\vec{E}_i) reflects at the interface and penetrates into a dielectric material, as shown in Fig 2.10 (b). As reflection and transmission, an electric field vector travels in the x-z plane with parallel polarization. The form of incident fields are given by

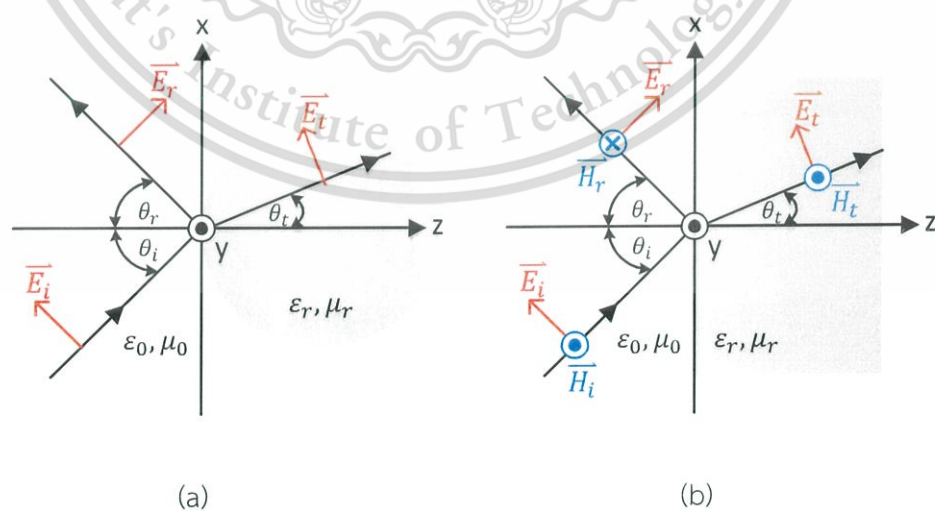


Fig. 2.10 Incident wave and reflected wave for material interface [33]: (a) Spherical dielectric (b) Plane dielectric

This material is reserved for educational use only, not allowed for commercial use.

Forbidden to modify the content, and cite the document when use.

$$\vec{E}_i = E_0(\hat{x} \cos \theta_i - \hat{z} \sin \theta_i) e^{-jk_0(x \sin \theta_i + z \cos \theta_i)}, \quad (2.16a)$$

$$\vec{H}_i = \frac{E_0}{\eta_0} \hat{y} e^{-jk_0(x \sin \theta_i + z \cos \theta_i)}, \quad (2.16b)$$

where $k_0 = \omega\sqrt{\mu_0\epsilon_0}$ and $\eta_0 = \sqrt{\mu_0/\epsilon_0}$ are the propagation constant (also known as the phase constant or wave number) and wave impedance of the free-space. E_0 is arbitrary amplitude constant. The reflected and transmitted fields can be written as

$$\vec{E}_r = E_0\Gamma(\hat{x} \cos \theta_r + \hat{z} \sin \theta_r) e^{-jk_0(x \sin \theta_r - z \cos \theta_r)}, \quad (2.17a)$$

$$\vec{H}_r = \frac{-E_0\Gamma}{\eta_0} \hat{y} e^{-jk_0(x \sin \theta_r - z \cos \theta_r)}, \quad (2.17b)$$

$$\vec{E}_t = E_0T(\hat{x} \cos \theta_t - \hat{z} \sin \theta_t) e^{-jk_1(x \sin \theta_t + z \cos \theta_t)}, \quad (2.18a)$$

$$\vec{H}_t = \frac{E_0T}{\eta_1} \hat{y} e^{-jk_1(x \sin \theta_t + z \cos \theta_t)}, \quad (2.18b)$$

where Γ and T is the reflection and transmission coefficients, $k_1 = \omega\sqrt{\mu\epsilon_1}$ is the propagation constant of the dielectric material, and $\eta_1 = \sqrt{\mu/\epsilon_1}$ is wave impedance of the dielectric material.

At the interface at $z=0$, tangential field components are obtained from the field in equation 2.16, 2.17, and 2.18 by enforcing the continuity of E_x and H_y , defined as

$$\cos \theta_i e^{-jk_0x \sin \theta_i} + \Gamma \cos \theta_r e^{-jk_0x \sin \theta_r} = T \cos \theta_t e^{-jk_1x \sin \theta_t}, \quad (2.19a)$$

$$\frac{1}{\eta_0} e^{-jk_0x \sin \theta_i} - \frac{\Gamma}{\eta_0} e^{-jk_0x \sin \theta_r} = \frac{T}{\eta_1} e^{-jk_1x \sin \theta_t}, \quad (2.19b)$$

The two sides of equations 2.19 are functions of the coordinate x , including the continuity of E_x and H_y at the interface for all x . Then, the x variation must be

the same on both sides of the equations which cause the equal phase factor as follows:

$$k_0 \sin \theta_i = k_0 \sin \theta_r = k_1 \sin \theta_t. \quad (2.20)$$

This results in the well-known Snell's laws of reflection and refraction:

$$\theta_i = \theta_r, \quad (2.21a)$$

$$k_0 \sin \theta_i = k_1 \sin \theta_t. \quad (2.21b)$$

Using equation 2.21 in equation 2.19, the reflection coefficient can be written as follows:

$$\Gamma = \frac{\eta_1 \cos \theta_t - \eta_0 \cos \theta_i}{\eta_1 \cos \theta_t + \eta_0 \cos \theta_i}. \quad (2.22)$$

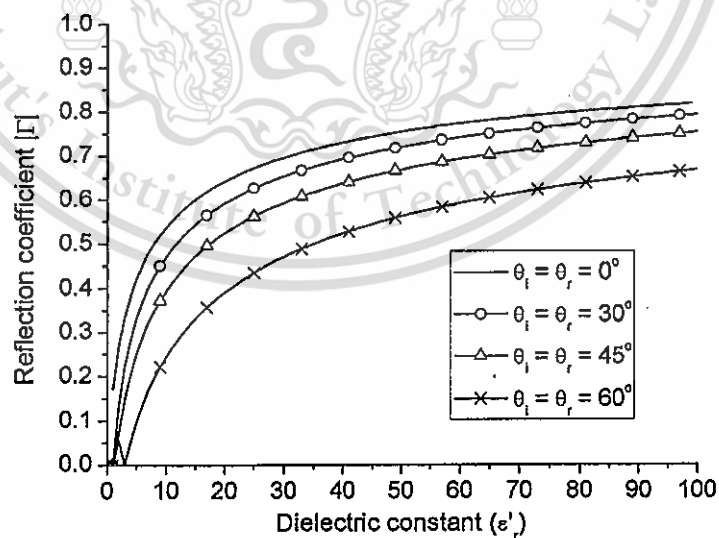


Fig. 2.11 Reflection coefficient versus dielectric constant by varying angle of incident wave.

Let us define the intrinsic impedance of free-space as $\eta_0 = \sqrt{\mu_0/\epsilon_0} \approx 377\Omega$ where $\mu_0 = 4\pi \times 10^{-7}$ henry/m, $\epsilon_0 = 8.854 \times 10^{-12}$ farad/m, and $\epsilon_r = \mu_r = 1$ for free-space. Also, the intrinsic impedance for a dielectric material can be derived in the same manner by using

$$\eta_1 = \sqrt{\mu/\epsilon_1} = \eta_0 \sqrt{\frac{\mu_r}{\epsilon_r}}. \quad (2.23)$$

The reflection coefficient can be determined from these intrinsic impedances by calculating in equation 2.22. Fig. 2.11 illustrates the relation between dielectric constant of material under test and reflection coefficient by varying angle of incident wave. It is noted that reflection coefficients are shifted to high value with decreasing angle of incident wave, meanwhile, the reflection will be increased with increasing dielectric constant. However, high dielectric constant will slightly change the reflection coefficient and the measurement will have more uncertainty.

As above mentioned, the dielectric properties influence reflected wave since those values can be used for determining impedance. If the impedance of free-space is different from that of material, there will appear the reflection of wave.

Therefore, reflection method is utilized for wave reception that reflects from fruit. The bistatic measurement of reflected waves around the fruit will be used. Then, collected data of waves are processed by statistical method, which is based on the Rician k-factor.

2.5 Scattered wave from a non-uniform dielectric

The main purpose here is the application of the previously mentioned basic principles and dielectric properties of orange. Then, the concept of the proposed sensor shows how to overcome problems for classifying quality of fruit, including simulation to design the sensor system.

Due to the different influences on scattered waves of normal and granulated fruits that have different dielectric properties, the channels of the scattered waves exhibit different values of k-factor (k). These values can be calculated from equation 2.15 where the mean of magnitude of line of sight component “s” is calculated from the magnitudes of scattered waves from different positions around the fruit and “ σ^2 ” is the variance of the scattered waves.

In order to obtain statistical data for calculating k-factor, the signal reception around the fruit is necessary. The value of k-factor can be either low or high which depends on dielectric properties of the fruit. If dielectric properties within fruit are much dissimilar, the k-factor will be low since the received signals from around the fruit are different. This causes high variance (σ^2). On the other hand, the similar dielectric properties around the fruit imply low variance of scattered wave (σ^2) and results in higher k-factor. This is the reason that k-factor can be used for indicating quality of fruit.

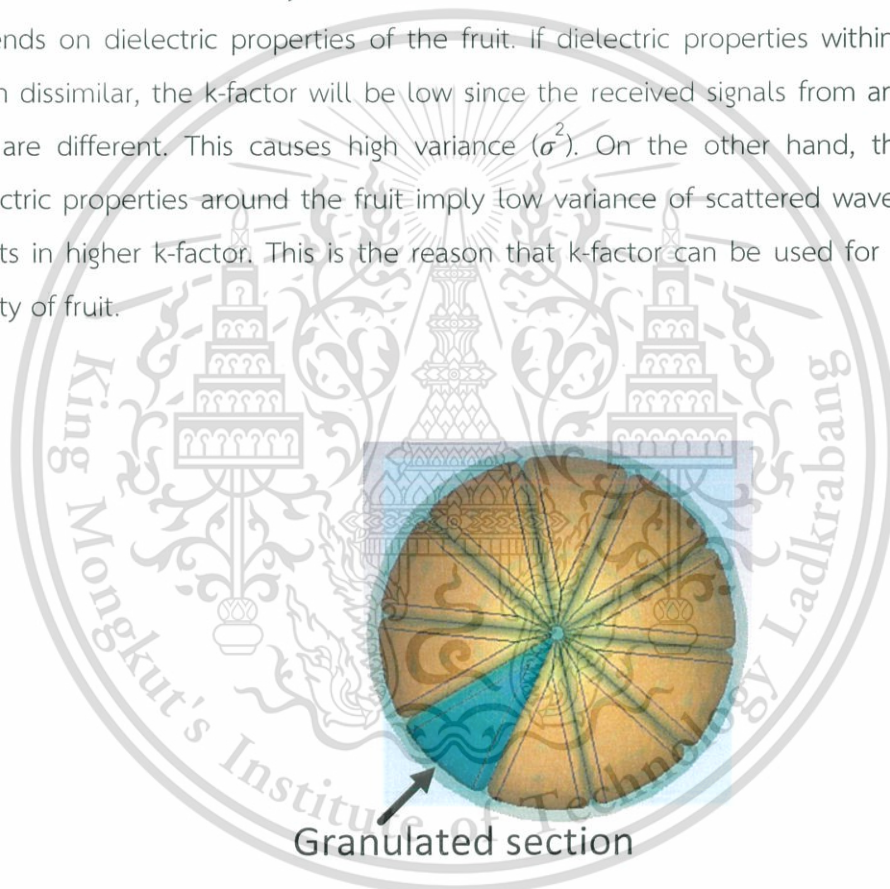


Fig. 2.12 Model of granulated tangerine

The model of granulated tangerine was used to determine the optimum number of the receiving antennas which receive scattered wave from the model. Fig. 2.12 shows the model of granulated tangerine which simulates 6 cm in size and having one granulated section out of a total of 10. The dielectric properties of the granulated flesh were set as 33.96 -j9.96 while those of the normal flesh were set as

45.23 -j12.71. The transmitting antenna illuminated 2.45 GHz incident waves on the granulated tangerine model producing scattered waves around the model ($0 < \theta < 2\pi$). Then, the scattered waves from the model travelled to the receiving antenna as shown in Fig. 2.13.

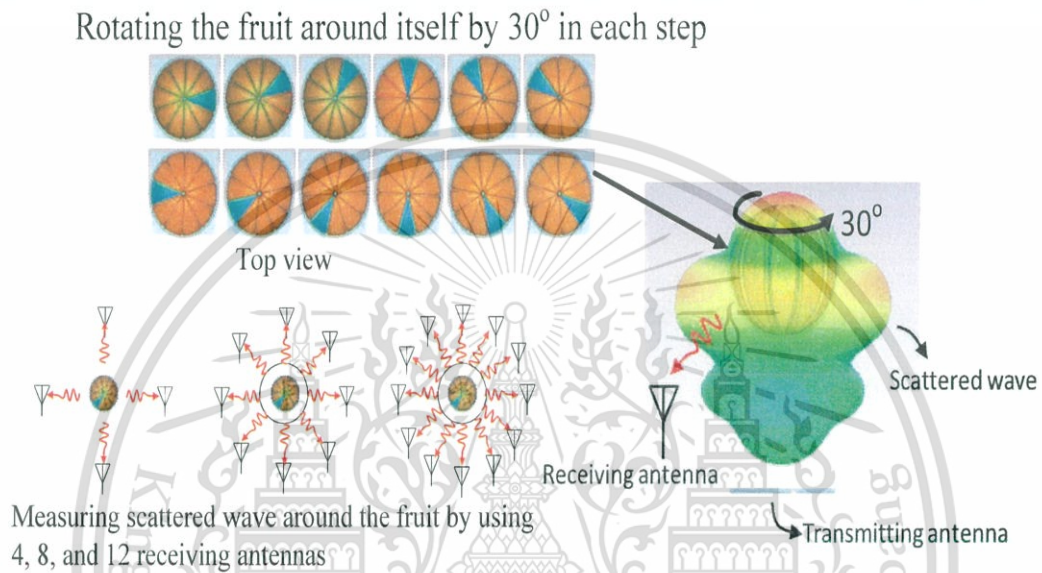


Fig. 2.13 Simulation to determine the optimum number of receiving antennas.

Table 2.2 k-factors for different number of receiving antennas

Number of the receiving antennas	4	8	12
Minimum k-factor	1.08	0.49	0.38
Average k-factor	2.04	0.99	0.88
Maximum k-factor	3.81	1.78	1.64

To simulate whether the granulated section would be detected or not, it was placed at different positions in incremental steps equivalent to rotating the fruit around itself by 30° in each step, as illustrated in Fig. 2.13. The waves scattered from the model at each position were received by 4, 8, and 12 receiving antennas, and the corresponding Rician k-factors were calculated, shown in Table 2.2. It can be observed that the more number of the receiving antennas, the lower value of k-

factor due to a higher chance that a scan by the system with more number of receiving antennas can detect the granulated section and produce a higher variance hence a lower k-factor. As the difference between the values of k-factors obtained by the system with 8 and with 12 receiving antennas was not much and since a larger number of the receiving antennas result in a more complex antenna system, we picked 8 as the optimum number of the receiving antennas for this work. This simulated result implies that we can use the beam-scanning antenna with 8 beams to replace system with 8 receiving antennas.

Hence, the calculation of k-factor can be possible to detect the granulated orange which has to receive the scattered wave from around an orange with eight directions.

2.6 Conclusion

In this chapter, characteristic of orange and principle theory have been explained for classifying fruit quality. An orange comprises many components such as rind, flesh, and seed, etc. A common disorder of orange is granulation which occurs in the part of flesh. To check inside the tangerine, operating frequency at 2.45 GHz is suitable for monitoring flesh of tangerine. The dielectric properties between normal and granulated oranges, including total soluble solids were investigated and presented. It is seen from the experimental results that the dielectric constant and loss factor of normal tangerine are significantly higher than those of granulated tangerine. The water content of granulated tangerines is less than that of normal tangerine. Also, the total soluble solids for tangerine juice indicate that normal tangerines have sweet flavor, whereas granulated tangerines are tasteless. Since juice vesicles of granulated tangerines are dry and tough, this clearly confirms that dielectric properties and flavor of normal tangerine are different from those of granulated tangerines. These properties can be indicated by propagation channel. In order to know characteristic of channel, Rician k-factor is utilized which is important factor to design wireless communication system. This factor is applied for channel of orange. The dielectric properties of orange are treated as a propagation channel that k-factor relates with dielectric properties. To evaluate k-factor, the signal reception

from a transmitter which travels through dielectric properties of orange must be executed. The reflectometer can be utilized for transmitting electromagnetic wave to an object and measuring the reflected wave that can reveal the material's property. In addition, the bistatic reflection is a suitable structure to set up in a continuous process. Both k-factor and bistatic reflection are used for a sensor system. However, k-factor is obtained from statistical data, scanning around an orange is necessary. In order to use in real scan, receiving antenna has to receive scattered wave from around an orange with 8 directions. This condition is sufficient for classifying granulated orange.



CHAPTER 3

PHASDED ARRAY USING PATTERN RECONFIGURABLE YAGI-UDA ANTENNAS

3.1 Introduction

To capture wave scattered from around the fruit, a beam-scanning antenna can be applied. The mechanism of beam-scanning is divided into two groups, i.e. mechanical rotation and electronic processing. However, mechanical scanning often suffer from wear and tear. It causes expense to repair mechanical equipment. To avoid machine, electronic scanning is selected for this application. This solution can be carried out by a phased array using pattern reconfigurable Yagi-Uda antenna. The detail of the proposed antenna will be explained, including experimental results. This chapter begins with a discussion of the pattern reconfigurable Yagi-Uda antenna and modes that provides good efficiency. Then, array antenna will be utilized and explained by arrangement of reconfigurable Yagi-Uda antennas. This configuration can be extended to beam-scanning with meaningful results.

3.2 Pattern reconfigurable Yagi-Uda antenna

The rapid technological advancement of wireless communications has significantly contributed to the development of reconfigurable antennas with speedy data transferability. As the name implies, a reconfigurable antenna is designed to enable alterations of radiation directions by which the interference is reduced and less energy is required. In addition, the reconfigurable antenna is able to achieve a larger coverage by means of re-directing the main beam toward the target and thereby minimizes the volume requirement. These characteristics make the reconfigurable antenna a good candidate for applications in short-range radio communication devices (SRDs) [34], e.g. for wireless audio and video, wireless LAN, RF (RADAR) level gauges, and sensors. Moreover, according to [35], the pattern-

reconfigurable antenna could be deployed in the multiple-input-multiple-output (MIMO) system to reduce the spatial channel correlation and maximize link capacity.

There exists four main reconfiguration mechanisms that have been employed in the reconfigurable antennas, i.e. the material change [36], physical change [37], optical change [38], and electrical change [39]-[51] mechanisms. The fourth mechanism relies upon discrete elements (e.g. RF-MEMs, PIN diodes, varactors) to redistribute the surface currents. By comparison, it is simpler to integrate switches into an antenna to achieve the intended reconfigurable functionality. Furthermore, the responsiveness of discrete elements is significantly higher than any other mechanism, a phenomenon which leads to good performance.

Previous research attempted the development of pattern-reconfigurable antennas using discrete elements. Nonetheless, most of them were focused on reconfiguration of the main beam shape, e.g. transformation between endfire and broadside radiation patterns [39]-[40], reconfiguring between conical and broadside radiations [41], altering the radiation patterns between near-omnidirectional pattern and two endfire patterns whose main beams are directed in the opposite directions [42], and switching from the boresight direction of a slot antenna to that of a monopole antenna [43].

The steering of null positions via the transformation of shape beam is another electrical change mechanism in which varactor diodes are employed for continuous null steering [44]-[45]. Another electrical change mechanism is steering of the main beam direction, which is of great interest and extensively researched [46]-[51]. In [46]-[47], a four-element L-shaped antenna array with pin diodes was utilized to manipulate the radiation beam to any direction in the azimuth plane with their respective antenna gains of 2.1 and 2.7 dBi. In [48], two couples of magnetic dipoles array were designed to change the main beam direction by phase difference between two magnetic dipoles. The phases were adjusted by four varactor diodes and the gains were in a range of 2-4 dBi.

In addition, there exists prior research on beam-steering antennas based on the Yagi-Uda antenna principle [49]-[51]. Typically, these antennas are made up of either one or several driven elements and a number of parasitic elements integrated with

switches. By alternating the status of switches (i.e. OFF/ON), the parasitic elements function as either director or reflector to regulate the main beam direction. In [49], a microstrip dipole was the driven element of the antenna and the main beam was directed to either one of three directions by manipulating the switches on the parasitic elements. In [50], a microstrip patch was used as the driven element. The circular polarization was formed by two identical reconfigurable linear Yagi-Uda patch arrays lying orthogonally to each other around a single driven patch element. The radiation pattern of the antenna by [50] was able to cover the horizontal plane by means of manipulation of the switches on the parasitic elements.

Recently, a wire antenna was implemented in a four beam-pattern reconfigurable Yagi-Uda antenna [51]. This antenna was comprised of a pair of dipoles and four parasitic elements and arranged in uniform linear array. The antenna was fed by a coaxial transmission line and capable of switching between the dipoles during operation. To achieve four beams for UHF TV signal reception, the parasitic elements were required to function in correspondence with the operating dipole.

The sensor functionality of the proposed antenna is based on [34] for a frequency range of 2.435-2.465 GHz (i.e. Table 11 of Appendix 2 to Annex 2), which 2.45 GHz frequency exists in this range. In addition, its capability of beam steering over 360° in the azimuth plane without the need of a control motor contributes to minimal units of the antenna required for installation and thus lower budgets. Therefore, the antenna design of this work is based on Yagi-Uda antenna which feeds by microstrip-to-CPS transition, and capable of re-directing the main beam toward different directions. The details of the antenna are provided in the following sections.

3.2.1 Yagi-Uda antenna

The basic structure of proposed pattern reconfigurable antenna is planar Yagi-Uda antenna that consists of a reflector, a driven element and a director. To support explanation of antenna, this will start with general Yagi-Uda antenna in the following [52].

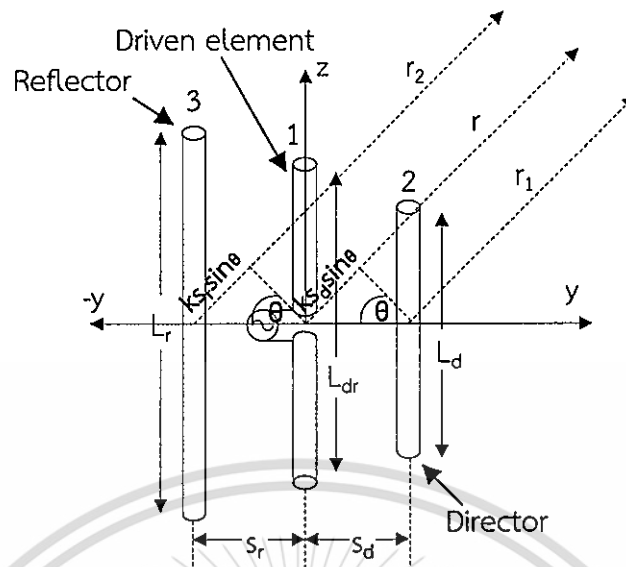


Fig. 3.1 Structure of Yagi-Uda antenna [53]

A single driven element in the form of dipole, including parasitic elements performed as a reflector or a director, are arranged in end-fire array along the y -axis, as shown in Fig. 3.1. The current is only fed on the driven element and then it will induce current to parasitic elements. The length of the driven element (usually $0.45-0.49 \lambda$) behaves as a resonance element which refers to a resistance, i.e. reactance is zero. It is well known for phasor that current of resistance and its voltage is in-phase with each other. The one of parasitic elements is set on radiated direction ($+y$ axis) that it is known as a director. Also, another parasitic element is set on the opposite side of radiation ($-y$ axis), called the reflector. The length of the reflector is longer than that of the driven element whereas the length of the director is shorter than that of the driven element. In addition, the dipole is similar to flared transmission line with open circuit, which can determine impedance of transmission line terminated an open circuit by [33]

$$z_{in} = -jz_c \cot\left(\frac{2\pi}{\lambda} L\right) \quad (3.1)$$

where z_c is characteristic impedance of transmission line and L is length of transmission line terminated with an open circuit. If the length of flared transmission line is longer than that of resonance, it will be inductive. This is reason that reflector behaves as an inductive reactance and its current lags phase of voltage. Similarly, the

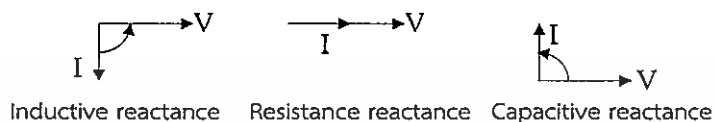


Fig. 3.2 Phasor diagram of impedance [53]

director is a capacitive reactance since the length of director is shorter than that of resonance. The current of capacitive reactance is always leading the voltage. The phasor diagram of impedance is summarized in Fig. 3.2. These appearances result in main beam in only one direction and will be discussed in the next paragraph.

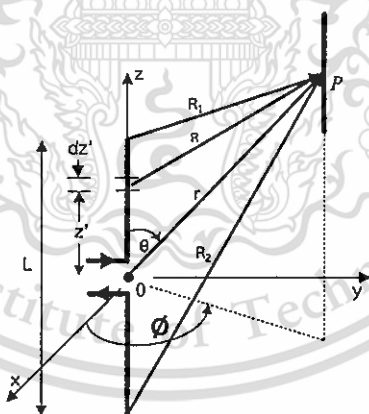


Fig. 3.3 Thin dipole for near field analysis [52]

The electric field induces from the driven element to the parasitic element which is in the form of near field. The sinusoidal current distributes on the dipole that has a negligible diameter, is shown in Fig. 3.3. The vector of current is directed and travelled along the z-axis. To determine field, it is considered with

This material is reserved for educational use only, not allowed for commercial use.

cylindrical coordinate and the symmetry in the ϕ coordinate ($\partial/\partial\phi = 0$). The vector potential (A) will be determined from current distribution and used to calculate magnetic field (\vec{H}) as

$$\begin{aligned}\vec{H} &= \frac{1}{\mu} \nabla \times \vec{A} = -\hat{a}_\phi \frac{1}{\mu} \frac{\partial A_z}{\partial \rho} \\ &= -\hat{a}_\phi \frac{I_0}{4\pi j y} \left[e^{-jkR_1} + e^{-jkR_2} - 2\cos\left(\frac{kL}{2}\right) e^{-jkr} \right]\end{aligned}\quad (3.2)$$

where $r = \sqrt{x^2 + y^2 + z^2} = \sqrt{\rho^2 + z^2}$,

$$R_1 = \sqrt{x^2 + y^2 + \left(z - \frac{L}{2}\right)^2} = \sqrt{\rho^2 + \left(z - \frac{L}{2}\right)^2},$$

$$\text{and } R_2 = \sqrt{x^2 + y^2 + \left(z + \frac{L}{2}\right)^2} = \sqrt{\rho^2 + \left(z + \frac{L}{2}\right)^2}.$$

Then, Maxwell's equation is utilized to find electric field radiated in the range of near field is

$$\vec{E} = \frac{1}{j\omega\epsilon} \nabla \times \vec{H}$$

$$E_\rho = j \frac{\eta I_0}{4\pi y} \left[\left(z - \frac{L}{2}\right) \frac{e^{-jkR_1}}{R_1} + \left(z + \frac{L}{2}\right) \frac{e^{-jkR_2}}{R_2} - 2z \cos\left(\frac{kL}{2}\right) \frac{e^{-jkr}}{r} \right]\quad (3.3)$$

$$E_z = -j \frac{\eta I_0}{4\pi} \left[\frac{e^{-jkR_1}}{R_1} + \frac{e^{-jkR_2}}{R_2} - 2\cos\left(\frac{kL}{2}\right) \frac{e^{-jkr}}{r} \right]\quad (3.4)$$

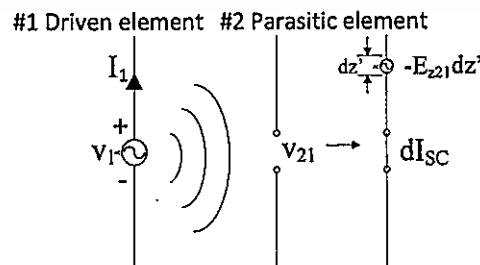


Fig. 3.4 Mutual coupling of antenna

This material is reserved for educational use only, not allowed for commercial use.

Forbidden to modify the content, and cite the document when use.

To analyze induced electric field, the parasitic element will be like a receiving antenna with open circuit. The current of driven element (I_1) induces it to parasitic element, resulting in open circuit voltage (V_{21}) at the terminals, as shown in Fig. 3.4. However, this induction occurs from region of near field which electric field is in z-axis shown in equation 3.4. If the electric field induced inside dz' of parasitic element, there will become an electromotive force. Then, open circuit of parasitic element is connected. This event causes current flow (dI_{sc}) which is produced from electromotive force. Another situation of parasitic element is assumed as a transmitter. The voltage (V_2) is fed to the center of the parasitic element, resulting in current along the wire, which is denoted by $I_2(z')$. It is noted that both situations have same impedances and comply with reciprocity theorem, given by

$$\frac{-E_{z21} dz'}{dI_{sc}} = \frac{V_2}{I_2(z')} \quad \text{or} \quad dI_{sc} = \frac{-E_{z21} dz'}{V_2} I_2(z'). \quad (3.5)$$

The total current of short circuit (I_{sc}) is contributed by all the electromotive forces induced along the parasitic element as follows:

$$I_{sc} = -\frac{1}{V_2} \int E_{z21} I_2(z') dz'. \quad (3.6)$$

Then, the induced open circuit voltage (V_{21}) is obtained from short circuit current multiplied by impedance of all effect on the parasitic element (Z_{p2}), described by

$$V_{21} = I_{sc} Z_{p2} = -\frac{1}{I_2(0)} \int E_{z21} I_2(z') dz' \quad (3.7)$$

where Z_{p2} is input impedance of all effect from the driven and parasitic elements, and $I_2(0)$ is input current of the parasitic element at terminals.

Since induced open circuit voltage has minus value, this causes transformation of voltage vector in Fig. 3.2. It is changed to opposite direction and is shown in Fig. 3.5.

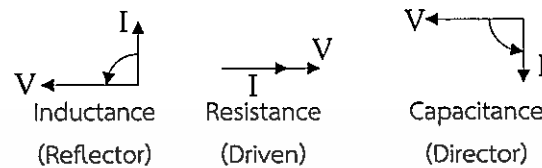


Fig. 3.5 Phasor diagram of induction between driven and parasitic elements [53]

As above mentioned, the current and voltage of the driven element is still in-phase. The phasor of reflector changes status that the current leads current of the driven element. Simultaneously, current of director lags current of the driven element. It is noted that current phases of each element are arranged in end-fire form, which maximum radiation is only one direction and directed toward lagging current, i.e. director element.

To determine radiated field, the current of each element must be known. Fig. 3.1 shows three elements of Yagi-Uda antenna. The center of the driven element is fed with voltage (V_1) and current (I_1). The parasitic elements are regarded at the center as short circuit. The voltages of parasitic element become zero, while the currents occur from near-field coupling with the driven element. The currents of director and reflector are denoted by I_2 and I_3 , respectively. The impedance matrix of network [33] is utilized, then the circuit relations are given by

$$V_1 = I_1 Z_{11} + I_2 Z_{21} + I_3 Z_{13} \quad (3.8a)$$

$$0 = I_1 Z_{21} + I_2 Z_{22} + I_3 Z_{23} \quad (3.8b)$$

$$0 = I_1 Z_{31} + I_2 Z_{23} + I_3 Z_{33} \quad (3.8c)$$

where Z_{11} , Z_{22} , and Z_{33} are impedance of driven, director, and reflector, respectively. Z_{21} is mutual impedance between the driven element and the director. Z_{31} is mutual impedance between the driven element and the reflector. Z_{23} is mutual impedance between the director and the reflector.

Then, I_2 and I_3 are obtained by solving equation 3.8

$$I_2 = I_1 \left| \frac{Z_{31}Z_{23} - Z_{21}Z_{33}}{Z_{22}Z_{33} - Z_{23}^2} \right| = I_1 F_{21} \quad (3.9)$$

$$I_3 = I_1 \left| \frac{Z_{12}Z_{23} - Z_{13}Z_{22}}{Z_{22}Z_{33} - Z_{23}^2} \right| = I_1 F_{31} \quad (3.10)$$

where F_{21} and F_{31} are current coefficient of I_2 and I_3 , respectively.

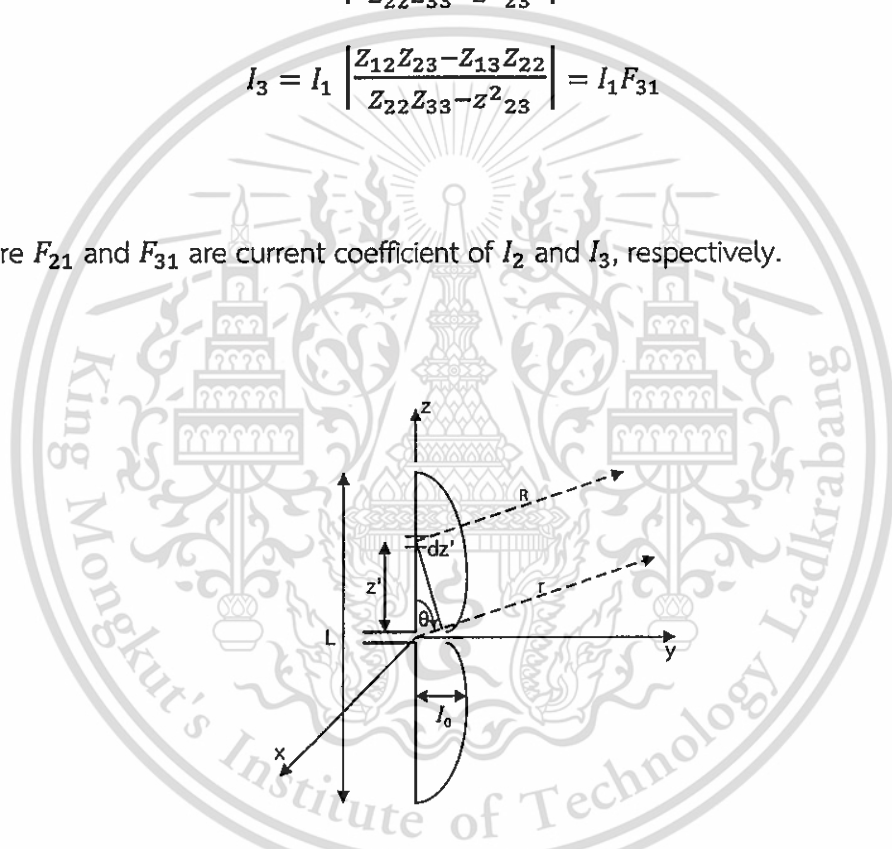


Fig. 3.6 Thin dipole for far field analysis [52]

Since Yagi-Uda antenna is a linear array antenna which the total field is determined by the vector addition of each field element within the array antenna, the far-field of linear dipole is used to determine the field vector of element. To analyze the radiation in E-plane (z-y plane), each element of the antenna will be considered as dipole antenna and described for determination of far-field.

The dipole antenna is a sum of infinitesimal dipole which is length dz' positioned along the z-axis, as shown in Fig. 3.6. The electric field in the far field of infinitesimal dipole can be written as

$$dE_{\theta} \approx j\eta \frac{kl_e(x',y',z')e^{-jk(r-z'\cos\theta)}}{4\pi r} \sin\theta dz'. \quad (3.11)$$

Then, the total electric field in the far field is obtained by summing infinitesimal dipole over length of dipole, defined as

$$E_{\theta} = \int_{-L/2}^{+L/2} dE_{\theta} = j\eta \frac{ke^{-jkr}}{4\pi r} \sin\theta \left[\int_{-L/2}^{+L/2} I_e(x',y',z')e^{jkz'\cos\theta} dz' \right]. \quad (3.12)$$

When the current is fed on the linear dipole, which distribution is given by

$$I_e(x' = 0, y' = 0, z') = \begin{cases} \hat{a}_z I_0 \sin \left[k \left(\frac{L}{2} - z' \right) \right], & 0 \leq z' \leq \frac{L}{2} \\ \hat{a}_z I_0 \sin \left[k \left(\frac{L}{2} + z' \right) \right], & -\frac{L}{2} \leq z' \leq 0 \end{cases}. \quad (3.11)$$

The electric field pattern of the dipole antenna can be written as

$$E_{\theta} = j\eta \frac{I_0 e^{-jkr}}{2\pi r} \left[\frac{\cos\left(\frac{kL}{2}\cos\theta\right) - \cos\left(\frac{kL}{2}\right)}{\sin\theta} \right]. \quad (3.12)$$

To determine radiation in E-plane, Fig. 3.1 is used to analyze, which comprises driven element, a director, and a reflector. The field vector is determined by using equation 3.12. Therefore, the total electric field of Yagi-Uda is an addition of all field vectors, given by

This material is reserved for educational use only, not allowed for commercial use.

Forbidden to modify the content, and cite the document when use.

$$\begin{aligned}
E_T(\theta) = j\eta I_1 \frac{e^{-jkr}}{2\pi r} \left\{ e^{j0} \left[\frac{\cos\left(\frac{kL_{dr}}{2}\cos\theta\right) - \cos\left(\frac{kL_{dr}}{2}\right)}{\sin\theta} \right] + F_{21} e^{j(ks_d\sin\theta + \phi_d)} \left[\frac{\cos\left(\frac{kL_d}{2}\cos\theta\right) - \cos\left(\frac{kL_d}{2}\right)}{\sin\theta} \right] \right. \\
\left. + F_{31} e^{-j(ks_r\sin\theta - \phi_r)} \left[\frac{\cos\left(\frac{kL_r}{2}\cos\theta\right) - \cos\left(\frac{kL_r}{2}\right)}{\sin\theta} \right] \right\} \quad (3.13)
\end{aligned}$$

where ϕ_d and ϕ_r are current phase of director and reflector, respectively. L_{dr} , L_d , and L_r are length of driven, director element, and reflector, respectively.

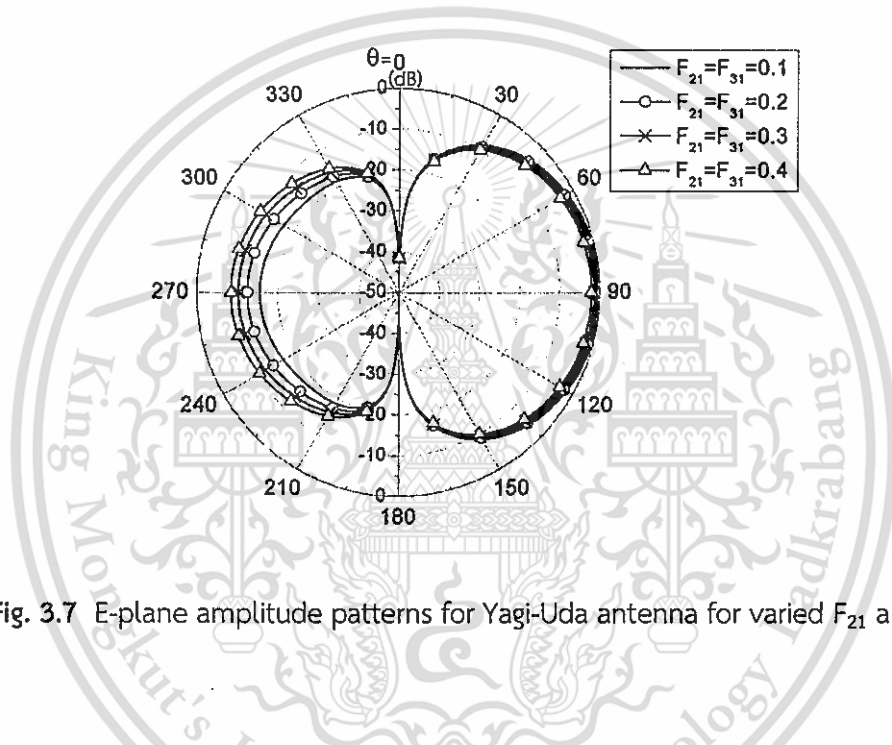


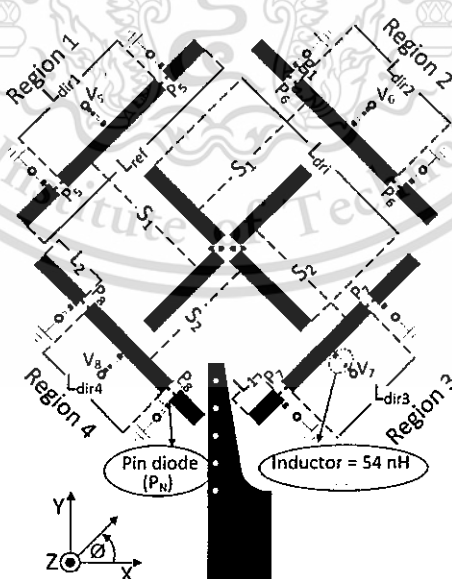
Fig. 3.7 E-plane amplitude patterns for Yagi-Uda antenna for varied F_{21} and F_{31}

From equation 3.13, the length of each element, space between elements, and current coefficient are variable which can change radiation pattern of the antenna. For example, the E-plane patterns of Yagi-Uda antenna in case of current coefficient variation are shown in Fig. 3.7. It is noted that current coefficient influences amplitude of electric field. In addition, the current coefficient is relation of self-impedance and mutual impedance of elements, which these impedances depend on dimension and space between elements. Therefore, the tuning of these parameters can produce best performance of the antenna, such as gain, side lobe level (SLL), etc.

As above mentioned, the Yagi-Uda antenna can radiate main beam in one direction. In order to utilize this process, an antenna is developed to increase direction of main beam which can direct toward more targets. The main beam direction depends on current vector of each element. To succeed re-direct main beam, electrical mechanism is applied to change current vector, including structure of antenna suitable for this application. These details will be clarified by applying this basic and described in the next section.

3.2.2 Configuration of the pattern reconfigurable Yagi-Uda antenna

The electrical mechanism with PIN diodes can be applied to Yagi-Uda antenna to achieve beam switching. In addition, antenna needs balun at the feed system which supports currents on the two arms of dipole of driven element to be the same phase and to eliminate deformed radiation pattern. The proposed antenna consists of two parts: 1) a printed Yagi-Uda antenna with PIN diodes attached onto parasitic elements (Fig. 3.8(a)), the driven elements (Fig. 3.8(b)); and 2) a microstrip-to-CPS transition for balanced current distribution (Fig. 3.8(c)).



(a)

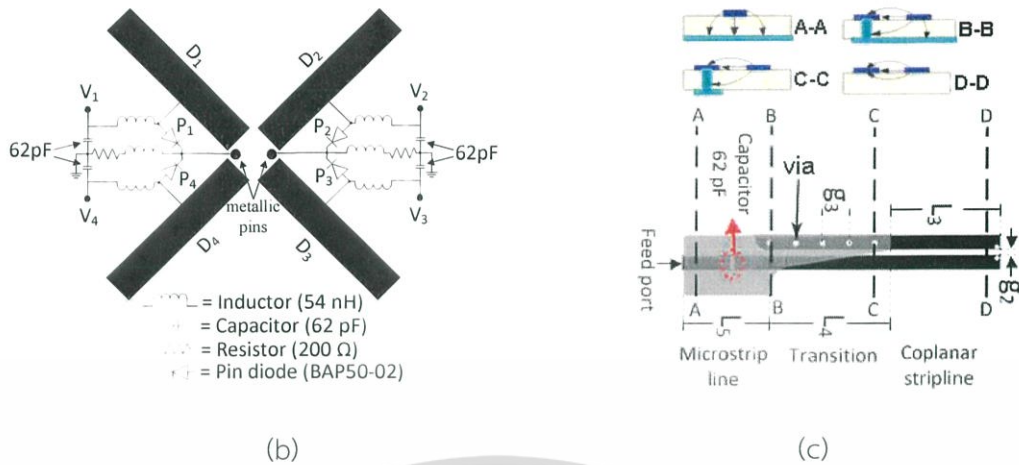


Fig. 3.8 Proposed antenna: (a) schematic of pattern-reconfigurable Yagi-Uda antenna, (b) driven elements and PIN diode circuit, (c) microstrip-to-CPS transition (balun).

A 1.6-mm-thick double-sided metallized FR-4 PCB is used as the substrate. The dielectric constant (ϵ_r) is 4.24 and loss tangent is 0.012. The top metallization consists of two driven elements, four parasitic elements and a ground plane for microstrip-to-CPS transition. The bottom metallization consists of microstrip line, transition and coplanar stripline (CPS). DC biasing cables are connected to the bottom of the antenna at V_N , where $N = 1, 2, 3, \dots, 8$. The operating frequency of the antenna is 2.45 GHz.

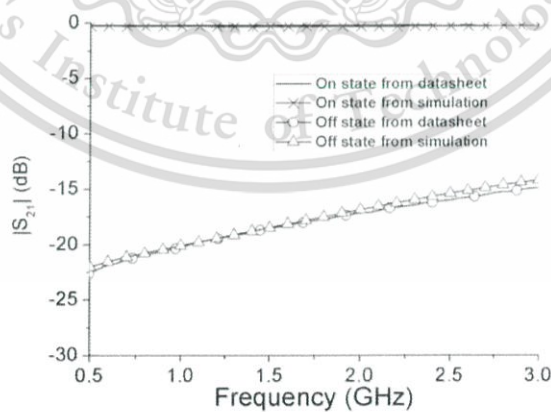


Fig. 3.9 Characteristics of the Philips BAP50-02.

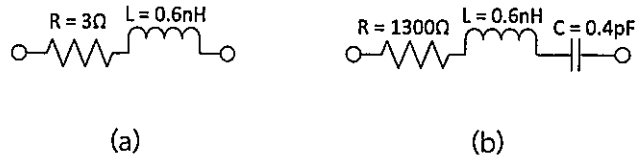


Fig. 3.10 PIN diode equivalent circuit (a) the ON state, (b) the OFF state.

The pattern reconfigurable antenna is realized by mounting four PIN diodes (BAP50-02) onto the driven elements and two PIN diodes (P_N) onto each of the four parasitic elements, resulting in a total of 12 P_N deployed on the antenna. The ON state and OFF state of diode models are established by referring to characteristics of the BAP50-02 diode for the case of 10 mA biased and the zero biased, respectively. The RLC circuits exhibit the equivalent circuit of the BAP50-02 diode. In Fig. 3.9, the simulated results of PIN diode models agree well with the datasheet of the BAP50-02 PIN diode. In the ON state, the diode is modeled as a 3Ω resistor and a 0.6nH series inductor. In the OFF state, it is modeled as series circuit consisting of a 1300Ω resistor, a 0.6nH inductor and a 0.4pF capacitor. Both models are shown in Fig. 3.10 and simulated in this work. DC-biasing voltages are utilized to manipulate the diodes on both the driven elements and the parasitic elements at V_N , where $N = 1, 2, 3, \dots, 8$. The direct current (DC) circuit is isolated from the RF signal by low-pass filters. The simulated result of low-pass filter is shown in Fig. 3.11. It can isolate between DC line and 2.45 GHz frequency with more than 20 dB , which consists of a surface-mount inductor (54 nH) and a capacitor (62 pF). The DC ground and RF signal are isolated by an inductor (54 nH).

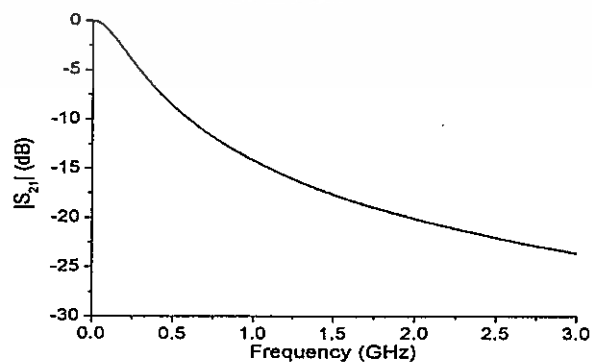


Fig. 3.11 Simulated result of isolation between DC circuit and RF signal.

This material is reserved for educational use only, not allowed for commercial use.

Forbidden to modify the content, and cite the document when use.

With reference to Fig. 3.8(b), four diodes (P_1 - P_4) are mounted orthogonally on the two driven elements. The diodes are deployed for connecting the monopoles (i.e. D_1 , D_2 , D_3 and D_4) with or disconnecting from CPS through alteration of the diode status between ON and OFF. The diode anodes are soldered to the monopoles and DC biasing voltage points. On the other hand, the diode cathodes are connected to ground and CPS through metallic pins. The selected pair of monopoles for the driven elements are perpendicular to the radiation direction. To manipulate the functions of the parasitic elements (i.e. director/reflector), each parasitic element is embedded with two diodes to regulate their electrical lengths. When V_N ($N = 5, 6, 7, 8$) is turned on, the parasitic element act as a reflector as DC voltage is fed to the anodes of two diodes (i.e. the ON state). Conversely, the parasitic element becomes a director when the DC voltage is turned off (i.e. OFF state). The functionality of the PIN diodes in the proposed antenna is discussed in Section 3.2.3.

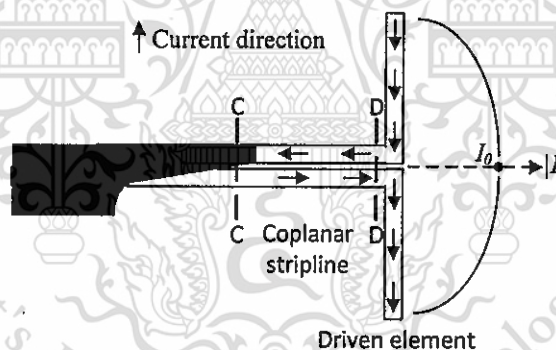


Fig. 3.12 Current distribution on CPS and driven element.

In Fig. 3.8(c), a microstrip-to-CPS transition [54] is used to feed the proposed antenna. It is constructed by a one of striplines connecting to the ground plane with five via holes. The diameter and center-to-center distance (g_3) is 1 mm and 5.1 mm, respectively. This transition realizes both field matching and impedance matching. Since the electric field lines in the microstrip line (A-A) are perpendicularly terminated at the ground of the substrate, the odd mode in the CPS is needed. As signal passes through the transition, the electric field lines have the coupling

between microstrip line and ground plane, as displayed accordingly in cross-sectional view of B-B and C-C. After ground plane is removed, the odd mode field is then established across the CPS line (D-D). This mode causes opposite direction of current (Out of phase) on CPS line, resulting in nonradiating at CPS line. In addition, the currents with the odd mode are fed on driven element which causes same direction of current on both arms, as shown in Fig. 3.12. Thus the fields radiated by the two arms of the dipole will primarily reinforce each other toward aspiring direction. Also, the impedance matching between the microstrip line and the CPS line is realized using the Klopfenstein taper, which is optimized for a given taper length [33]. A back-to-back configuration of the microstrip-to-CPS transition was simulated and optimized, as shown in Fig. 3.13. In addition, the figure illustrates the simulation results, in which $|S_{11}|$ is < -13.8 dB and the insertion loss is < 0.5 dB, which are obtained over the frequency range of 2.35-2.55 GHz.

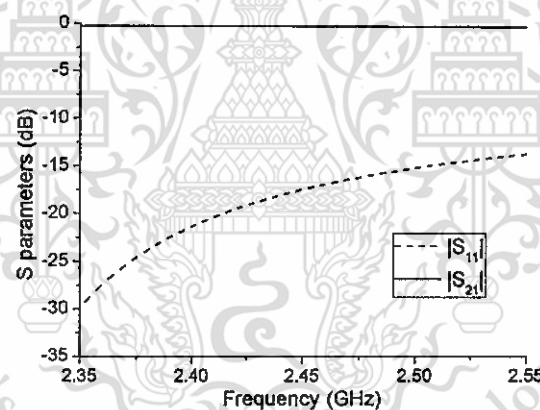


Fig. 3.13 Simulation results of the two-port back-to-back configuration of the microstrip-to-CPS transition.

A major design challenge of this research is to develop an antenna integrating balun and feed that is capable of redirecting the main beam toward a specified direction around the azimuth plane. To determine the optimal antenna design, the antenna specifications are varied until the desired performances, i.e. impedance, gains, and sidelobe level, are achieved. The impedance of the antenna is

enhanced by varying the function (i.e. director/reflector) of the parasitic elements via alternating the biasing voltages (i.e. 0 or 5 volts), including dimension of the antenna.

3.2.3 Pattern reconfigurable antenna design

The design of the pattern reconfigurable antenna is required to meet two specific criteria: (1) to be operable in the frequency range of 2.435-2.465 GHz, which is based on ISM bands for SRDs [34]; and (2) to realize a quad-directional beam-switchable antenna. In addition, the proposed antenna is not just used in conjunction with array antenna but it can be applied for other applications. Especially, the specific application is a reflectometer. With multiple beams, the reflectometer can sense multiple targets. Furthermore, a calibration with known target is required. Instead of placing a known target, i.e., a conducting plate in front of the target under test, the conducting plate is placed in the different main beam directions. This can facilitate the calibration in practice. The reflectometer consists of a transmitter, a directional coupler, an antenna, and a power detector. For illustration, with the transmitter power of 10 dBm, the freespace loss of 25 dB, directional coupler with coupling coefficient of 15 dB, a power detector with sensitivity of -60 dBm, power reflection coefficient derived from dielectric constant of paper sheet ($\epsilon_p = 3$) is -11 dB and the satisfactory gain of antenna is $(-60-10+25+11+25+15)/2 = 3$ dBi. This determination will also be used for antenna design with gains higher than 3 dBi. The initial antenna dimensions are based on the analysis given in [52] prior to subsequent optimization by trial and error to find the optimal antenna design with the best outcomes.

3.2.3.1 Main beam in region 1 (the 135°-direction main beam)

The simulation started with the main beam in region 1, as shown in Fig. 3.8(a), in which the antenna specifications are as follows: $\lambda = 122.45$ mm, $L_{dri} = 0.35 \lambda$, $L_{ref} = 0.38 \lambda$, S_1 and $S_2 = 0.21 \lambda$, and L_{dir1} , L_{dir2} , L_{dir3} , $L_{dir4} = 0.21 \lambda$. In Table 3.1, the suitable performance is achieved in Case 3 following the alternating of the status of PIN diodes (i.e. ON/OFF) in the parasitic elements. The compromise between half

power beamwidth (HPBW) of 76° , gain of 5.0 dBi and sidelobe level (SLL : $P_{sidelobe}(\text{dB}) - P_{mainlobe}(\text{dB})$) of -10.8 dB at $\phi = 18^\circ$ are achieved as shown in Fig. 3.14.

Table 3.1 Mode of PIN diodes (ON/OFF) on the parasitic elements for the 135° -direction main beam (region 1).

Case	Bias		Gain (dBi)	SLL (dB)	HPBW
	5 Volts (ON)	0 Volt (OFF)			
1	V_2, V_4, V_6, V_7, V_8	V_1, V_3, V_5	5.2	-7.1	67°
2	V_2, V_4, V_7	V_1, V_3, V_5, V_6, V_8	5.0	-10.9	70°
3	V_2, V_4, V_7, V_8	V_1, V_3, V_5, V_6	5.0	-10.8	76°
4	V_2, V_4, V_6, V_7	V_1, V_3, V_5, V_8	5.0	-5.3	61°

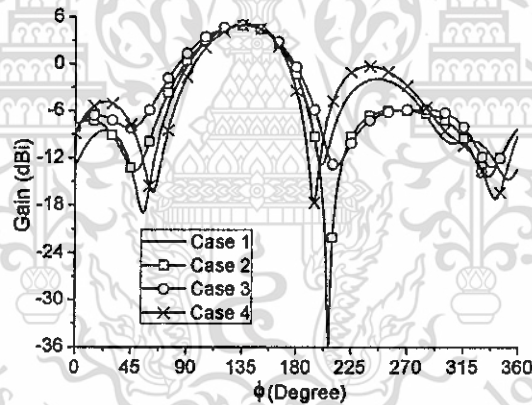


Fig. 3.14 Simulation results of radiation patterns (E-plane) in each cases of Table 3.1.

Next, the distance between the parasitic and driven elements (S_1 and S_2) was varied, while the other antenna specifications remain unaltered and the biasing voltages of PIN diodes followed Case 3 of Table 3.1. In Fig. 3.15(a), it is found that gains are inversely correlated to S_1 and S_2 , while the sidelobe level is positively correlated with S_1 and S_2 . In addition, in Fig. 3.15(b), the resonance frequency is shifted to high frequency with increases in S_1 and S_2 . Thus, the distance between the parasitic and driven elements of 0.21λ produces the best results. Then, the lengths

of directors (L_{dir1} , L_{dir2} , L_{dir3} , L_{dir4}) were varied. It is found that the gains and SLL are inversely correlated with the director length, whereas $|S_{11}|$ is positively related to the length of directors. In Fig. 3.16, the director length of 0.21λ provides the optimal gain and SLL.

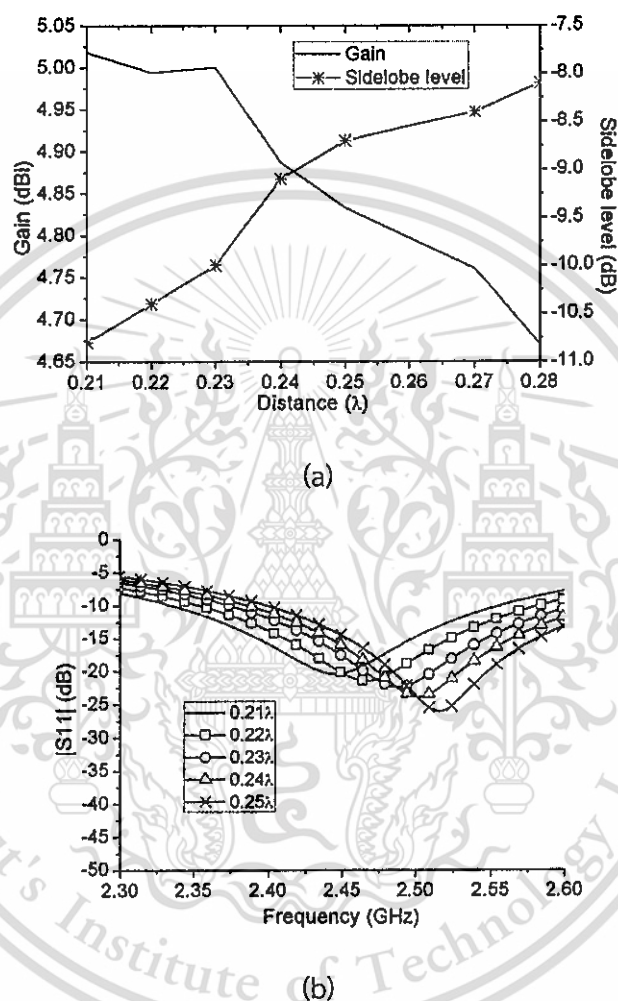
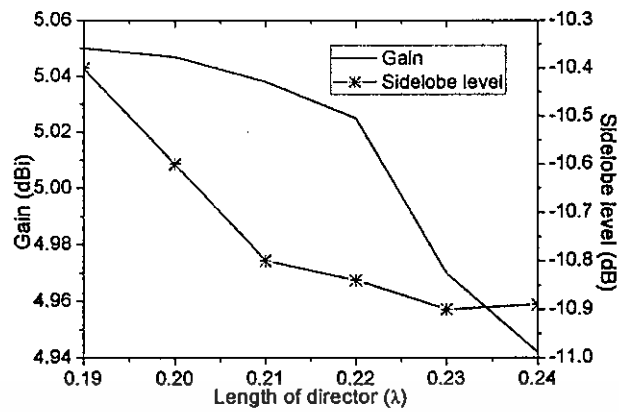
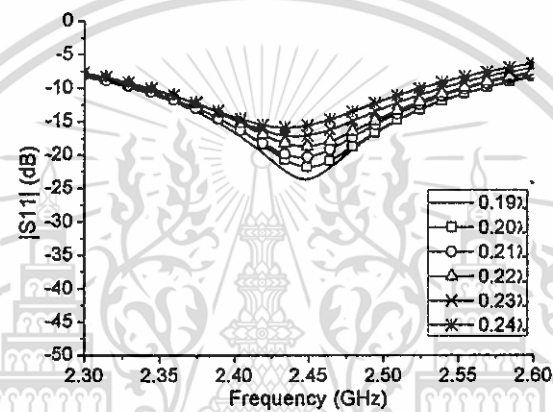


Fig. 3.15 Simulation results in case of distance variation (S_1 and S_2) for the main beam in region 1: (a) gain and sidelobe level relative to distance, (b) $|S_{11}|$ and frequency relative to distance.



(a)



(b)

Fig. 3.16 Simulation results in case of director length variation (L_{dir1} , L_{dir2} , L_{dir3} , L_{dir4}) for the main beam in region 1: (a) gain and sidelobe level relative to length, (b) $|S_{11}|$ and frequency relative to length.

3.2.3.2 Main beam in region 2 (the 45° -direction main beam)

Further simulation was carried out for the main beam in region 2 by which the antenna specifications and biasing voltages on the parasitic elements remain identical to those for the region 1 simulation, except for the biasing voltages at the driven elements. The simulated $|S_{11}|$ for incident 1 is shown in Fig. 3.17. The biasing voltages at V_1 , V_3 , V_7 and V_8 are 5 volts. Those at V_2 , V_4 , V_5 and V_6 are 0 volts. The frequency is shifted to high frequency and the gain is 4.8 dBi. Nevertheless, it is possible to improve the frequency response by altering the functions of the parasitic elements. To follow incident 2 in Fig. 3.17, the parasitic elements in regions

1, 3 and 4 are assigned to function as the reflector (V_5 , V_7 , and $V_8 = 5$ volt) while the remaining parasitic element (i.e. in region 2, $V_6 = 0$ volt) acts as a director. The frequency with lowest $|S_{11}|$ is subsequently shifted closer to the desired frequency with an improvement in gain to 5 dBi. Therefore, the functions of the parasitic elements by Incident 2 in Fig. 3.17 are good option for main beam in region 2.

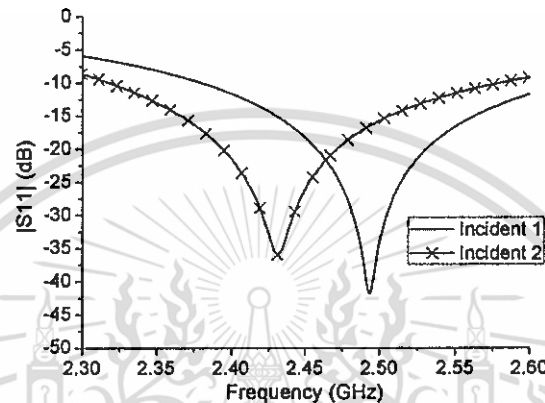


Fig. 3.17 Simulated $|S_{11}|$ for the main beam in region 2: Incident 1 is when the biasing voltages at V_1 , V_3 , V_7 , V_8 and at V_2 , V_4 , V_5 , V_6 are 5 and 0 volts respectively; Incident 2 is when the parasitic elements functions are manipulated with the biasing voltage at V_1 , V_3 , V_5 , V_7 , V_8 and at V_2 , V_4 , V_6 are 5 and 0 volts, respectively.

3.2.3.3 Main beam in regions 3 and 4 (the 310° and 225° -direction main beams)

Simulation was also carried out for the main beams in regions 3 and 4, and similar results were obtained for both regions. Thus, only the simulation results for region 4 are illustrated. In the simulations, the specifications are identical to the optimized specifications employed for region 2. In Table 3.2, Event 4 provides almost widest half power beamwidth (60.3°), the highest gain (4.7 dBi) and low sidelobe level (-7 dB). Hence, it was selected. Fig. 3.18 illustrates the simulated $|S_{11}|$ for regions 3 and 4, in which the frequency with lowest $|S_{11}|$ is shifted toward low frequency. Since it is possible to improve the impedance by varying the distance between the parasitic and driven elements (i.e. S_1), additional simulations in which S_1 was varied while the other parameters remained constant (i.e. $L_{dri} = 0.35\lambda$, $L_{ref} = 0.38\lambda$, $S_2 =$

0.21λ , L_{dir1} , L_{dir2} , L_{dir3} , $L_{dir4} = 0.21\lambda$) were performed. In Fig. 3.19, with increasing in the distance (S_1), the gain increases while the sidelobe level decreases until arriving at 0.24λ . Thus, the optimal distance (S_1) is 0.24λ .

Table 3.2 Mode of PIN diodes (ON/OFF) on the parasitic elements for the 225° -direction main beam (region 4).

Event	Bias		Gain (dBi)	SLL (dB)	HPBW
	5 Volts (ON)	0 Volt (OFF)			
1	V_1, V_3, V_5, V_6	V_2, V_4, V_7, V_8	3.4	-2.9	54.1°
2	V_1, V_3, V_5, V_6, V_7	V_2, V_4, V_8	4.1	-7.1	55.7°
3	V_1, V_3, V_6	V_2, V_4, V_5, V_7, V_8	3.8	-2.7	60.5°
4	V_1, V_3, V_6, V_7	V_2, V_4, V_5, V_8	4.7	-7	60.3°

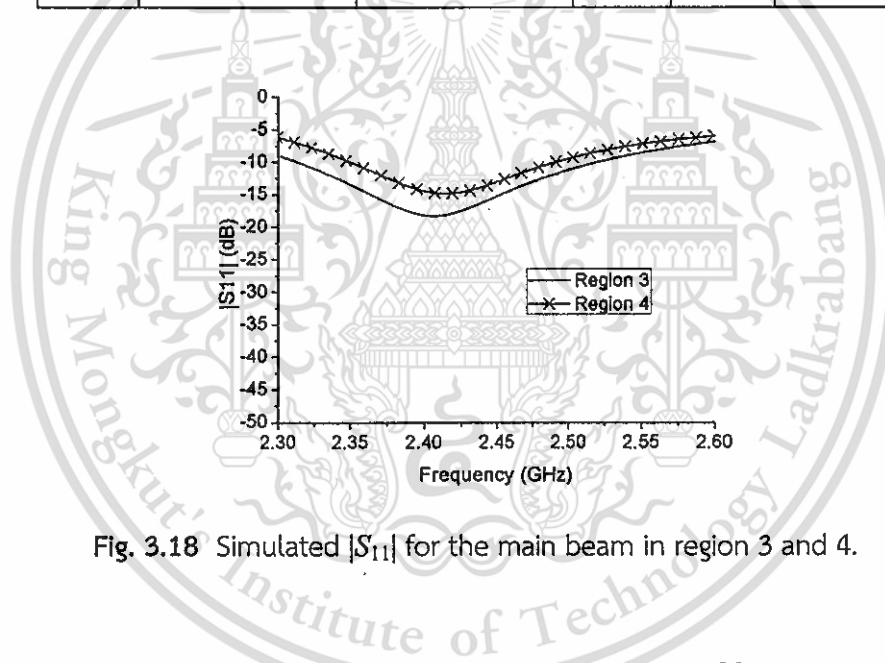
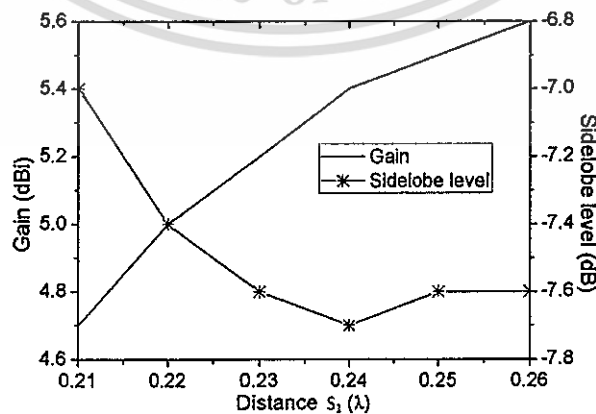
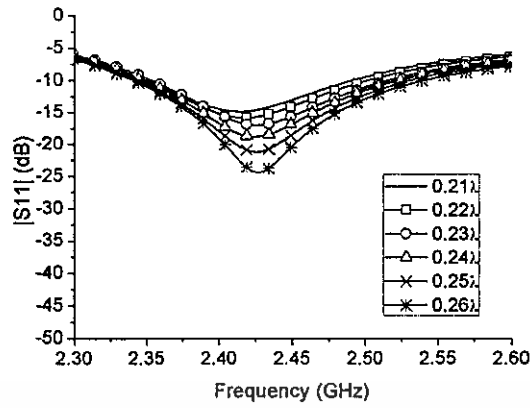


Fig. 3.18 Simulated $|S_{11}|$ for the main beam in region 3 and 4.



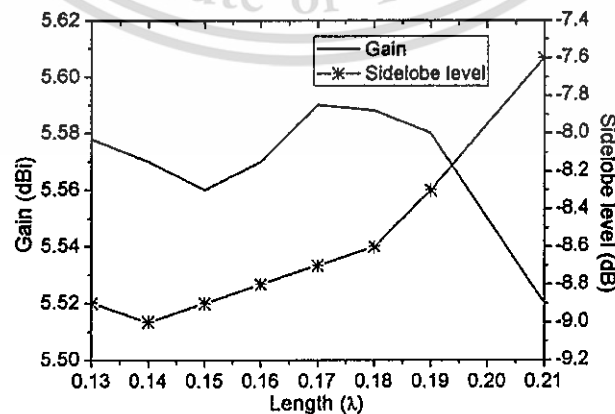
(a)



(b)

Fig. 3.19 Simulation results in case of distance variation (S_1) for the main beam in region 4: (a) gain and sidelobe level relative to distance, (b) $|S_{11}|$ and frequency relative to distance.

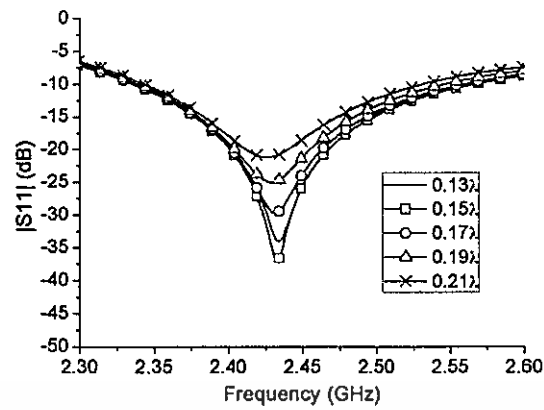
Figs. 3.20(a)-(b) illustrate the simulation results for varying director lengths (L_{dir3} and L_{dir4}), in which the highest gain is achieved at a length of 0.17λ ; however, beyond that the gain becomes lower whereas the sidelobe level and $|S_{11}|$ increase. As illustrated in Fig. 3.21, it is found that the variation in the lengths of L_{dir3} and L_{dir4} impacts the radiation performance of the main beam in region 2. As the lengths of L_{dir3} and L_{dir4} increase, the gain of the main beam in region 2 increases while the sidelobe level decreases. Thus, the director length of 0.17λ is selected for both L_{dir3} and L_{dir4} .



(a)

This material is reserved for educational use only, not allowed for commercial use.

Forbidden to modify the content, and cite the document when use.



(b)

Fig. 3.20 Simulation results in case of director length variation (L_{dir3} and L_{dir4}) for the main beam in region 4: (a) gain and sidelobe level relative to length, (b) $|S_{11}|$ and frequency relative to length.

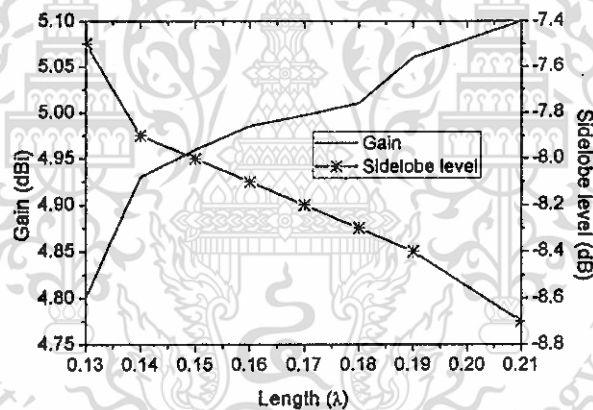


Fig. 3.21 Simulated effects of varying director lengths (L_{dir3} and L_{dir4}) on the main beam in region 2.

Therefore, the design of the prototype antenna are based on the optimal simulation results. The specific interest is the antenna ability is to achieve the highest performance with unequal measurements of its constituents. In addition, the length and spacing of the antenna constituents are varied until the target performances are achieved. The final design and biasing voltages for antenna operation are summarized in Tables 3.3 and 3.4, respectively.

Table 3.3 Optimal specifications/dimensions of the prototype antenna.

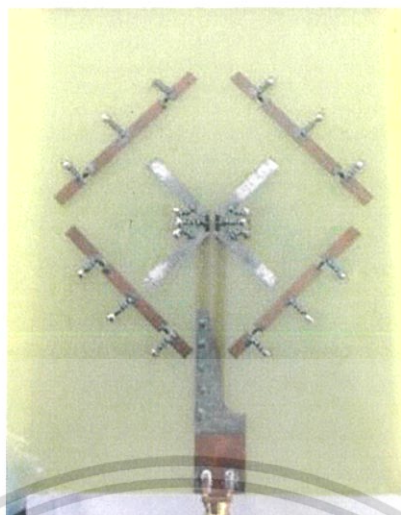
Specifics	Dimension (mm)
Length of driven element (L_{dri})	43.25 (= 0.35λ)
Length of director in regions 1 and 2 (L_{dir1} and L_{dir2})	25.7 (= 0.21λ)
Length of director in regions 3 and 4 (L_{dir3} and L_{dir4})	20.82 (= 0.17λ)
Length of reflector (L_{ref})	46.53 (= 0.38λ)
Length of L_1	6.59
Length of L_2	10.86
Spacing within parasitic element (g_1)	2
Length of CPS (L_3)	22.02
Transition length (L_4)	23.66
Microstrip line length (L_5)	17.19
Gap between strips (g_2)	1
Distance between metallic PIN on transition (g_3)	5.1
Distance between the parasitic and driven elements (S_1)	30.6 (= 0.25λ)
Distance between the parasitic and driven elements (S_2)	26 (= 0.21λ)

Table 3.4 Status of PIN diodes by region of the main beam.

Main beam	Bias	
	5 volts (ON)	0 volts (OFF)
Region 1	V_2, V_4, V_7, V_8	V_1, V_3, V_5, V_6
Region 2	V_1, V_3, V_5, V_7, V_8	V_2, V_4, V_6
Region 3	V_2, V_4, V_5, V_8	V_1, V_3, V_6, V_7
Region 4	V_1, V_3, V_6, V_7	V_2, V_4, V_5, V_8

3.2.4 Simulation and measured results

Based on the optimal simulation results tabulated in Table 3.3, a prototype antenna was fabricated for further experiment and comparison. Fig. 3.22 is a photograph of the prototype antenna onto which PIN diodes are attached using electrically conductive silver epoxy.



(a)



(b)

Fig. 3.22 Photographs of the prototype antenna (a) Top view. (b) Side view.

Figs. 3.23-3.24 respectively illustrate the simulated and measured $|S_{11}|$ relative to frequency of the main beams for the four regions of the antenna. In Fig. 3.23, the simulated $|S_{11}|$ where the impedance bandwidth is ≤ -10 dB for all four regions is between 2.34-2.56 GHz (8.98%). By comparison, in Fig. 3.24 the measured results of $|S_{11}|$ where the impedance bandwidth is ≤ -10 dB are from 2.39 to 2.59 GHz (8.2%), indicating reasonably good agreement between the simulation and measured results. Nonetheless, there is ripple in the measured $|S_{11}|$ of regions 2 and 4, while there is only one frequency with lowest $|S_{11}|$ and smooth response for the simulated results. The discrepancy is attributable to the multiple reflection from the antenna structure.

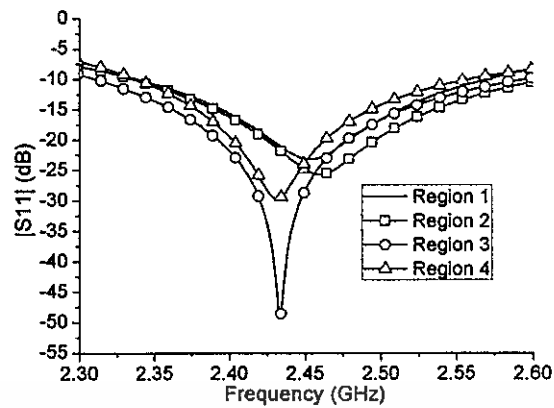


Fig. 3.23 Simulated $|S_{11}|$ for the main beams in different regions.

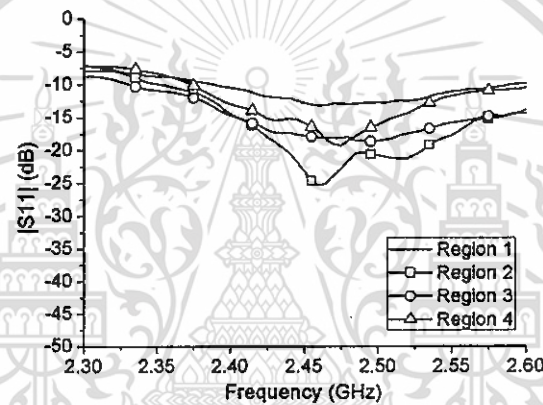


Fig. 3.24 Measured $|S_{11}|$ for the main beams in different regions.

The orientation of rectangular coordinate system for all radiation patterns is identical to Fig. 3.8(a). Fig. 3.25(a) illustrates the simulated E-plane radiation patterns for the four regions at 2.45 GHz, in which the simulated main beams are steered to the desired directions. At 2.45 GHz, the simulated maxima of the main beams in regions 1, 2, 3 and 4 are at 133° , 43° , 311° and 229° , respectively, while the simulated gains are 5.2, 5.0, 5.6 and 5.6 dBi for the corresponding regions. The simulated HPBW of each radiation pattern in regions 1, 2, 3 and 4 are 74° , 72° , 63° and 60° , respectively. Note that HPBW of regions 3 and 4 are narrower than that of the other regions due to effect of asymmetrical ground plane of microstrip-to-CPS transition. The simulated sidelobe level is approximately -8.7 dB. Fig. 3.25(b)

illustrates the simulated H-plane results. It is seen that the maximum beam directions are at 90° .

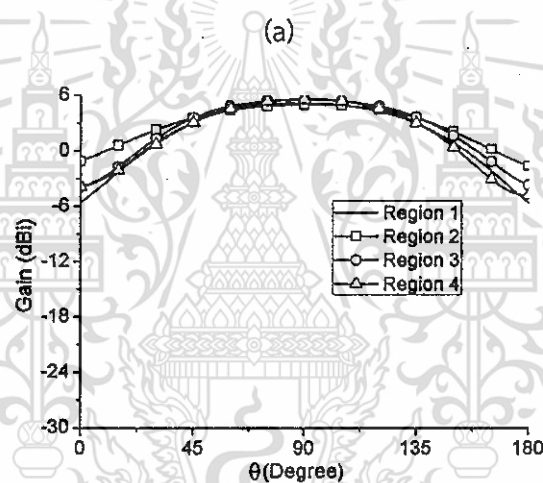
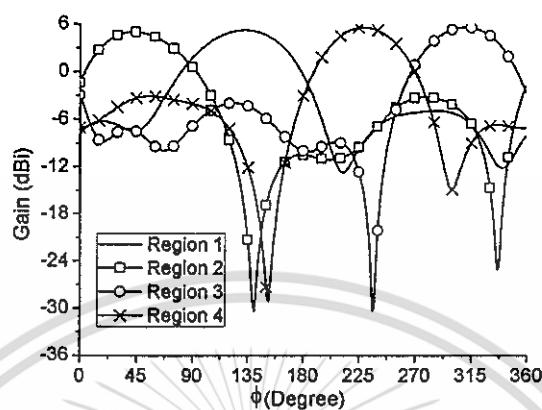
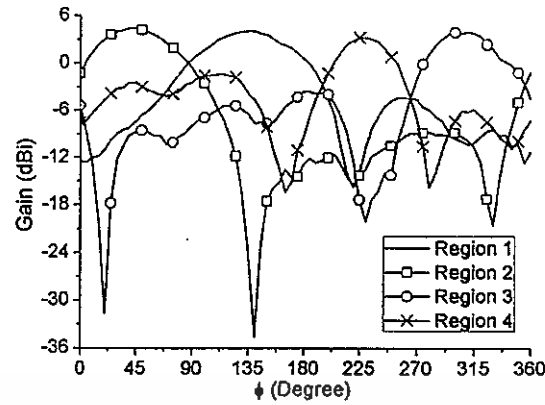
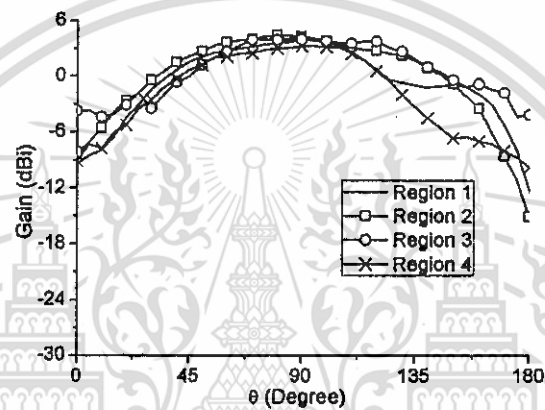


Fig. 3.25 Simulated results of radiation patterns at 2.45 GHz: (a) E-plane, (b) H-plane.

The radiation patterns of the prototype antenna were measured at the frequency of 2.45 GHz. The distance between the transmitting antenna and the prototype antenna was based on the far field distance requirement [52]. The DC power supplies were placed inside an anechoic chamber and covered with absorbers during measurement. A 360° scan was conducted during the measurement of E-plane (x-y plane).



(a)



(b)

Fig. 3.26 Measured results of radiation patterns at 2.45 GHz: (a) E-plane, (b) H-plane

The measured radiation patterns at 2.45 GHz for four different regions are illustrated in Fig. 3.26. By comparison, the measured E-plane results in Fig. 3.26(a) agree reasonably well with the simulated E-plane results in Fig. 3.25(a). The measured main beams were steered to the desired directions. The measured maxima for the main beams in regions 1, 2, 3 and 4 are at 135° , 45° , 310° and 225° , respectively, while the measured gains for the corresponding regions are 4.01, 4.42, 3.98 and 3.25 dBi. The measured HPBW of each radiation patterns in regions 1, 2, 3 and 4 are 70° , 67° , 50° and 48° , respectively. It should be noted that main beam direction in region 3 is 310° instead of 315° due to asymmetrical shape of feeding structure. In addition, the disparities between the measured and simulated gains are attributable to variations between the realized insertion loss of PIN diodes and the

ideal insertion loss on the datasheet. The measured insertion loss of PIN diode at 2.45 GHz was 0.9 dB, while in the simulation the insertion loss was modeled as 0.26 dB. It is also observed that the measured HPBW in regions 3 and 4 are narrower than the other regions, which is consistent with the simulated results. Nevertheless, the measured HPBW is narrower than simulation due to a coaxial cable and a connector are not taken into account in simulation. Fig. 3.26(b) illustrates the measured H-plane results, indicating that all main beams are in the direction of 90° .

Therefore, the pattern reconfigurable Yagi-Uda antenna was fabricated on FR4 PCB for short-range radiocommunication devices in the 2.435-2.465 GHz frequency range. An optimal antenna design is determined through a series of simulations. The proposed antenna is capable of re-directing the main beam toward one of four antenna regions (i.e. the 135° , 45° , 310° and 225° directions) to cover the azimuth plane. The measured impedance bandwidth of 8.2% with center frequency of 2.45 GHz for all four beams is achieved, and the realized gains range from 3.25 to 4.42 dBi, the variation of which is attributable to the PIN diodes characteristics. Due to its compact size, planar form and inexpensiveness, the proposed antenna possesses high potential to collaborate with phase array antenna, including sensor applications where workspace and budgetary considerations are of significance.

3.2.5 Applications

This section is further detail of application apart from achievement of a phased array antenna. The pattern reconfigurable antenna is presented on two sensor applications that use it to improve measurement results. The first one discusses the use of switched beam for detecting multiple targets that locates in different directions. The second one utilizes switched beam antenna for calibration of the system.

To detect multiple objects, the diagram of the beam switching reflectometer is shown in Fig. 3.27 where it consists of a reflectometer and a beam switching antenna. An ADF4351 frequency synthesizer generates 2.45 GHz with the output power of +12 dBm and feeds a dual directional coupler. The coupled incident and reflected powers are attenuated by attenuators to obtain the

acceptable level that feeds an AD8302 magnitude detector. The measured magnitude of reflection coefficient is displayed.

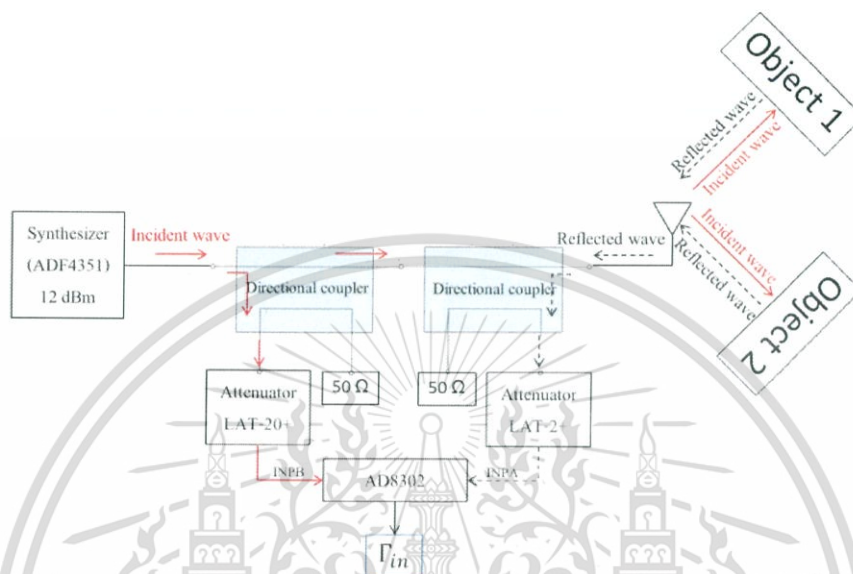


Fig. 3.27 Diagram of the beam switching reflectometer for detecting multiple objects

The object in this experiment was paper (Size A4 80gsm). The operation of antenna is referred to Fig. 3.8(a) and Table 3.4, which uses main beams in region 1 and 2, i.e. at 135° and 45° direction, respectively. The reflectometer was fixed and two pieces of paper were placed in the re-directing the main beam of the antenna. In Fig. 3.28(a), the main beam of region 1 was used for detecting "Paper 1" whereas "Paper 2" was detected by re-directing the main beam toward region 2. In the calibration, an aluminum plate was placed in front of the paper pieces, then the reflection coefficients were measured. As well known, the reflection coefficient of the conductor is 1. The measured reflection coefficient of each beam was normalized by the measured values to obtain 1 in both directions. When an aluminum plate was replaced by paper sheets, the measured reflection coefficients of the papers were measured and shown in 3.28(b). The moisture content range of paper was from 0% to 20% for analysis. It is obvious that each beam can distinguish between the different moist papers. When moistness rises, the magnitude of

reflection coefficient is increasingly related to moisture level due to amount of water in the paper under test.

Hence, this concept can assist to reduce cost since the more number of beams for measuring objects reduces the number of reflectometer systems at the expense of acquisition time.

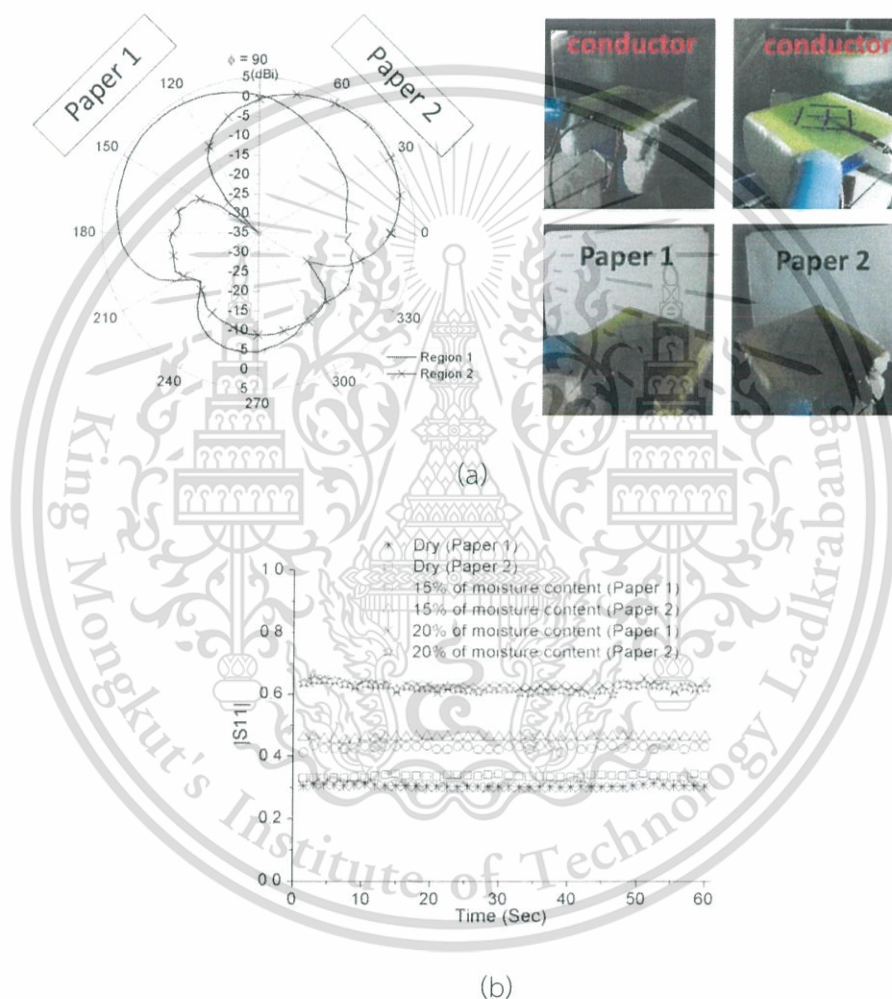


Fig. 3.28 Measurement of two targets which locate in different direction: (a) Azimuth patterns at 2.45 GHz, (b) Magnitude of reflection coefficient for different moisture content

In addition, other application is that a beam-switching reflectometer can be used to calibrate the system. Due to the size of the material under test is extra This material is reserved for educational use only, not allowed for commercial use.

Forbidden to modify the content, and cite the document when use.

large, it is sometimes difficult to replace a conducting plate with the material under test for calibration. The pattern reconfigurable antenna can solve this problem since main beam can be switched to many directions. One of main beams was undertaken for calibration system and the remaining main beam was used for measuring material under test.

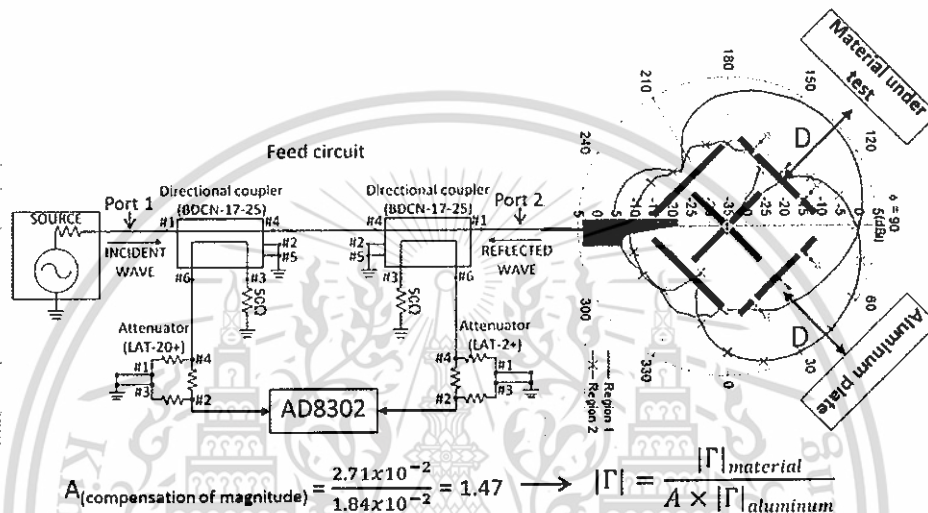


Fig. 3.29 Diagram of the beam switching reflectometer for calibration system

Table 3.5 Magnitude of reflection coefficient for aluminum plate in each main beam

Case	$ \Gamma_{11} $
Aluminum plate was placed at 135° (main beam for material under test)	2.71×10^{-2}
Aluminum plate was placed at 45° (main beam for calibration)	1.84×10^{-2}

In Fig. 3.29, an aluminum plate is fixed in main beam at 45° and material under test is target of main beam at 135° . The distances (D) of both directions must be identical. To examine system, aluminum plate was placed in both directions of main beam, measured reflection coefficient of aluminum plate is

illustrated in Table 3.5. It is obvious that those magnitudes are different. Therefore, the main beam for calibration will be compensated by magnitude ratio of reflection coefficient of the aluminum plate at 135° to that of the aluminum plate at 45° . Then, operation of main beam for calibration is as calibrating in the main beam for measuring material under test. This process causes convenient calibration by switching beam in two directions. The material of this confirmation was paper stack which has moisture between 15% and 20%. The antenna beam was switched toward the aluminum plate for calibration, and then compensates it. After that, main beam was switched toward the paper stack for measuring reflection coefficient. The measured reflection coefficient of paper stack was normalized by obtained value from main beam for calibration. The measured result of the paper stack is shown in Fig. 3.30. It is obviously noted that it can distinguish the different moistness of paper stack. The magnitude of reflection coefficient is positively correlated with moisture level. Therefore, this system can assist calibration for measuring the large material.

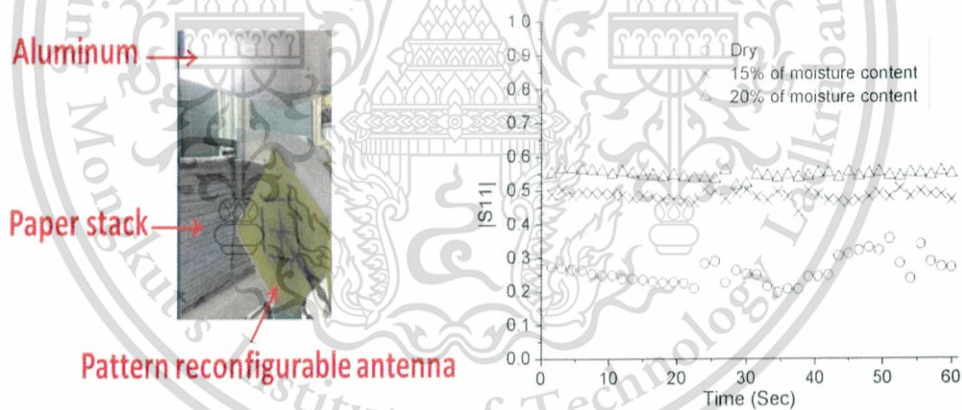


Fig. 3.30 Magnitude of reflection coefficient for different moisture content of paper stack

3.3 Phased array antenna using pattern reconfigurable Yagi-Uda antennas

Phased array antennas have been widely utilized in wireless communication and radar systems for convenient beam controlling, energy management advantages,

and reducing co-channel interference, etc [55]. To apply for beam-scanning reflectometer, main beam should scan with wide angle according to chapter 2. The construction of the phased array antenna comprises multiple stationary antenna elements, which are fed with variable phase at each element to scan a beam in space. Also, the scanning angle and gain of phased array are associated with antenna elements. In addition, it is well known that gain decreases more than 3dB when scanning angle of phased array increases beyond 3-dB beam angle (HPBW) of antenna element. This effect is a common problem of scanning angle of array antenna. To reduce this problem, many techniques have been reported to enhance scanning angle. One of approaches is developed by enlarging 3-dB beam width of antenna element [56]. The wide beam antenna for wide scanning array was designed by using printed dipole antenna [57]. The beam width of the printed dipole antenna was extended with addition of parasitic element, which offered 120° in E-plane. Then, antenna was utilized for array antenna, resulting in scan angle increased from $\pm 50^\circ$ to $\pm 60^\circ$. Also, a meander-line microstrip antenna was presented in [58] for wide beam, and the antenna provided a beam width of 130° in the E-plane. The corresponding phased array can scan its main beam to $\pm 60^\circ$. However, wide beam of antenna elements causes high side lobe level and average gain contribution from each element will be low due to a wider beam. Furthermore, gain of array antenna decreases when main beam of the array scans to larger angle than HPWB angle of antenna element. Alternatively, pattern-reconfigurable antenna is another way to enhance the scanning range of a phased array and to reduce the scanning gain fluctuation [59]-[61]. In [59], the beam of antenna elements can be switched in two directions, which forms to have four-element circular array by using one-bit phase shifters. It was found that various combinations of element patterns cause increased transformation of shape beam, including main beam switched around four-quadrant of the array antenna. In [60]-[61], pattern reconfigurable antennas were designed for switching beam in three states and fed with principle of a progressive phase. When the array scans to different regions, all the elements operate in accordant states and then the overall scanning range is expanded. By using this method, scanning range of phased array with pattern reconfigurable antennas can reach $\pm 60^\circ$ for [60] and $\pm 70^\circ$ for [61], while maintaining the scanning gain flatness. However, they were designed on the basis of microstrip antenna which metal ground usually appears at the

bottom of the structure and generates the mirror effect. Radiation from the surface current on the patch and the mirror current will offset at the end-fire direction. This phenomenon is serious to scan the main beam in horizontal plane. In addition, number of beam for antenna element influences scanning beam, and therefore, the beam-scanning range of the phased array is restricted.

As a result, the effectiveness of using pattern reconfiguring for wide-angle scanning applications is emphasized. In order to design followed structure of proposed sensor, the phased array antenna is developed by using pattern reconfigurable antenna, which describes in section 3.2. The proposed array is linear array with two antenna elements, operating at frequency of 2.45 GHz. In addition, the array antenna has to scan beam in a horizontal plane, which utilizes one-bit phase shifter to minimize loss and complexity of the system.

3.3.1 Linear array antenna

Let us illustrate that the two-element linear array formed by electric field vector of individual antenna element is shown in Fig. 3.31, and the electric field of array (E_{TA}) in y-z plane is described by the following formula:

$$E_{TA}(\theta) = E_1(\theta_1) e^{j(k\frac{d}{2}\sin\theta + \beta_1)} + E_2(\theta_2) e^{-j(k\frac{d}{2}\sin\theta - \beta_2)} \quad (3.14)$$

where $E_1(\theta_1)$ and $E_2(\theta_2)$ are electric field pattern of the element 1 and 2, respectively, θ is the radiation angle of the array, $k = \frac{2\pi}{\lambda}$ is the phase constant and λ is the wavelength in free space at the operation frequency, d is distance between elements, β_1 and β_2 represent the phase excitation of the element 1 and 2 in the array, respectively.

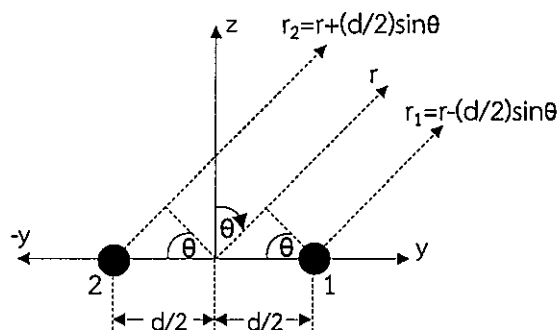


Fig. 3.31 Configuration of linear phased array

In equation 3.14, the maximum of electric field pattern occurs when

$$k \frac{d}{2} \sin \theta + \beta_1 = 0 \text{ and } k \frac{d}{2} \sin \theta - \beta_2 = 0 \quad (3.15)$$

To consider phase excitation, equation 3.15 is main formula for explanation. If maximum radiation of an array needs to direct toward normal to the axis of the array, it will be known as broadside direction. Since it is desired to have the maximum directed toward either $\theta = 0^\circ$ or 180° which refer to Fig. 3.31, then phase excitation of each element is given by

$$k \frac{d}{2} \sin \theta + \beta_1 |_{\theta=0^\circ \text{ or } 180^\circ} = \beta_1 = 0 \quad (3.16a)$$

$$k \frac{d}{2} \sin \theta - \beta_2 |_{\theta=0^\circ \text{ or } 180^\circ} = \beta_2 = 0. \quad (3.16b)$$

Thus, it is necessary that all the elements have the same phase excitation for broadside direction. In addition, main beam may be desirable to direct it along the axis of the array, called as end-fire direction. (end-fire; either $\theta = 90^\circ$ or 270° of Figure 3.31). If it is desired to have the maximum directed toward $\theta = 90^\circ$, then

$$k \frac{d}{2} \sin \theta + \beta_1 |_{\theta=90^\circ} = \beta_1 = -k \frac{d}{2} \quad (3.17a)$$

$$k \frac{d}{2} \sin \theta - \beta_2 |_{\theta=90^\circ} = \beta_2 = k \frac{d}{2}. \quad (3.17b)$$

Similarly, when maximum is desired toward $\theta = 270^\circ$,

$$k \frac{d}{2} \sin \theta + \beta_1 |_{\theta=270^\circ} = \beta_1 = k \frac{d}{2} \quad (3.18a)$$

$$k \frac{d}{2} \sin \theta - \beta_2 |_{\theta=270^\circ} = \beta_2 = -k \frac{d}{2}. \quad (3.18b)$$

It is noted that end-fire radiation is accomplished when element 1 and 2 are excited at different phases, and the maximum radiation is directed toward element which excites lagging phase. (β_1 lags β_2 for $\theta = 90^\circ$ or β_2 lags β_1 for $\theta = 180^\circ$)

By using equation 3.14-3.18, the main beam direction of array will be changed according to phase excitation. In addition, the distance between elements is parameter which can modify for performance of array antenna. Therefore, these parameters will be processed for array antenna design.

3.3.2 Design of phased array with pattern reconfigurable antennas

The pattern reconfigurable antenna has already been presented in section 3.2. In this section, two-element linear array is designed by using pattern reconfigurable antenna elements. The design of array antenna will be considered on structure of a novel beam-scanning reflectometer. This causes three criteria for array antenna design: (1) to be operable in the frequency of 2.45 GHz, which is based on ISM bands for measuring orange fruit; (2) to scan main beam in 8 directions in horizontal plane; and (3) to investigate the advantage for wide angle scanning applications.

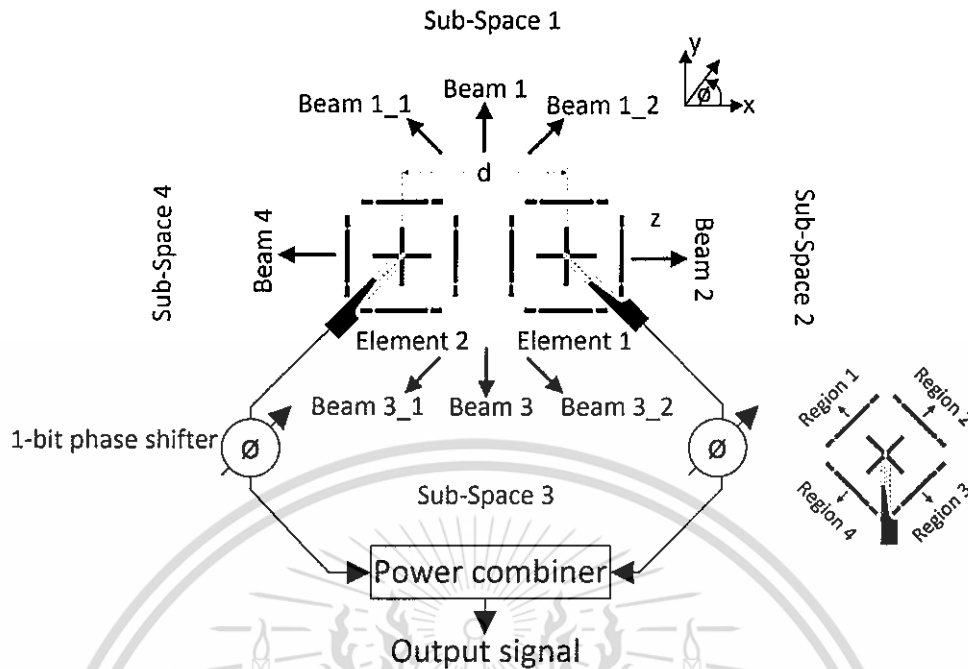
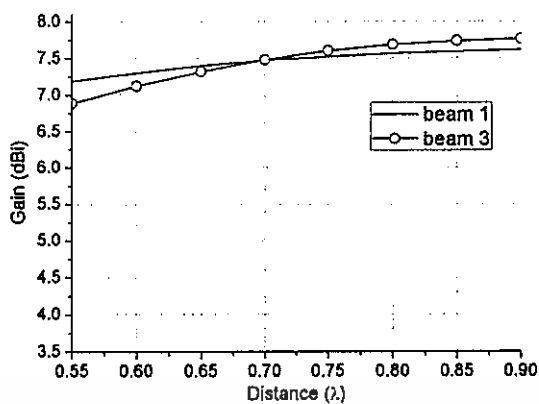
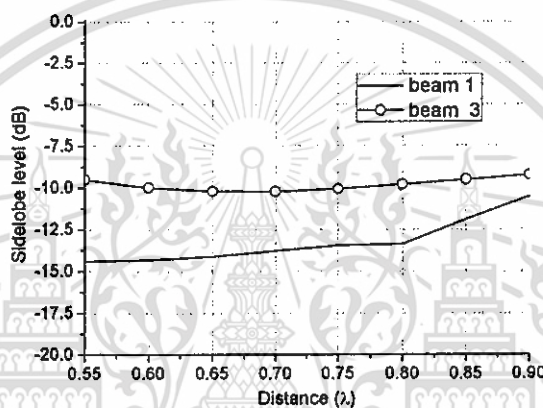


Fig. 3.32 Geometry of the phased array of pattern reconfigurable antennas.

In order to get a general understanding of how the antenna element works for switching beam of the array, a simplified illustration on the structure is given in Fig. 3.32. The scanning space of a phased array is divided into four sub-spaces. Each sub-space respectively matches with one of the reconfigurable beams of each element. When all the pattern reconfigurable elements are set to one of the reconfigurable states, beam scanning in the corresponding sub-space can be completed according to the principle of a phased array. To illustrate about this idea, Fig. 3.32 shows that each element 1 and 2 can cover regions in 4 directions, as depicted in the inset. The main beams of element 1 and 2 point to region 2 and 1, respectively, for 'sub-space 1' signal reception. The signal reception of 'sub-space 4' is jointed with element 1 and 2 pointed to region 1 and 4. Similarly, the cases of the other sub-space are accomplished by pointing main beam of elements toward desired sub-space. Throughout this section, switching beam of element will be performed as the above mentioned process.



(a)



(b)

Fig. 3.33 Simulation results in case of distance variation (d) for the main beam in 'Beam 1' and 'Beam 2': (a) gain relative to distance, (b) sidelobe level relative to distance.

The separation between element 1 and 2 (d) was varied to get the highest gain and lowest side-lobe level. 'Beam 1' of 'sub-space 1' and 'Beam 3' of 'sub-space 3' was used for considering separation. Since main beam of 'Beam 1' and 'Beam 3' act as broadside direction, thus, phase excitation of all elements were in-phase for simulation. In Fig. 3.33, the simulated results are found that gains are positively correlated to d , while the sidelobe level decreases until arriving at 0.70λ ($\lambda = 122.45$ mm). In addition, sidelobe level of 'Beam 3' is higher than that of 'Beam 1' due to effect of asymmetrical ground plane of microstrip-to-CPS transition. Hence, distance (d) for sidelobe level < -10 dB and highest gain is optimal at 0.75λ .

Then, 'Beam 2' of 'sub-space 2' and 'Beam 4' of 'sub-space 4' were used to determine phase excitation with one-bit. Since beam directions perform as end-fire direction. To calculate phase excitation, equations 3.17-3.18 were utilized by using distance between elements at 0.75λ , and then phase excitation for one-bit (β) was estimated as

$$k \frac{d}{2} \sin \theta \pm \beta \Big|_{\substack{d=0.75\lambda \\ \theta=90^\circ \text{ or } 270^\circ}} = \beta = \pm 135^\circ . \quad (3.19)$$

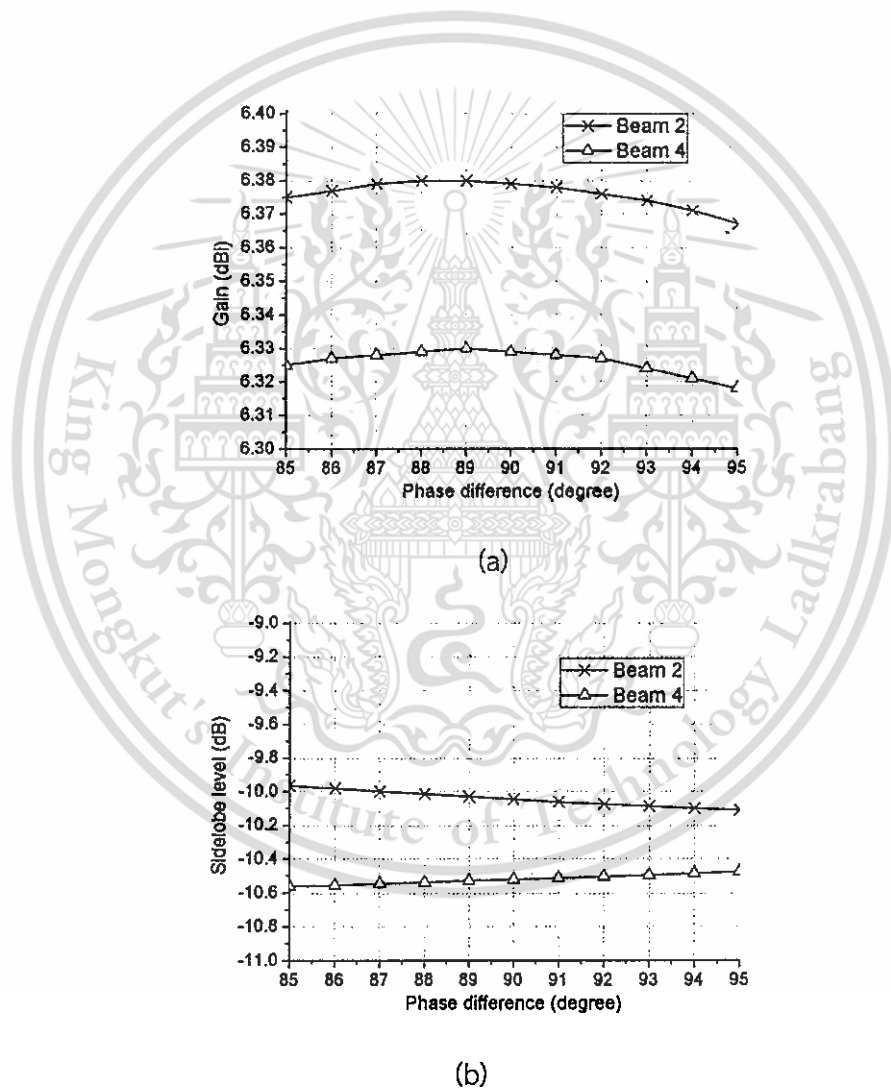


Fig. 3.34 Simulation results in case of phase variation for the main beam in 'Beam 2' and 'Beam 4': (a) gain relative to phase difference, (b) sidelobe level relative to phase difference.

However, this value was obtained from calculation which defines as identical amplitudes. Thus, phase excitation would be replicated by combining effect of pattern reconfigurable antenna. The further simulation started from phase excitation of $\pm 135^\circ$ and fed according to end-fire array. For example of 'Beam 2', the element 1 excited with phase of $+135^\circ$ whereas the element 2 excited with phase of -135° . The phase difference between both elements will be 90° for initial determination, and then the phase difference was varied in the $90^\circ \pm 5^\circ$ range for determining good condition. The simulated result of phase excitation is shown in Fig. 3.34. It is found that the variation in the phase difference impacts the radiation performance of the main beam. As phase difference increases, gain of the 'Beam 2' and 'Beam 4' increase until arriving at 89° . While, the sidelobe level for 'Beam 2' is less than -10 dB when phase difference is higher than 87° . Therefore, the phase difference of 89° is selected and the phase excitation for one-bit is $\pm 135.5^\circ$ for operation.

Moreover, areas of 'sub-space 1' and 'sub-space 3' can scan main beam with principle of end-fire array. For 'sub-space 1', the beam patterns of element 1 and 2 are switched toward region 2 and 1, respectively. Then, element 1 and 2 are excited at different phases: -135.5° and $+135.5^\circ$ respectively. These appearances result in main beam which tilts to left side of 'Beam 1', i.e. 'Beam 1_1' in Fig. 3.32. While 'Beam 1_2' tilted to right side of 'Beam 1', the beam patterns of element 1 and 2 are also toward region 2 and 1, respectively but element 1 and 2 are excited with phases of $+135.5^\circ$ and -135.5° , respectively. For 'sub-space 3' with end-fire array, it is similar processed which main beam of each element are switched toward sub-space 3. Then, phase excitation of elements will be executed according to principle of end-fire array.

As above mentioned, the feed and operation of the antenna will be summarized in the Table 3.6 and the separation between both elements is 0.75λ . In addition, these specifications will be simulated to explain all radiation patterns at 2.45 GHz, which are illustrated in Fig. 3.35. The orientation of all radiation patterns refers to that of the coordinate system in Fig. 3.32. It is noted that the phased array antenna can scan in each of the following directions: 73° , 88° , 104° , 182° , 256° , 270° ,

284°, and 355°. The simulated gains of the scanning patterns at 2.45 GHz are between 6.4 and 7.6 dBi. For other radiation characteristics, it is elaborated in Table 3.7.

Table 3.6 Operation of the array antenna

Beam	Beam direction of elements and Phase excitation	
	Element 1	Element 2
1_1	Region 2, -135.5	Region 1, +135.5
1	Region 2, -135.5	Region 1, -135.5
1_2	Region 2, +135.5	Region 1, -135.5
2	Region 3, +135.5	Region 2, -135.5
3_1	Region 4, -135.5	Region 3, +135.5
3	Region 4, -135.5	Region 3, -135.5
3_2	Region 4, +135.5	Region 3, -135.5
4	Region 1, -135.5	Region 4, +135.5

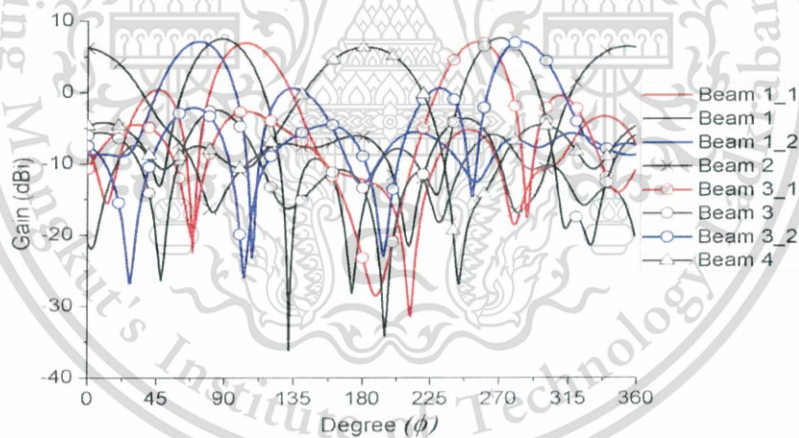


Fig. 3.35 Simulated radiation characteristics of the eight-beam array

Table 3.7 Simulated radiation characteristics of eight-beam antenna

Beam	Simulated results of radiation pattern			
	Main beam	Gain (dBi)	SLL (dB)	HPBW
1_1	104°	6.96	-6.54	36°
1	88°	7.53	-13.44	36°
1_2	73°	7.14	-6.50	36°

This material is reserved for educational use only, not allowed for commercial use.

Forbidden to modify the content, and cite the document when use.

Table 3.7(cont.) Simulated radiation characteristics of eight-beam antenna

Beam	Simulated results of radiation pattern			
	Main beam	Gain (dBi)	SLL (dB)	HPBW
2	355°	6.38	-10.03	57°
3_1	256°	7.09	-7.53	33°
3	270°	7.60	-10.06	33°
3_2	284°	7.14	-6.51	33°
4	182°	6.33	-10.53	56°

Therefore, simulation of phased array indicates that main beam can scan in eight directions around the array antenna by using pattern reconfigurable antenna. When the phased array scans toward different directions, the gain fluctuation is less than 1.2 dB with a maximum scanning gain of 7.6 dBi. Finally, simulated results of main beam can appropriately operate at 2.45 GHz frequency according to the design.

3.3.3 Feed system of the proposed array antenna

The configuration of the proposed phased array antenna is shown in Fig. 3.32. In practice, the two-element linear array is fed with the feed system which consists of phase shifters and a power combiner. The phase shifters are used to shift the phase excitation of each element to switch the beam toward the defined direction, while a power combiner is a three-port network that can be used for power division. Both devices are important to operation of the phased array antenna.

The phase shifter is based on a switched delay line, as shown in Fig. 3.36. The switched delay line phase shifter uses different length of transmission lines to produce a differential phase shift [33]. Two transmission lines of length L_1 and $L_1 + \Delta L$ are reference path and delayed path, respectively. Three PIN diodes (P_1 , P_2 , and P_3) are used to switch the signal path with either on or off state. On state of PIN diode indicates connection between anode and cathode point. On the other hand, off state of PIN diode indicates disconnection. When PIN diode of P_1 is connected to the transmission line of length L_1 while PIN diodes of P_2 and P_3 are disconnected to

the transmission line of length $L_1 + \Delta L$. This results in the signal passes through the reference path of length L_1 . As, PIN diodes of P_1 is disconnected to the transmission line of length L_1 and PIN diodes of P_2 and P_3 are connected to the transmission line of length $L_1 + \Delta L$, the signal passes through the delayed path of length $L_1 + \Delta L$. It is noted that the delay of the signal is different of the length ΔL . Therefore, the phase shift is given by $k\Delta L$; k = propagation constant ($k = \frac{2\pi}{\lambda}$).

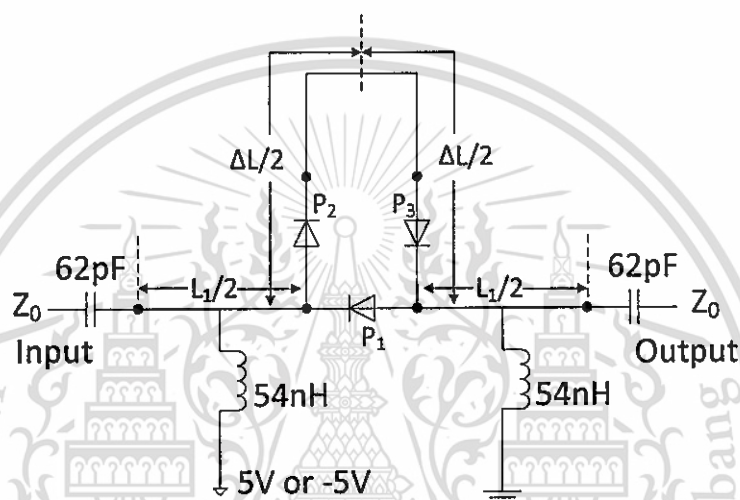


Fig. 3.36 Circuit of the designed 1-bit phase shifter..

For this work, the one-bit phase shifter must have phase difference of 89° (phases of $\pm 135.5^\circ$) to excite two elements of the phased array antenna. The phase shifter was fabricated on an FR4 substrate, with a dielectric constant of 4.24, loss tangent of 0.012 and a thickness of 1.6 mm. Three Philips BAP50-02 PIN diodes were used for switching between the delay line and reference line according to Fig. 3.36, including the RF choke and capacitor for bias tee circuit. In addition, PIN diodes would be biased with 10 mA current for operation of each mode. Fig. 3.37 shows a prototype of one-bit phase shifter and its dimensions are elaborated. The characteristics of the phase shifter were examined at the frequency of 2.45 GHz. The measured results are shown in Table 3.8. The reflection coefficient is less than -14 dB, insertion loss is 1.4 dB and phase error is less than 0.5° throughout the operating at 2.45 GHz.

This material is reserved for educational use only, not allowed for commercial use.

Forbidden to modify the content, and cite the document when use.

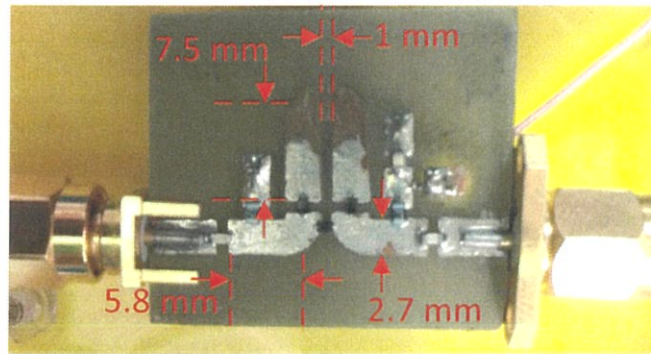


Fig. 3.37 Prototype of the 1-bit phase shifter

Table 3.8 Characteristic of one-bit phase shifter at 2.45 GHz

Mode	$ S_{11} $ (dB)	Insertion loss (dB)	Phase error
$P_1 = \text{On}$ P_2 and $P_3 = \text{Off}$	-20.3	0.68	-0.4°
$P_1 = \text{Off}$ P_2 and $P_3 = \text{On}$	-14.5	1.4	

Similarly, a two-way power combiner is employed to combine the received signals of two array elements. In order to combine power, the Wilkinson power combiner is utilized for feeding system of the array antenna. It consists of three-port network that can match at all ports and have isolation between the input ports [33]. The equivalent transmission line circuit is shown in Fig. 3.38. Since impedance of the antenna system is designed with 50Ω , therefore, three ports of the combiner are defined as 50Ω ($Z_0 = 50 \Omega$). The quarter-wave lines have impedance of 70.7Ω ($\sqrt{2}Z_0$), and shunt resistance is 100Ω ($2Z_0$). Then, it was also designed and fabricated on the FR4 substrate. The prototype of the two-way power combiner is shown in Fig. 3.39. The characteristics of the power combiner were examined at 2.45 GHz frequency. The theoretical loss of the two way combiner will be half of the input power at each port. However, it will be higher than a 3dB loss at ports since the combiner may be mismatch, resulting in further loss, known as insertion loss. The measured results found that the insertion loss was 0.85 dB. The

reflection coefficient was less than -15 dB for each port and isolation between input ports was 20.23 dB.

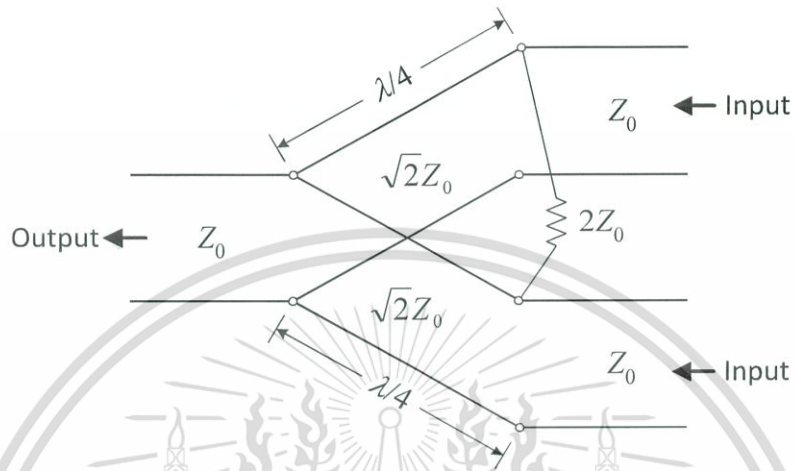


Fig. 3.38 Equivalent transmission line circuit of the Wilkinson power combiner [33]

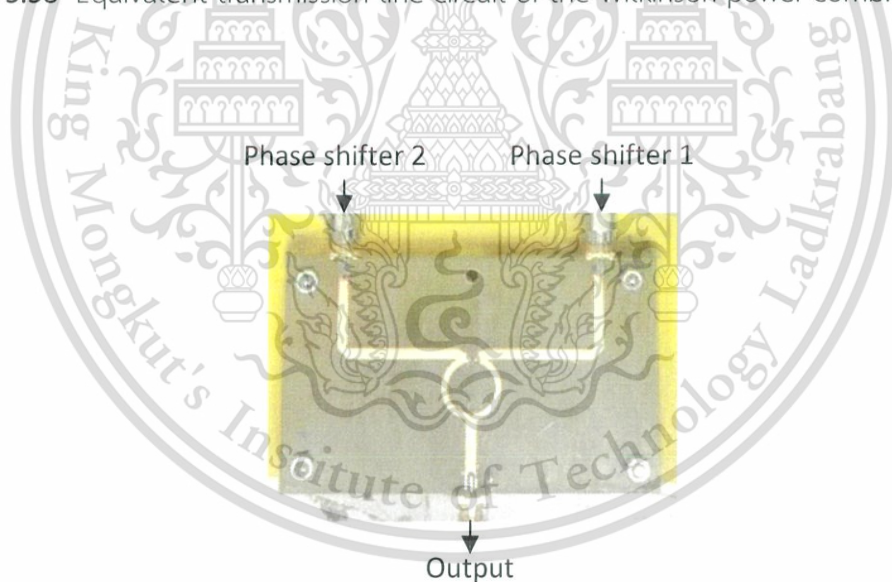


Fig. 3.39 Prototype of the two way power combiner.

3.3.4 Implementation of the proposed array antenna

The phased array antenna was fabricated on basis of section 3.3.2 by using the pattern reconfigurable antenna in section 3.2. The electrical mechanism

This material is reserved for educational use only, not allowed for commercial use.

Forbidden to modify the content, and cite the document when use.

still uses to operate in array antenna, including in feeding system of the antenna. The operation of the array antenna must be accordant with Table 3.6 and distance between both elements of the array is 0.75λ . In order to bias the circuit, the wire lines were etched on FR4 substrate which those wires connected toward DC biasing voltage points. The RG 316 coaxial was used to connect between antenna elements and the feed system. Fig. 3.40 (a) and (b) are photographs of prototype array antenna for top view and side view, respectively. Fig. 3.40(c) is a photograph of the feed network which combines with power combiner and two phase shifters. It was covered by a black RF absorber to reduce reflection. The insertion loss in the feed system was 2 dB.

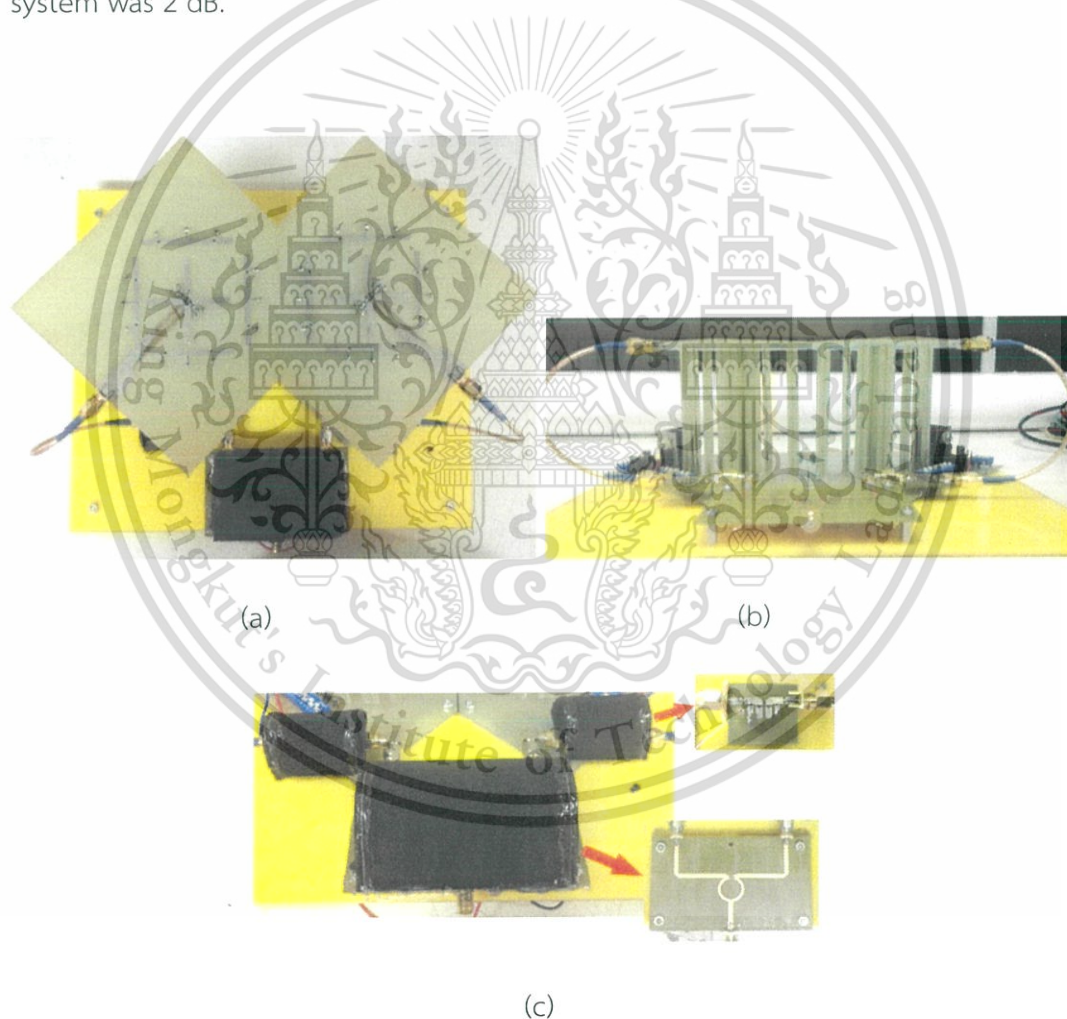
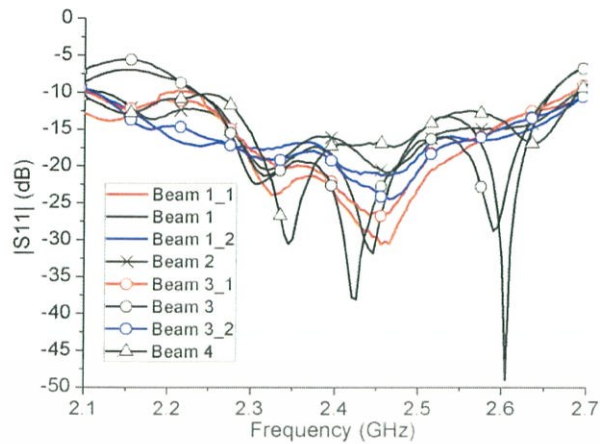
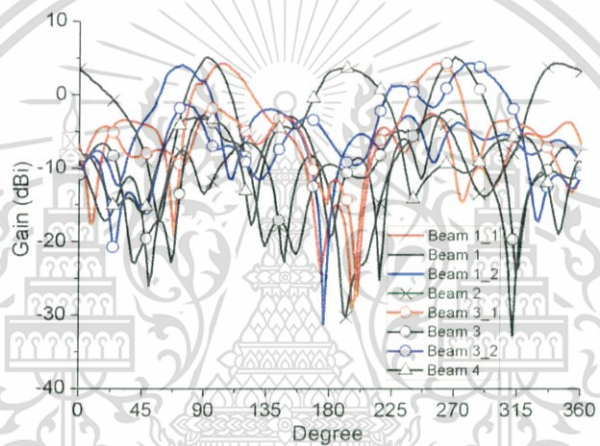


Fig. 3.40 Photographs of the phased array antenna: (a) Top view, (b) Side view, and (c) Feeding system.



(a)



(b)

Fig. 3.41 Measured results of the phased array antenna. (a) $|S_{11}|$ for different main beams. (b) Gain patterns.

Fig. 3.41(a) shows measured results that reflection coefficient of all the main beam are less than -10 dB at 2.45 GHz. This results in radiated power over 90% of total power.

Far-field radiation patterns were measured for the eight states of the proposed antenna. The orientation of the rectangular coordinate system was used in radiation pattern is the same as the one shown in Fig. 3.32. The dc power supplies were placed inside an anechoic chamber and covered with absorbers during measurement. Fig. 3.41(b) shows the measured E-plane radiation patterns for the

eight main beams at 2.45 GHz. It is noted that radiation patterns of measured result agree reasonably well with those of simulated result in Fig. 3.35. The measured maximum beam radiations can scan at 74°, 92°, 106°, 186°, 257°, 270°, 284°, and 349°. The realized gains were in a range of 4 to 5.23 dBi. However, realized gains are less than simulated gains since simulation did not include the insertion loss of feed network. In addition, it is noted that the measured sidelobes level are greater than the simulated ones. This discrepancy can be due to the unshielded RF cables and dc biasing lines attached to the antenna. All radiation characteristics of measurement are summarized in Table 3.9.

Table 3.9 Measured radiation characteristics of eight-beam antenna

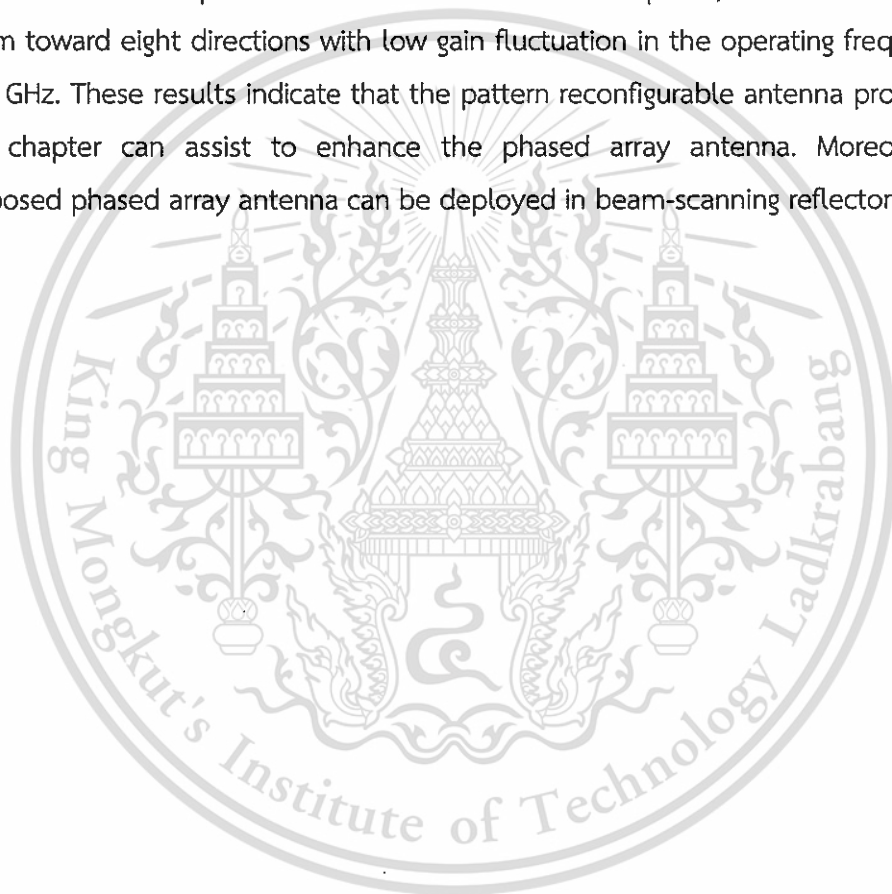
Beam	Measured results of radiation pattern			
	Main beam	Gain (dBi)	SLL (dB)	HPBW
1_1	106°	4.28	-6.87	36°
1	92°	5.11	-7.13	24°
1_2	74°	4.10	-6.04	34°
2	349°	4.36	-7.22	44°
3_1	257°	4.30	-6.14	32°
3	270°	5.23	-8.04	28°
3_2	284°	4.38	-4.35	34°
4	186°	4.08	-6.76	46°

The beam-scanning performance is found that the main beam can scan toward eight directions around it. Moreover, when phased array scans its beam, gain fluctuation is less than 1.2 dB. These results indicate that the proposed array antenna can be utilized for beam-scanning applications.

3.4 Conclusion

In this chapter, the pattern reconfigurable Yagi-Uda antenna is designed and analyzed. It can switch main beam toward one of four regions to cover the horizontal plane. The impedance bandwidth is 8.2% with center frequency of 2.45

GHz for all four beams, and the realized gains are range from 3.25 to 4.42 dBi. This antenna has been presented on sensor applications that use it to detect multiple targets and to assist calibration for measuring the large material. Furthermore, the proposed pattern reconfigurable antenna can be served as elements of the phased array antenna. It has been designed and fabricated on structure of two-element linear array. An optimal design of array antenna is determined from a principle of linear array and the simulated results. The beam pattern of elements and 1-bit phase shifter are main parameters for operating proposed array antenna. The measured radiation patterns are radiated in horizontal plane, which can scan main beam toward eight directions with low gain fluctuation in the operating frequency of 2.45 GHz. These results indicate that the pattern reconfigurable antenna proposed in this chapter can assist to enhance the phased array antenna. Moreover, the proposed phased array antenna can be deployed in beam-scanning reflectometer.



CHAPTER 4

IMPLEMENTATION OF BEAM-SCANNING REFLECTOMETER

4.1 Introduction

In this chapter, a novel reflectometer is analyzed from the theoretical background and the antenna design presented in the previous chapters. The beam-scanning antenna is utilized to advance traditional reflectometer measurement and it is expected to improve for identifying material accurately. The proposed reflectometer will be designed and fabricated which refers to Fig. 2.13. Algorithm for identifying material's property is based on k-factor calculation. In order to investigate sensitivity of sensor system, plasticine model either with or without one missing section is used for initial test. Then, real tangerine fruits will be measured to classify granulated tangerine.

4.2 Sensor system design

The concept of the beam-scanning reflectometer has been briefly presented in section 2.5. To setup experimentation, the structure of the sensor system must be suitable for a continuous process. This reason results in the configuration of proposed system which is shown in Fig. 4.1.

The unidirectional antenna #1 is used for illuminating microwave signal on a spherical fruit which the cross dipole antenna over a ground plane is utilized. The far-field distance between the cross dipole antenna and a spherical fruit is 6 cm. A frequency synthesizer module is used to generate microwave signal regulated by a controller. The controller not only controls the frequency synthesizer but also the radiation pattern of antenna #2 which, in principle of beam-scanning, can scan by either mechanical rotation or electronic processing. To avoid mechanical scanning,

this work uses electronic scanning accomplished by the proposed phased array antenna in section 3.3. In addition, the space between antenna #1 and #2 is 14-cm that the isolation between the two antennas was 30 dB. Furthermore, the size of the sensor system was a manageable one, so the spacing between the reflector and the phased array antenna was not as far apart as 35 cm of the far-field region. The radiation patterns for 20, 30, and 40 cm away from the array antenna were measured and plotted, as shown in Fig. 4.2. The nulls in the near-field region were not as deep as in the far-field range but the main beams were still in the same directions, so we chose the smallest spacing of 20 cm.

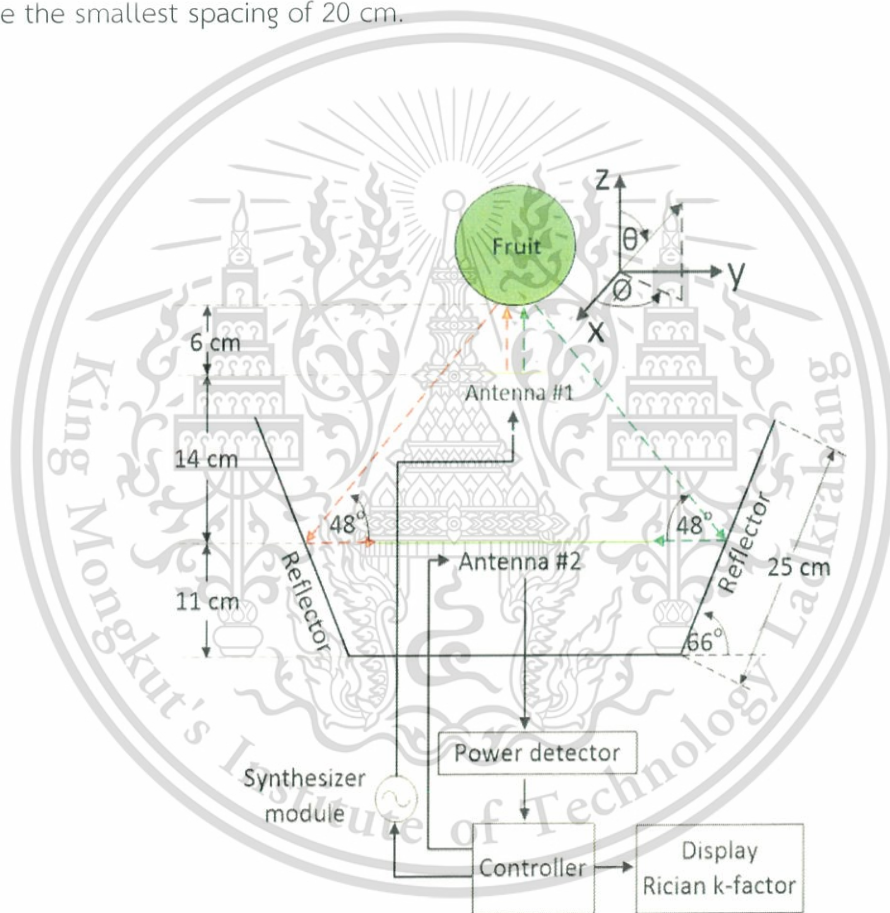


Fig. 4.1 Configuration of the beam-scanning reflectometer.

Then, scattered waves from the fruit incident on a conical reflector with an inclined angle of $\alpha = 66^\circ$ (depicted in Fig. 4.1). The conical reflector with the 25-cm dimension reflects waves to the beam-scanning antenna #2. When this antenna captures the signals from around a conical reflector and passes them along to a

power detector that converts the collected signal into D.C. signal which is then input into the controller that calculates the Rician k-factor.

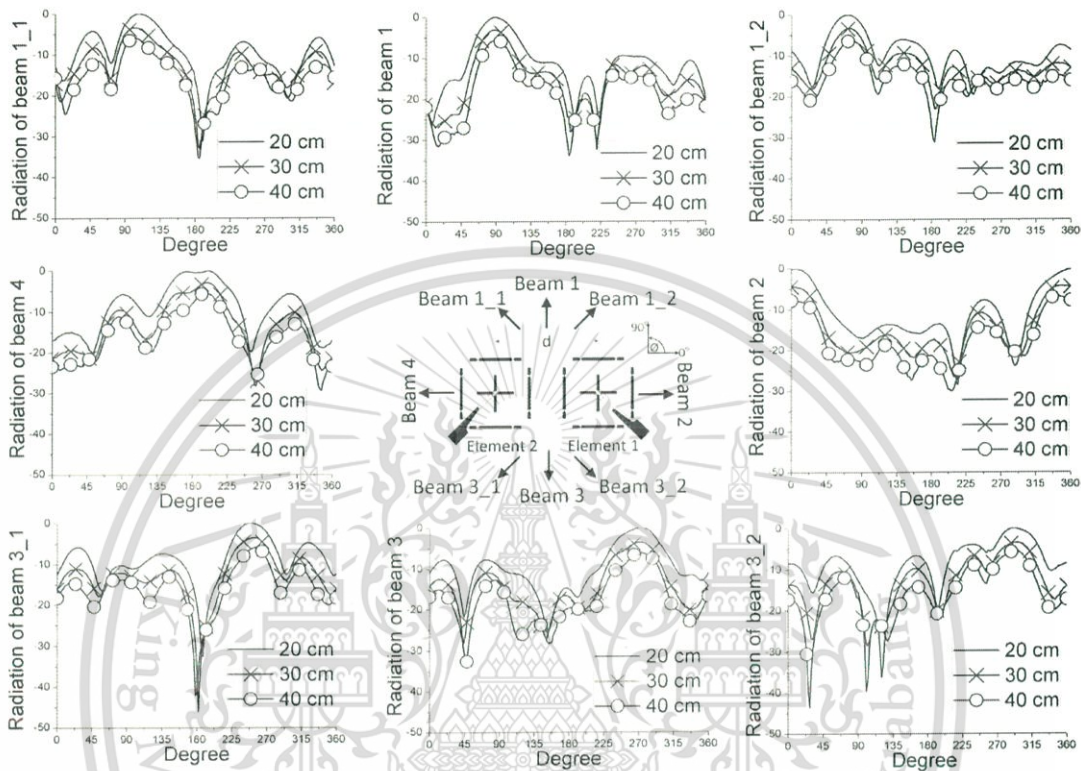


Fig. 4.2 Radiation patterns at different distances.

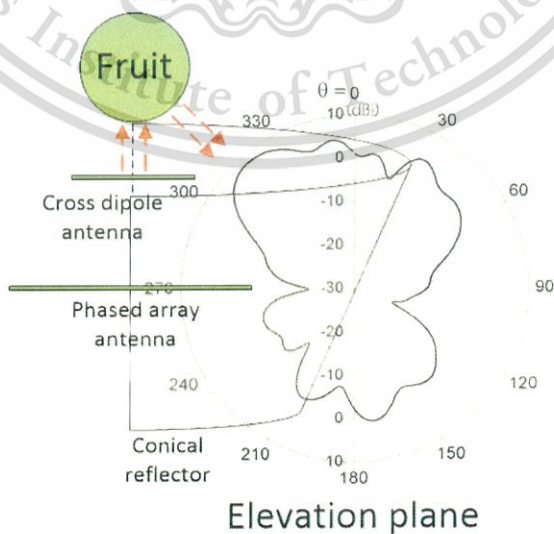


Fig. 4.3 Radiation pattern of 'Beam1' with a conical reflector.

This material is reserved for educational use only, not allowed for commercial use.

Forbidden to modify the content, and cite the document when use.

Fig. 4.3 shows the simulated elevation pattern of the antenna system consisting of array antenna ('Beam 1' in Table 3.6) and a conical reflector. The conical reflector with an inclined angle of 66° produced a main beam in the direction of 319° which was the direction of the scattered wave from the fruit. The 3-dB beamwidth in elevation and azimuth planes were 27° and 40° , respectively. The gain of the antenna system (G_s) was 8.06 dBi. Similar results were obtained from beams from other directions. Fig. 4.1 shows the input power (P_{in}) at 2.45 GHz fed a cross dipole antenna over a ground plane which had a gain (G_c) of 4.6 dBi. The cross dipole antenna was used to illuminate the granulated tangerine model in order to determine the radar cross section (RCS). The RCS of the granulated section (σ_g) was $2.18 \times 10^{-3} \text{ m}^2$. The incident waves on the tangerine model were captured and reradiated to the antenna system. The radar range equation [52] was used to calculate the received power (P_r) given in equation 4.1.

$$P_r = \frac{P_{in}(\sigma_g)|G_c||G_s|}{4\pi} \left[\frac{\lambda}{4\pi(R_1)(R_2)} \right]^2 \quad (4.1)$$

where R_1 and R_2 were distances from antenna #1 to the tangerine model and from the tangerine model to the conical reflector, respectively. They were 6 cm and 30 cm, respectively. The acquired power of each beam from the tangerine model was converted to magnitude (M_i) in order to calculate the k-factor. The mean (S) and variance (σ^2) of this system were calculated from the magnitudes of scattered wave in 8 directions, as defined in equation 4.2 and 4.3. Then, the k-factor obtained was as expressed in equation 2.15.

$$S = \frac{1}{8} \sum_{i=1}^8 M_i \quad (4.2)$$

$$\sigma^2 = \frac{1}{8} \sum_{i=1}^8 (M_i - S)^2 \quad (4.3)$$

where M_i is a sampled magnitude of the scattered wave around the fruit (M_1, M_2, \dots, M_8) which was captured from each of the 8 directions received by the phased array antenna.

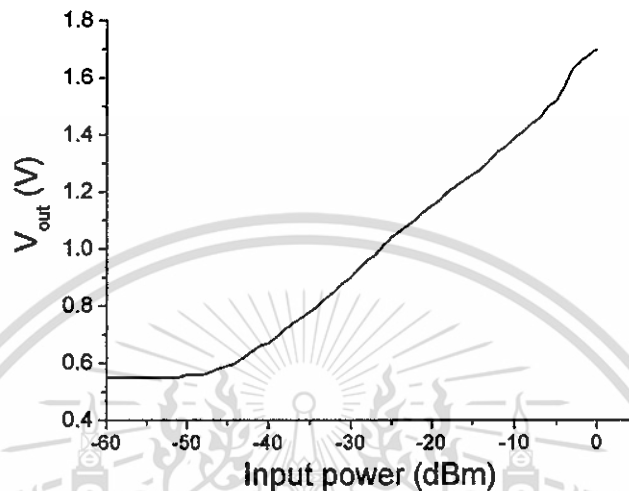


Fig. 4.4 Measured result of MAX4003 characteristic.

Table 4.1 summarizes the received power, signal to noise ratio (SNR) and uncertainty (U) of the system. A Max4003 power detector module operating linearly between -40 dBm to 0 dBm was used, which as shown in Fig. 4.4. SNR was calculated with a noise floor (P_n) of -40 dBm (1×10^{-4} mW). As expected, the calculated SNR of the granulated tangerine model increased when input power was increased. In addition, this noise floor had an effect on the uncertainty of k-factor. The value of k-factor varied in the range of $k = k_c \pm \Delta k$ where k_c was the correct value and Δk was the uncertainty from the noise floor. The percentage of uncertainty was derived from $\left(\frac{\Delta k}{k_c} \times 100\right)$ which should be low at high SNR. Shown in Table 4.1, the input power of 15 dBm provided 24.72 dB of SNR and 1.83% of uncertainty. Because of all of these results, the input power of 15 dBm was selected for further use in this work.

Table 4.1 Calculated results of received power and signal-to-noise ratio

Input power (W)	Granulated model		
	Received power (W)	SNR (dB)	Uncertainty (%)
1×10^{-3} (0 dBm)	9.37×10^{-7} (-30.28 dBm)	9.72	55.01
3.16×10^{-3} (5 dBm)	29.6×10^{-7} (-25.28 dBm)	14.72	18.28
10×10^{-3} (10 dBm)	93.7×10^{-7} (-20.28 dBm)	19.72	5.80
31.6×10^{-3} (15 dBm)	296.4×10^{-7} (-15.28 dBm)	24.72	1.83

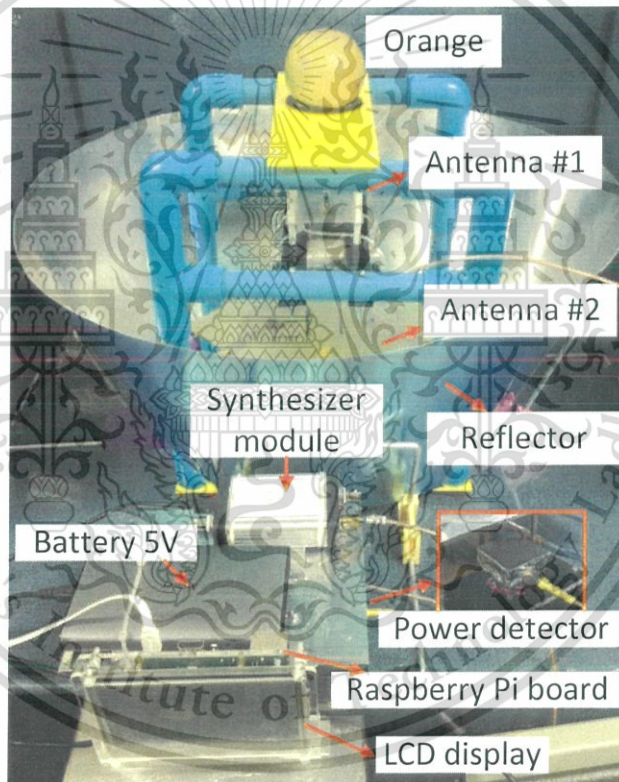


Fig. 4.5 Photograph of the proposed system.

Fig. 4.5 shows a photograph of the constructed system. A TPI synthesizer version 5 module controlled by a Raspberry Pi generated 2.45 GHz signal with an output power of +15 dBm. The phased array antenna received reflected waves from the reflector and input them to a MAX4003 power detector. Then, the D.C. signal

was converted into a digital signal by an MCP3008 10-bit analog to digital converter (ADC) and input into the Raspberry Pi to calculate k-factor. Note that 10 bits of ADC can detect power with a 0.2 dB resolution. A suitable threshold value of k-factor for classifying normal or granulated tangerine was determined. In addition, the sensor system was used to measure waves without any object to scatter them and found that the isolation between the two antennas was 30 dB.

4.3 Experimental results

To examine sensitivity of the proposed beam-scanning reflectometer, the experiments will be divided into two sections: those use a plasticine model which is used to represent tangerine fruit for initial test, and those use real tangerine fruits which are the target fruit for classifying quality of the fruit. Sensitivity of the k-factor will be illustrated for both experiments.

4.3.1. Results from a plasticine model with one missing section

In practice, the position of granulation is not known and it is desirable to know the effect of position of granulation on the Rician k-factor. Furthermore, it is necessary to know the effect of size of tangerine and the number of beams of the antenna on the Rician k-factor. Plasticine is a material that can change its shape easily. The preparation of a spherical plasticine to have a missing section and have different size is simple. Although the values of dielectric properties of plasticine ($4.8-j0.3$) are different from tangerine, the difference of dielectric properties between it and air ($1-j0$) is obvious. The dielectric constant of plasticine is 4.8 times higher than that of air. While the dielectric constant of normal and granulated tangerines are 45.23 and 33.96, respectively, the dielectric constant of normal tangerine is 1.33 times higher than that of granulated tangerine. With the obvious difference in dielectric constant of plasticine and air, we therefore used a plasticine model to simulate a normal tangerine and a missing section to simulate a granulated tangerine. Hence, the effect of position of granulation and the size of the tangerine including the number of beams of the antenna can be experimentally investigated. It is

expected that the Rician k-factor for the plasticine model with a missing section, that simulates a granulated tangerine, is lower than that for the model without a missing section (representing a normal tangerine).

In order to validate the proposed idea that the system can truly detect granulated tangerine, a plasticine model was sculpted to be 6 cm in size, the same as the typical size of tangerines in Fig. 4.6 (a). The spherical plasticine modeled with the missing section can be seen in Fig 4.6 (b).

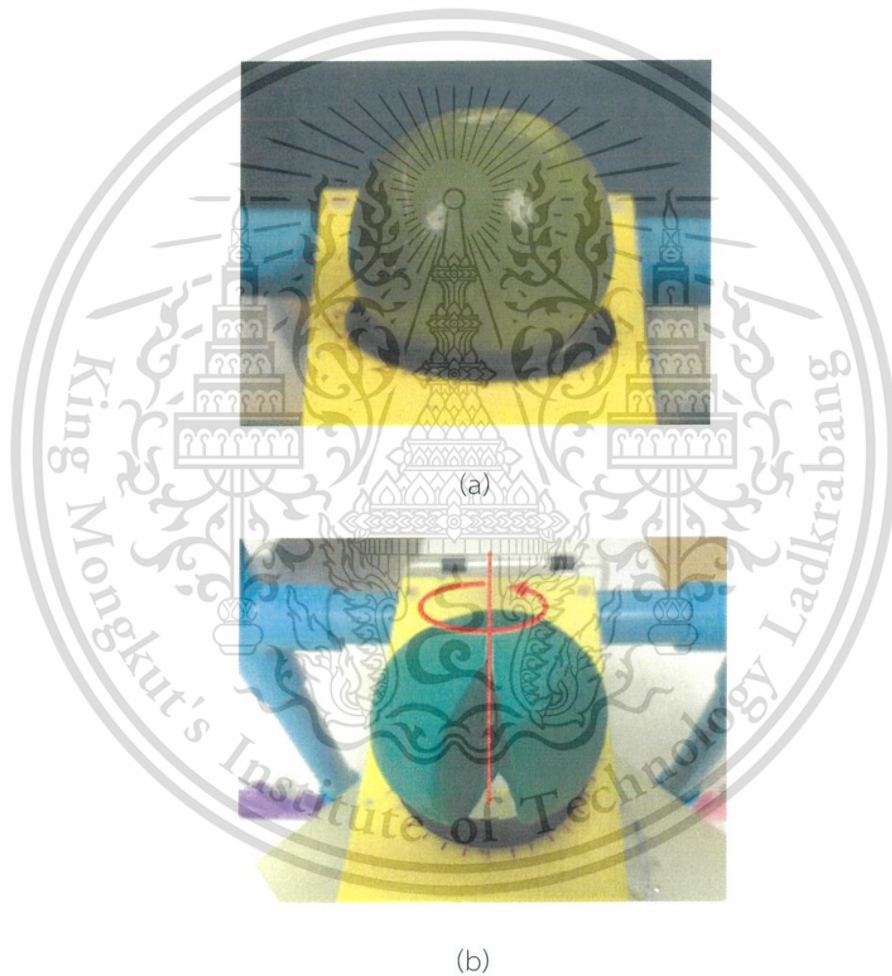


Fig. 4.6 Photographs of objects under test: (a) real tangerine and (b) plasticine with a missing section.

Since the system operates at 2.45 GHz ISM band, the problem of interference must be properly controlled. We measured interference with a
This material is reserved for educational use only, not allowed for commercial use.

Forbidden to modify the content, and cite the document when use.

spectrum analyzer at the sensor system and found the interference level was -50 dBm which was lower than a sensitivity of the system.



Fig. 4.7 Photograph of calibration with a metallic ball

Calibration was done with a metallic ball with the same size as the fruit to normalize the different amplitudes of the scattered waves coming in from all 8 directions, as shown in Fig. 4.7. After calibration, the metallic ball was replaced with the plasticine model. The plasticine model with no missing section showed uniform dielectric properties. Ideally, all scattered waves would be identical, hence variance of 0 and k-factor of infinity should be obtained. In practice, the variance was not exactly zero but a low value. Most importantly, the variance of the model with no missing section was less than the model with a missing section and hence the k-factor was higher than that from the model with a missing section.

Table 4.2 Propagation channel of 6-cm plasticine model with a missing section measured by the 8-beam antenna system

Section's position	Propagation channel		
	Mean (S)	Variance (σ^2)	k-factor
0°	0.562	0.033	4.810
45°	0.579	0.042	3.959
90°	0.604	0.054	3.395
135°	0.593	0.058	3.045

This material is reserved for educational use only, not allowed for commercial use.

Forbidden to modify the content, and cite the document when use.

Table 4.2(cont.) Propagation channel of 6-cm plasticine model with a missing section measured by the 8-beam antenna system

Section's position	Propagation channel		
	Mean (S)	Variance (σ^2)	k-factor
180°	0.613	0.050	3.759
225°	0.617	0.046	4.138
270°	0.576	0.051	3.248
315°	0.559	0.042	3.700
Average	0.588	0.047	3.757
Maximum	0.617	0.058	4.810
Minimum	0.559	0.033	3.045

Table 4.3 Propagation channel of 6-cm plasticine model with a missing section measured by the 4-beam antenna system

Section's position	Propagation channel		
	Mean (S)	Variance (σ^2)	k-factor
0°	0.630	0.023	8.725
45°	0.629	0.030	6.618
90°	0.643	0.036	5.729
135°	0.631	0.036	5.541
180°	0.655	0.036	5.956
225°	0.661	0.035	6.232
270°	0.622	0.041	4.732
315°	0.608	0.033	5.512
Average	0.635	0.034	6.131
Maximum	0.661	0.041	8.725
Minimum	0.608	0.023	4.732

Experiments were conducted on the plasticine model without a missing section (representing a normal tangerine) and with a missing section (representing a granulated tangerine). The mean and variance of the plasticine model with no missing section were found to be 0.653 and 0.034, respectively, and the

corresponding k-factor was 6.254. Table 4.2 depicts measured results when the position of the missing section was hand-turned in 45° increment at a time from 0° to 315°. At each position, the measured results from the eight-beam system were used to calculate mean, variance, and k-factor. Obviously, for all positions, the values of the means of the plasticine model with a missing section were less than that obtained from the model with no missing section and their variances were higher except for the 0° position where the beam width was the widest. This resulted in a lower k-factor, at 3.757, than the case of the model with no missing section. This same procedure was applied for determining the k-factors obtained from measurements with a system with four beams (Beam 1, 2, 3, 4 of the array antenna). It was found that the plasticine with no missing section showed a mean and variance of 0.677 and 0.029, respectively, and the corresponding k-factor was 7.848. The higher mean and lower variance (due to fewer data from only 4 beams) than those provided by the system with eight beams resulted in a higher k-factor. Table 4.3 shows the results of the plasticine model with a missing section measured by the 4-beam system. The values of the mean at all positions that the model with a missing section was placed were lower than that where there was no missing section, while the variances were higher except at the 0° position due to same reason as in the case of eight-beam, hence the k-factors for the model with a missing section were lower than that without a missing section except at the 0° position.

For the 8-beam antenna system, an appropriate k-factor threshold level could be set in the range of 4.810 and 6.254, whereas for the 4-beam system, the range would be between 8.725 and 7.848. This narrower range resulted in higher chance of erroneous detection.

Table 4.4 Propagation channel of 8-cm plasticine model with a missing section measured by the 8-beam antenna system

Section's position	Propagation channel		
	Mean (S)	Variance (σ^2)	k-factor
0°	0.839	0.016	21.998
45°	0.792	0.016	19.602
90°	0.698	0.019	12.821

Table 4.4(cont.) Propagation channel of 8-cm plasticine model with a missing section measured by the 8-beam antenna system

Section's position	Propagation channel		
	Mean (S)	Variance (σ^2)	k-factor
135°	0.694	0.017	14.166
180°	0.714	0.020	12.745
225°	0.741	0.017	16.149
270°	0.734	0.018	14.965
315°	0.798	0.020	15.920
Average	0.751	0.018	16.046
Maximum	0.839	0.020	21.998
Minimum	0.694	0.016	12.745

Table 4.5 Propagation channel of 8-cm plasticine model with a missing section measured by the 4-beam antenna system

Section's position	Propagation channel		
	Mean (S)	Variance (σ^2)	k-factor
0°	0.846	0.00395	90.597
45°	0.832	0.00285	121.44
90°	0.781	0.00360	84.717
135°	0.784	0.00354	86.816
180°	0.750	0.00362	77.693
225°	0.768	0.00291	101.344
270°	0.794	0.00393	80.208
315°	0.836	0.00298	117.264
Average	0.799	0.00342	95.010
Maximum	0.846	0.00395	121.44
Minimum	0.750	0.00285	77.693

A larger 8-cm plasticine model was measured by the same procedure with the 8-beam antenna system and the results for the model with and without a missing section followed the same trend but the values of the means were higher

and the values of the variances were lower, so the value of the k-factor for the model with no missing section was higher at 23.481 instead of 6.254. It should be noted that the dimension of the fruit had an influence on the k-factor, possibly due to the bigger tangerine model gave out more scattered waves. Table 4.4 shows the results of the 8-cm plasticine model with a missing section measured by the 8-beam system. It was found that the bigger model with a missing section still showed a lower value of k-factor than its counterpart without a missing section. The 8-cm model was also measured with the 4-beam antenna system, and the mean and variance obtained for the model without a missing section were 0.849 and 0.00325, respectively, hence the corresponding value of k-factor was 111.80 which was much higher than that achieved by its 8-beam counterpart. Table 4.5 illustrates the measured results from the 8-cm plasticine model with a missing section by using the four-beam system. It should be noted that at some positions, the values of the k-factors for the model with a missing section were quite close to those without a missing section. This is most likely due to the 4-beam system not being able to detect scattered waves coming in from the directions corresponding to those positions where the missing section was at. To sum up, a measurement with fewer beams resulted in a higher detection error due to a higher chance that the missing part would not get detected.

Because the value of the Rician k-factor for the plasticine model with a missing section was found to be consistently lower than that for the model without a missing section in almost every case, it was deduced that the 8-beam system of sensor was suitable for detecting real 6-cm granulated tangerines.

4.3.2. Results from real tangerine fruits

Sixty-five tangerine fruits the size of 6 ± 0.5 cm were purchased from a local market. Cross-section photographs of samples of normal and granulated tangerine are shown in Fig. 4.8 (a) and (b), respectively. These samples were measured with the proposed sensor then each tangerine was broken to see if there was any granulation. Also, °Brix (°Bx) values were measured with an OPTIK handheld refractometer [62]. After having been measured, all samples were divided into two groups—normal and

granulated fruits—according to the detection results, shown by symbol ‘O’ in Fig. 4.9. The brix values for the granulated tangerines were near zero while those for the normal tangerines were between 10.5 and 12, demonstrating that the normal tangerines were much sweeter.

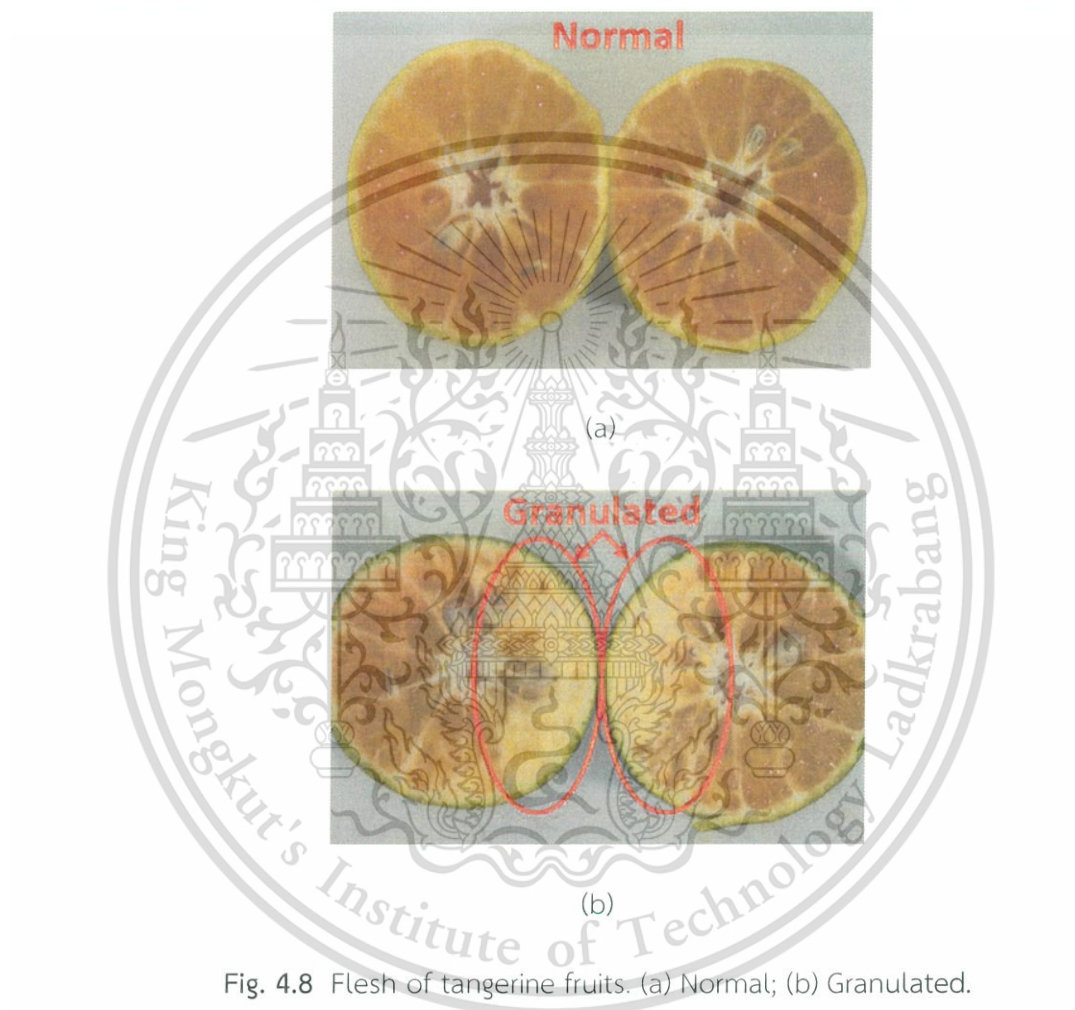
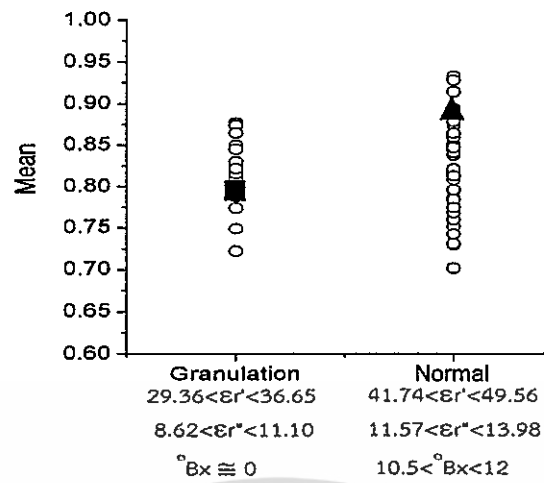
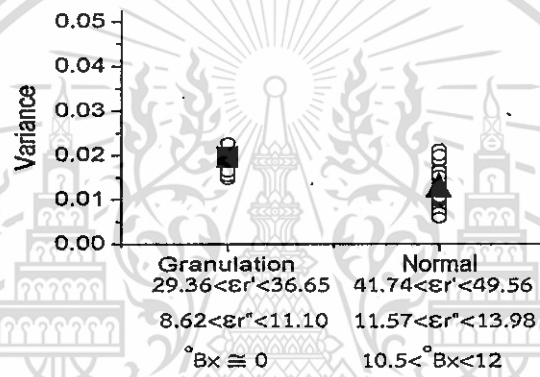


Fig. 4.8 Flesh of tangerine fruits. (a) Normal; (b) Granulated.

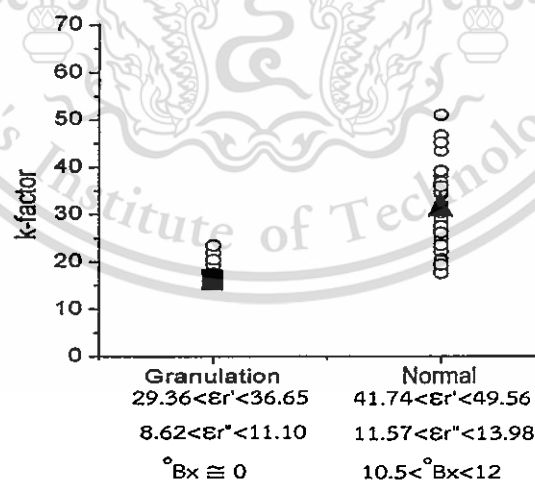
Shown in Fig. 4.9 (a) the mean values of 10 repeated measurements of the scattered waves from 8 directions around each fruit. From these, the received powers were calculated. It was found that the magnitudes of the scattered waves from the granulated tangerines varied between 0.72 and 0.87 while those from the normal tangerines were between 0.71 and 0.93.



(a)



(b)



(c)

Fig. 4.9 Measured results from normal and granulated tangerine fruits: (a) mean; (b) variance; and (c) k-factor

It is seen in Fig. 4.9 (b) that the values of variance of granulated and normal tangerines varied between 0.015 to 0.023 and 0.008 to 0.019, respectively. For illustration, the symbol '■' in Fig. 4.9 (a) and (b) represent the value of mean and variance of one granulated tangerine which provide the k-factor of 15.6 in Fig. 4.9 (c). In the same manner, the symbol '▲' show the values of mean, variance and k-factor of a normal tangerine. The values of k-factors for granulated tangerines and normal tangerines were in the ranges of 15.2 to 22.52 and 18.14 to 50.96, respectively. The range of values of k-factors for the normal tangerines was overlapped with the range for the granulated tangerines and the measurement variance was large most likely due to the fruits being of different sizes and having different degrees of granulation. Selection of k-factor threshold level was fine-tuned in increment of 0.1 between 18 and 23 (overlapping measured values for normal and granulated tangerines). The accuracy rate was calculated from the ratio of the number of correctly identified tangerines to the total number of tangerines. The highest accuracy of 85% was achieved at the threshold level of 18.5. A more accurate result should be possible if a more sophisticated decision making procedure such as fuzzy logic and artificial neural networks are used to select the threshold level. This undertaking is left for a further study. From our design point of view, this kind of performance is readily acceptable for a crude prototype, and the system has a great potential for discriminating normal and granulated fruits at an accuracy rate that will be satisfactory to vendors.

4.4 Conclusion

As a response to the high demand for a sensor for detecting granulation in tangerines, a non-destructive sensor has been designed and tested. It was based on a beam-scanning reflectometer that can receive waves scattered from tangerines in different directions. This sensor system was accomplished by using a phased array antenna whose elements were pattern reconfigurable Yagi-Uda antenna that had 4 beams and a conical reflector. The 2-element array had eight beams and was able to receive scattered waves from 8 directions. The different dielectric properties of normal and granulated tangerines resulted in different scattered waves and hence

different values of k-factor. This system was designed to operate at 2.45 GHz and tested with spherical plasticine models. The results showed that it was able to detect a missing section in the plasticine model. The system was then used to measure real tangerines, and at 18.5 k-factor threshold level setting, it was able to achieve an 85% classifying accuracy, showing the great potential of this design concept.



CHAPTER 5

CONCLUSIONS AND DISCUSSIONS

5.1 Conclusion

The first chapter mentioned on problem in an orange fruit which granulation is a common problem. Many techniques have been attempted for detecting this disorder. However, there is a limitation for real use. Therefore, the work presented in this dissertation aims to enhance sensor system for classifying granulated oranges.

In order to design the sensor system, the properties of oranges and basis of application should be investigated and acknowledged which have been presented in chapter 2. Orange's properties were measured which tangerine species were samples for test. It is seen that the dielectric constant and loss factor of normal tangerine are significantly higher than those of granulated tangerine. This causes different propagation channel when wave travels within normal and granulated tangerines. To indicate characteristic of the channel, Rician k-factor can be utilized for estimating channel characteristic of wireless communication system and this factor is applied for channel of tangerine fruit. The dielectric properties of tangerines were treated as a propagation channel that k-factor relates with dielectric properties. To calculate k-factor, the transmitting antenna illuminates electromagnetic wave to the fruit, and then the scattered wave measures with the receiving antenna. However, the k-factor is statistical data of received wave from all effects within tangerine. Therefore, a beam-scanning antenna is necessary to receive the scattered wave from the fruit.

For beam scanning, pattern reconfigurable antenna and phased array antenna have been proposed in chapter 3. They have been designed and developed to form the foundation for designing a phased array with pattern reconfigurable antenna elements. The pattern reconfigurable antenna is based on Yagi-Uda antenna. It can switch main beam toward four directions using PIN diodes to change the modes of parasitic element and driven element. In order to enhance wide scan of phased array antenna, the pattern reconfigurable antenna is utilized as elements of array. A two-

element linear array by using 1-bit phase shifter was designed for operating at 2.45 GHz. The simulation and measurement show that the array antenna with pattern reconfigurable antenna elements can scan its main beam toward 8 directions with a low gain-fluctuation at the operating frequency of 2.45 GHz. These results confirm that performances of the phased array using pattern reconfigurable Yagi-Uda antennas can be deployed for a novel beam-scanning reflectometer.

Then, a sensor system was designed and fabricated which has been presented in chapter 4. This system was designed to operate at 2.45 GHz. It is based on a beam-scanning reflectometer that can receive scattered waves from various positions around a tangerine, hence the value of k-factor is obtained. To test performance of the proposed beam-scanning reflectometer, spherical plasticine models were used. The results show that it is able to detect a missing section in the plasticine model. The system was then used to measure real tangerines. It is seen that k-factors of granulated tangerine are essentially lower than those of normal tangerine. At 18.5 k-factor threshold level setting, it is able to achieve an 85% classifying accuracy. The examined results of this prototype show well tendency of capability for classifying granulated oranges.

5.2 Discussion for future studies

According to the experiment of applying a beam-scanning reflectometer for classifying granulated oranges, the results show the great potential of this design concept and it is expected to use for real-time monitoring. However, accuracy of the sensor system should be improved which is possible if a more sophisticated decision making procedure such as fuzzy logic and artificial neural networks are used to select the threshold level. This undertaking is left for a further study. Moreover, large beam width of phased array antenna is another problem. Since it has a chance to receive scattered wave from other positions on an orange, this causes error for calculating k-factor. Thus, phased array antenna can be solved and developed in the future studies by increasing number of antenna element to reduce beam width.

REFERENCES

- [1] Office of agricultural economics, Thailand foreign agricultural trade statistics 2015. [Online]. Available: <http://www.oae.go.th/download/journal/2559/thailandtradestat2558.pdf>
- [2] Office of agricultural economics, Economic information of agriculture 2015. [Online]. Available: http://www.oae.go.th/download/download_journal/2559/commodity58.pdf
- [3] B. M. El-Zeftawi, "Factors Affecting Granulation and Quality of Late-Picked Valencia Oranges," *Journal of Horticultural Science*, vol. 53, no. 4, pp. 331-337, 1978
- [4] J. K. Burns and L. G. Albrigo, "Granulation in grapefruit," *Proc. Fla. State Hort. Soc.*, vol. 110, pp. 204-208, 1997.
- [5] J. W. Stevens, and W. E. Baier, "Refractometer determination of soluble solids in citrus juices," *Industrial and engineering chemistry*, vol. 11, no. 8, pp. 447-449, Aug. 1939.
- [6] J. Bai, E. A. Baldwin, G. McCollum, A. Plotto, J. A. Manthey, W. W. Widmer, G. Luzio, and R. Cameron, "Changes in Volatile and Non-Volatile Flavor Chemicals of "Valencia" Orange Juice over the Harvest Seasons," *Food*, vol. 5, no. 1, pp. 1-17, Jan. 2016.
- [7] S. V. Tang, and J. G. Blair, "The relation of specific gravity of whole fruit to the internal quality of oranges," *Proc. Florida State Hort. Soc.*, pp. 251-260, 1965.
- [8] A. H. Gomez, J. Wang, G. Hu, and A. G. Pereira, "Electronic nose technique potential monitoring mandarin maturity," *Sensor and Actuators B*, vol. 113, no. 1, pp. 347-353, Jan. 2006.
- [9] J. Wang, A. H. Gomez, and A. G. Pereira, "Acoustic impulse response for measuring the firmness of Mandarin during storage," *Journal of Food Quality*, vol. 29, no.4, pp.392-404, Aug. 2006.
- [10] A. Vidal, P. Talens J. M. Prats-Montalban, S. Cubero, F. Albert, and J. Blasco, "In-Line Estimation of the Standard Colour Index of Citrus Fruits Using a Computer Vision System Developed For a Mobile Platform," *Food Bioprocess Technol.*, vol. 6, no. 12, pp. 3412-3419, Dec. 2013.

- [11] T. G. Knight, A. Klieber, and M. Sedgley, "The Relationship Between Oil Gland and Fruit Development in Washington Navel Orange (*Citrus sinensis* L. Osbeck)," *Annals of Botany*, vol. 88, no. 6, pp. 1039-1047, Dec. 2001.
- [12] T. Pankasemsul, and B. Sutisanchanchai, "Quality evaluation of some fruits by using X-ray transmittance," *Proceedings of 37th Kasetsart University Annual Conference: Plant, Agricultural Extension and Communication*, Bangkok, Thailand, pp. 56-61, Feb. 1999.
- [13] J. Zhang, Y. Lui, N. Wang, and R. Ruan, "NMR technique application in evaluating the quality of navel orange during Storage," *Procedia Engineering*, vol. 37, pp. 234-239, 2012.
- [14] N. Zur, L. Shlizerman, G. Ben-Ari, and A. Sadka, "Use of magnetic resonance imaging (MRI) to study and predict fruit splitting in citrus," *The Horticulture Journal*, pp. 1-8, Jul. 2016.
- [15] S. Xudong, Z. Hailiang, and L. Yande, "Nondestructive assessment of quality of Nanfeng mandarin fruit by a portable near infrared spectroscopy," *Int. J. Agric. & Biol. Eng.*, vol. 2, no. 1, pp. 65-71, Mar. 2009.
- [16] C. Luo, L. Xue, M. Liu, J. Li, and X. Wang, "Nondestructive Measurement of Sugar Content in Navel Orange Based on Vis-NIR Spectroscopy," *International Conference on Computer and Computing Technologies in Agriculture*, pp. 467-473, Oct. 2010.
- [17] F. Antonucci, F. Pallottino, G. Paglia, A. Palma, S. D. Aquino, and P. Menesatti, "Non-destructive estimation of mandarin maturity status through portable VIS-NIR spectrophotometer," *Food and Bioprocess Technol.*, vol. 4, no. 5, pp. 809-813, July 2011.
- [18] P. Leekul, S. Chivapreecha, and M. Krairiksh, "Microwave sensor for tangerine classification based on coupled-patch antennas," *Int.l J. of Electron.*, vol. 103, no. 8, pp. 1287-1300, Oct. 2015.
- [19] P. Leekul, S. Chivapreecha, and M. Krairiksh, "Microwave sensor for defected fruit classification," *Proc. of 2015 IEEE Conference on Antenna measurement and applications*, Chiangmai, 2015.
- [20] P. Leekul, S. Chivapreecha, C. Phongcharoenpanich, and M. Krairiksh, "Rician k-factors-based sensor for fruit classification by maturity stage," *IEEE Sensors J.*, vol. 16, no. 17, pp. 6559-6565, Sep. 2016.

- [21] G. F. Engen and R. W. Beatty, "Microwave reflectometer techniques," *IRE Transactions on Microwave Theory and Techniques*, vol. 7, no. 3, pp.351-355, July 1959.
- [22] M. Oda, A. Mase, and K. Uchino, "Non-destructive measurement of sugar content in apples using millimeter wave reflectometry and artificial neural networks for calibration," *Proc. of Asia Pacific Microwave Conference*, Melbourne, pp.1386-1389, 2011.
- [23] P. Yoiyod, and M. Krairiksh, "Microwave vector reflectometer using self-mixing oscillator antennas," *Latin America Applied Research*, vol. 45, no. 3, pp. 199-205, April 2015.
- [24] P. Ngamjanyaporn, C. Phongcharoenpanich, P. Akkaraekthalin, and M. Krairiksh, "Signal-to-interference ratio improvement by using a phased array antenna of switched-beam elements," *IEEE Trans. Antennas Propag.*, vol.53, no.5, pp.1819-1828, May 2005.
- [25] C. Kittiyanyapunya, and M. Krairiksh, "A Four-Beam Pattern Reconfigurable Yagi-Uda Antenna," *IEEE Trans. Antennas Propag.*, vol. 61, no. 12, pp. 6210-6214, Dec. 2013.
- [26] Orange book, 2nd Edition 2004, Tetra Pak Processing System AB, Pyramid Communication AB.
- [27] V. Hippel, "Dielectric Materials and Applications," The Technology Press of MIT and John Wiley and Sons, New York, 1954.
- [28] J. Tang, F. Hao, and M. Lau, *Advances in bioprocessing engineering*, vol. 1, Singapore: World Scientific, 2002
- [29] Keysight technology, 85070E Dielectric probe kit 200 MHz to 50 GHz, Technical overview. [Online]. Available: <http://literature.cdn.keysight.com/litweb/pdf/5989-0222EN.pdf?id=364444>
- [30] Keysight technology, FieldFox Handheld Analyzers, Datasheet. [Online]. Available: <http://literature.cdn.keysight.com/litweb/pdf/5990-9783EN.pdf?id=2210837>
- [31] Handheld Refractometer, OPTIK, Model B-32.
- [32] S. R. Saunders and A. Aragon-Zavala, *Antennas and Propagation for Wireless Communication Systems*, 2nd Ed Wiley, 2007.
- [33] D. M. Pozar, "Microwave Engineering," 4th ed., New York: Wiley, 2011.

- [34] Report ITU-R SM.2153-4, Technical and operating parameters and spectrum use for short-range radiocommunication devices, SM series Spectrum management, 2013.
- [35] C. G. Christodoulou, Y. Tawk, S. A. Lane, and S. R. Erwin, "Reconfigurable antennas for wireless and space applications," *Proc. IEEE*, vol. 100, no. 7, pp. 2250-2261, Jul. 2012.
- [36] W. Hu, M. Y. Ismail, R. Cahill, J. A. Encinar, V. Fusco, H. S. Gamble, D. Linton, R. Dickie, N. Grant, and S. P. Rea, "Liquid-crystal-based reflectarray antenna with electronically switchable monopulse patterns," *Electron. Lett.*, vol. 43, no. 14, Jul. 2007.
- [37] D. Rodrigo, L. Jofre, and B. A. Cetiner, "Circular beam-steering reconfigurable antenna with liquid metal parasitics," *IEEE Trans. Antennas Propag.*, vol. 60, no. 4, pp. 1796-1802, Apr. 2012.
- [38] C. J. Panagamuwa, A. Chauraya, and J. C. Vardaxoglou, "Frequency and beam reconfigurable antenna using photoconducting switches," *IEEE Trans. Antennas Propag.*, vol. 54, no. 2, pp. 449-454, Feb. 2006.
- [39] G. H. Huff, and J. T. Bernhard, "Integration of packaged RF MEMS switches with radiation pattern reconfigurable square spiral microstrip antennas," *IEEE Trans. Antennas Propag.*, vol. 54, no. 2, pp. 464-469, Feb. 2006.
- [40] X. Ding, and B. Z. Wang, "A novel wideband antenna with reconfigurable broadside and endfire patterns," *IEEE Antennas Wireless Propag. Lett.*, vol. 12, pp. 995-998, 2013.
- [41] S. H. Chen, J. S. Row, and K. L. Wong, "Reconfigurable squarering patch antenna with pattern diversity," *IEEE Trans. Antennas Propag.*, vol. 55, no. 2, pp. 472-475, Feb. 2007.
- [42] S. J. Wu, and T. G. Ma, "A wideband slotted bow-tie antenna with reconfigurable CPW-to-slotline transition for pattern diversity," *IEEE Trans. Antennas Propag.*, vol. 56, no. 2, pp. 327-334, Feb. 2008.
- [43] I. Lim, and S. Lim, "Monopole-like and boresight pattern reconfigurable antenna," *IEEE Trans. Antennas Propag.*, vol. 61, no. 12, pp. 5854-5859, Dec. 2013.
- [44] S. Yong, and J. T. Bernhard, "A pattern reconfigurable null scanning antenna," *IEEE Trans. Antennas Propag.*, vol. 60, no. 10, pp. 4538-4544, Oct. 2012.

- [45] S. Yong, and J. T. Bernhard, "Reconfigurable null scanning antenna with three dimensional null steer," *IEEE Trans. Antennas Propag.*, vol. 61, no. 3, pp. 1063-1070, Mar. 2013.
- [46] M. I. Lai, T. Y. Wu, J. C. Hsieh, C. H. Wang, and S. K. Jeng, "Compact switched-beam antenna employing a four-element slot antenna array for digital home applications," *IEEE Trans. Antennas Propag.*, vol. 56, no. 9, pp. 2929-2936, Sep. 2008.
- [47] V. A. Nguyen, M. H. Jeong, M. T. Dao, and S. O. Park, "Four-port beam reconfigurable antenna array for pattern diversity system," *IET Microw. Antennas Propag.*, vol. 6, pp. 1179-1186, 2012.
- [48] Y. Y. Bai, S. Xiao, C. Liu, X. Shuai, and B. Z. Wang, "Design of pattern reconfigurable antennas based on a two-element dipole array model," *IEEE Trans. Antennas Propag.*, vol. 61, no. 9, pp. 4867- 4871, Sep. 2013.
- [49] S. Zhang, G. H. Huff, J. Feng, and J. T. Bernhard, "A pattern reconfigurable microstrip parasitic array," *IEEE Trans. Antennas Propag.*, vol. 52, no. 10, pp. 2773-2776, Oct. 2004.
- [50] X. S. Yang, B. Z. Wang, S. H. Yeung, Q. Xue, and K. F. Man, "Circularly polarized reconfigurable crossed-Yagi patch antenna," *IEEE Antennas Propag. Mag.*, vol. 53, no. 5, pp. 65-80, Oct. 2011.
- [51] C. Kittiyannunya, and M. Krairiksh, "A Four-Beam Pattern Reconfigurable Yagi-Uda Antenna," *IEEE Trans. Antennas Propag.*, vol. 61, no. 12, pp. 6210-6214, Dec. 2013.
- [52] C. A. Balanis, *Antenna Theory: Analysis and Design*, 3rd edition., Wiley, 2005.
- [53] M. Krairiksh, "Yagi-Uda antenna," Lecture notes distributed in antenna engineering at King Mongkut's Institute of Technology Ladkrabang, Bangkok, Feb. 2012.
- [54] Y. G. Kim, D. S. Woo, K. W. Kim, and Y. K. Cho, "A new ultrawideband microstrip-to-cps transition," *IEEE MTT-S Int. Dig.*, 2007, pp. 1563-1566.
- [55] R. J. Mailloux, *Phased Array Antenna Handbook*, 2nd ed. Norwood, MA., Artech house, INC., 2005.
- [56] K. S. Beenamole, U. K. Revankar, and V. M. Pandharipande, "Wide Band Wind Beam Antenna Elements for Active Phased Array Applications," *IETE Journal of Research*, vol. 54, no. 2, pp. 155-167, April 2008.

- [57] M. Scott, "A printed dipole for wide scanning array application," International Conference on Antenna and Propagation, pp. 37-40, April 17-20, 2001.
- [58] K. S. Beenamole, Prem N. S. Kutiya, U. K. Revankar, and V. M. Pandharipande, "Resonant microstrip meander line antenna element for wide scan angle active phased array antennas," *Microw. Opt. Technol. Lett.*, vol. 50, no. 7, pp. 1737-1740, July 2008.
- [59] P. Ngamjanyaporn, C. Phongcharoenpanich, P. Akkaraekthalin, and M. Krairiksh, "Signal-to-interference ratio improvement by using a phased array antenna of switched-beam elements," *IEEE Trans. Antennas Propag.*, vol.53, no.5, pp.1819-1828, May 2005.
- [60] Y. Y. Bai, S. Q. Xiao, M. C. Tang, Z. F. Ding, and B.-Z. Wang, "Wide-angle scanning phased array with pattern reconfigurable elements," *IEEE Trans. Antennas Propag.*, vol. 59, no. 11, pp. 4071-4076, Nov. 2011.
- [61] X. Ding, B.-Z. Wang, and G.-Q. He, "Research on a millimeter-wave phased array with wide-angle scanning performance," *IEEE Trans. Antennas Propag.*, vol. 61, no. 10, pp. 5319-5324, Oct. 2013.
- [62] Handheld refractometer, OPTIK, Model B-32, OPTIK, Japan, 2009.

RELATED PUBLICATIONS

Journals

- 1) C. Kittiyanyunya, P. Leekul, C. Phongcharoenpanich and M. Krairiksh, "Beam-Scanning Reflectometer for Detecting Granulated Fruits," *IEEE Sensors J.*, vol. 17, no. 5, pp. 1277-1284, Mar. 2017.
- 2) C. Kittiyanyunya and M. Krairiksh, "Design of pattern reconfigurable printed Yagi-Uda antenna," *IEICE Trans. Commun.*, vol. E99-B, no. 1, pp. 19-26, Jan. 2016.

Conferences

- 1) C. Kittiyanyunya and M. Krairiksh, "Phased array of switched beam elements and application," *2016 International Symposium on Antennas and Propagation Conference Proceedings, (ISAP 2016)*, pp. 954-955, Okinawa, Japan, Oct. 2016.
- 2) C. Kittiyanyunya and M. Krairiksh, "A reflectometer with beam switching capability," *2015 IEEE 4th Asia-Pacific Conference on Antennas and Propagation, (APCAP)*, pp. 384-385, Bali Island, Indonesia, Jul. 2015.
- 3) C. Kittiyanyunya and M. Krairiksh, "Pattern reconfigurable printed Yagi-Uda antenna," *2014 International Symposium on Antennas and Propagation Conference Proceedings, (ISAP 2014)*, pp. 325-326, Kaohsiung, Taiwan, Dec. 2014.
- 4) C. Kittiyanyunya and M. Krairiksh, "A Beam Switching Printed Yagi-Uda Antenna," *Proceedings of the 2014 Thailand-Japan Microwave*, Bangkok, Thailand, Nov. 2014.

AUTHOR BIOGRAPHY

Chainarong Kittiyapunya was born on December 15, 1985 in Nakhon Pathom, Thailand. He received the B.Eng. degree in electrical communication and electronic engineering from the King Mongkut's University of Technology Thonburi, Bangkok, Thailand, in 2008, and the M.Eng. degree in telecommunication engineering from the King Mongkut's Institute of Technology Ladkrabang, Bangkok, in 2012, where he was a Ph.D. student between 2013 and 2017. His research interests are in antenna design for mobile communications and microwave in sensor applications.

